SANDIA REPORT

SAND2003-4550
Unlimited Release
Printed December 2003

SREF—A SIMPLE REMOVABLE EPOXY FOAM DECOMPOSITION CHEMISTRY MODEL

Michael L. Hobbs

Prepared by
Sandia National Laboratories
Albuquerque, New Mexico 87185 and Livermore, California 94550

Sandia is a multiprogram laboratory operated by Sandia Corporation,
a Lockheed Martin Company, for the United States Department of Energy's
National Nuclear Security Administration under Contract DE-AC04-94AL85000.

Sandia National Laboratories

Issued by Sandia National Laboratories, operated for the United States Department of Energy by Sandia Corporation.

Available to DOE and DOE contractors from
U.S. Department of Energy
Office of Scientific and Technical Information
P.O. Box 62
Oak Ridge, TN 37831

Telephone: (865)576-8401
Facsimile: (865)576-5728
E-Mail: reports@adonis.osti.gov
Online ordering: http://www.doe.gov/bridge

Available to the public from
U.S. Department of Commerce
National Technical Information Service
5285 Port Royal Rd
Springfield, VA 22161

Telephone: (800)553-6847
Facsimile: (703)605-6900
E-Mail: orders@ntis.fedworld.gov
Online order: http://www.ntis.gov/help/ordermethods.asp?loc=7-4-0#online

SAND2003-4550
Unlimited Release
Printed December 2003

SREF – A SIMPLE REMOVABLE EPOXY FOAM DECOMPOSITION CHEMISTRY MODEL

Michael L. Hobbs
Engineering Sciences Center
Sandia National Laboratories
P.O. Box 5800
Albuquerque, New Mexico 87185-0836

Abstract

A Simple Removable Epoxy Foam (SREF) decomposition chemistry model has been developed to predict the decomposition behavior of an epoxy foam encapsulant exposed to high temperatures. The foam is composed of an epoxy polymer, blowing agent, and surfactant. The model is based on a simple four-step mass loss model using distributed Arrhenius reaction rates. A single reaction was used to describe desorption of the blowing agent and surfactant (BAS). Three of the reactions were used to describe degradation of the polymer. The coordination number of the polymeric lattice was determined from the chemical structure of the polymer; and a lattice statistics model was used to describe the evolution of polymer fragments. The model lattice was composed of sites connected by octamethylcylotetrasiloxane (OS) bridges, mixed product (MP) bridges, and bisphenol-A (BPA) bridges. The mixed products were treated as a single species, but are likely composed of phenols, cresols, and furan-type products. Eleven species are considered in the SREF model – 1) BAS, 2) OS, 3) MP, 4) BPA, 5) 2-mers, 6) 3-mers, 7) 4-mers, 8) nonvolatile carbon residue, 9) nonvolatile OS residue, 10) L-mers, and 11) XL-mers. The first seven of these species (VLE species) can either be in the condensed-phase or gas-phase as determined by a vapor-liquid equilibrium model based on the Rachford-Rice equation. The last four species always remain in the condensed-phase. The 2-mers, 3-mers, and 4-mers are polymer fragments that contain two, three, or four sites, respectively. The residue can contain C, H, N, O, and/or Si. The L-mer fraction consists of polymer fragments that contain at least five sites (5-mer) up to a user defined maximum mer size. The XL-mer fraction consists of polymer fragments greater than the user specified maximum mer size and can contain the infinite lattice if the bridge population is less than the critical bridge population. Model predictions are compared to 133-thermogravimetric analysis (TGA) experiments performed at 24 different conditions. The average RMS error between the model and the 133 experiments was 4.25%. The model was also used to predict the response of two other removable epoxy foams with different compositions as well as the pressure rise in a constant volume hot cell.

Acknowledgements

I would like to thank Art Ratzel, Gene Hertel, Mike Prairie, and Martin Pilch for management support and funding. Ken Erickson provided data obtained from the low-pressure unconfined/partially-confined TGA apparatus as well as enthalpy data from a differential scanning calorimeter. Ted Borek provided adsorption tube analysis. Tom Fletcher and Dan Clayton (Brigham Young University) provided elemental analysis, chemical structure, and low/high pressure unconfined TGA data. Anita Renlund provided dynamic pressurization data from her hot cell experiment. Walt Gill and Terry Aselage provided the heat capacity data. Amy Sun helped articulate the VLE model. Shawna Liff (coop student from Northeastern University, Boston) helped calculate the RMS errors and to plot the results. Scot Waye (student intern from the University of Utah) also helped plot some of the results. I am also thankful for comments from internal reviewers at Sandia National Laboratories, Ed Russick and Amy Sun.

Table of Contents

List of Figures

List of Figures

List of Tables

List of Tables

Executive Summary

A decomposition chemistry model has been developed to predict the decomposition behavior of a closed-cell, rigid, thermally removable, epoxy foam (REF) that is used to encapsulate shock and vibration sensitive components. The removable foam contains cross-links created using Diels-Alder reversible chemistry. Some of the cross-links are broken when the Diels-Alder reaction is reversed at a temperature of 90ºC or higher; and a mild solvent is required to dissolve the material from the potted assembly. Without a solvent, the REF encapsulant merely softens at 90ºC. In this report, the behavior of the REF encapsulants exposed to significantly higher temperatures is addressed.

The mechanism describes decomposition of the epoxy polymer as well as desorption of the blowing agent and surfactant that were used to make the foam encapsulant. The Arrhenius reaction rates were assumed to be normally distributed based on the extent of reaction. The chemical structure, in conjunction with the elemental composition of the polymer, was used to describe the initial polymer lattice. The dynamic distributions of polymer fragments were determined using simple lattice statistics based on percolation theory. The relative amounts of condensed-phase and gas-phase decomposition products were determined using a vapor-liquid-equilibrium (VLE) model with pressure dependent activity coefficients. A mass transport model was used to describe the transport of polymer fragments and adsorbed species from the reaction site *or adsorption site* to the bulk gas.

The decomposition model considers eleven species—seven potentially volatile species and four nonvolatile species. The seven potentially volatile species, referred to in this report as vapor-liquid-equilibrium (VLE) species, can reside in the condensed-phase, the gas-phase, or both phases. The remaining four species are nonvolatile species and can only reside in the condensed-phase. The seven VLE species include BAS, OS, MP, BPA, 2-mer, 3-mer, and 4-mers, which represent the blowing agent and surfactant; octamethylcyclotetrasiloxane; mixed products; bisphenol A; and polymer fragments containing two, three, and four sites; respectively. The blowing agent and surfactant are lumped into a single species referred to as BAS. The mixed product species represent products such as cresols, phenols, and furans.

Four nonvolatile species are considered in the decomposition model—a carbon residue, a silicone residue with the same composition as OS, a large nonvolatile polymer fragment residue, and an extra-large polymer fragment residue. The OS residue has the same elemental composition as OS {e.g. $[(CH3)_2SiO]_4$} but has a much higher molecular weight e.g. $\{[(CH3)_2SiO]_4\}_{30}$. The carbon residue is independent of the degree of confinement or pressure. However, the OS residue depends on the degree that the decomposition products are retained or confined. The large nonvolatile polymer fragment residue considers 5-mer to max-mer polymer fragment populations, where the user determines the size of the max-mer. The extra-large polymer fragment residue considers the (max+1)-mer to the ∞-mer fragment.

The foam decomposition model is based on the assumption that the struts and windows of the foam are composed of an epoxy polymer. The bubbles in the foam are created using a perfluorohexane blowing agent and a surfactant. Over time, the blowing agent and surfactant adsorb on to the polymer. The epoxy polymer [1-3] was made using commercial ingredients (e.g. EPON 8121, Ancamine 2049, and Epi-Cure 3270) as well as a resin (RER1) produced at Sandia National Laboratories. The chemical structure of the epoxy polymer was inferred from the starting materials and the synthesis method used to make the macromolecule as discussed by Clayton [4].

SREF model predictions were compared to various ThermoGravimetric Analysis (TGA) experiments [4,5]. Most of the TGA experiments (133) were performed with REF100 that has a glass transition temperature of 69-89ºC [3]. Several additional TGA experiments were performed with two other REF formulations with higher glass transition temperatures—REF200 and REF300. All of the REF formulations were simulated with one set of chemical kinetics with the primary difference in the three formulations being the amount of the adsorbed blowing agent, surfactant, and curing agent.

The 133 TGA experiments [4,5] were organized into three categories: 1) unconfined experiments at ambient pressure, 2) unconfined experiments at elevated pressures, and 3) partially-confined experiments at ambient pressure. The unconfined experiments were performed in an open pan without restricting the decomposition products. The partially-confined experiments had hermetically sealed lids with orifices ranging in diameter from 2-mm to 60-µm. All of the TGA experiments were run using a purge gas of either N_2 or He. The average root mean squared (RMS) error for all 133 REF100 TGA experiments was 4%. The RMS error for the REF200 and REF300 TGA experiments was 1% and 3%, respectively.

To further validate the SREF model, a fully-confined, dynamic pressure "hot-cell" experiment was simulated. The hot-cell experiment used a pneumatic load cell to maintain a constant volume decomposition chamber by confining the ends of a cylindrical foam sample between two pistons. The lateral surface was confined using a solid cylinder of stainless steel. A gas-tight seal was maintained using O-rings on the pistons. Decomposition gases caused the pressure within the constant volume chamber to increase. The SREF model predicted the increase in pressure accurately, but predicted higher pressures during the unloading phase of the experiment as the gases were allowed to cool. Poor thermal contact and/or reversible reactions during the unloading phase of the experiment may explain the differences.

Nomenclature

Abbreviations

BAS	Blowing agent and surfactant
BPA	Bisphenol A
BYU	Brigham Young University
CPUF	Chemical-structure-based polyurethane foam
DGEBA	Diglycidyl ether of bisphenol A
DMDC	Dimethyldicyane
GC/MS	Gas chromatography/mass spectrometer
HPTGA	High-pressure thermogravimetric analysis
LPTGA	Low-pressure thermogravimetric analysis
LVDT	Linear variable displacement transducer
MP	Mixed products
NP	Nonyl phenol
OS	Octamethylcyclotetrasiloxane
PETA	Pentaerythritol triacrylate
PUF	Polyurethane foam response model
REF	Removable epoxy foam
REF100	series 100 removable epoxy foam
REF200	series 200 removable epoxy foam
REF300	series 300 removable epoxy foam
RER1	Removable epoxy resin 1 [3]
RMS	Root mean squared
SREF	Simple removable epoxy foam
SNL	Sandia National Laboratories
SPUF	Simple polyurethane foam
TGA	Thermogravimetric analysis
VLE	Vapor-liquid equilibrium

Miscellaneous Variables

A, B, C, D, E	Vapor pressure coefficients in eqn (90)
A_j	Pre exponential factor for the j^{th} reaction, 1/s
a_n	Distinct number of configurations for the n-mer
b_i	Parameter used in optimization method to obtain prefactors
C_p	Heat capacity, cal/g-K
E_j	Activation energy for the j^{th} reaction, cal/mol
BAS	Blowing agent and surfactant population

Nomenclature

BPA	Bisphenol A population
$C\text{-}residue$	Carbon residue
$\left(d^* / \phi\right)_j^i$	Diffusion parameter for the i^{th} level of confinement and the j^{th} reaction
$D_{i,STP}^m$	Self diffusion coefficient of the i^{th} species at standard temperature and pressure
D_j^e	Effective diffusivity for the j^{th} reaction
D_{AB}^m	Molecular diffusivity for binary mixtures of species A and B
D_L^m	Molecular diffusivity of polymer fragments
D_S^m	Molecular diffusivity of "sorbed" species
$D_{S,STP}^m$	Molecular diffusivity of "sorbed" species at standard temperature and pressure
d^*	Effective diffusion length, cm
$d_{orifice}$	Orifice diameter, µm
ε	Lennard-Jones potential well depth
Φ	Cumulative distribution function of a standardized normal random variable
Φ	Extent of reaction
ϕ	Ratio of effective diffusivity to molecular diffusivity
F	Moles of VLE combined-phase species (feed)
f	Function in eqn (68)
F_n	Probability that any given site is a member of a finite fragment of n sites with s bridges
f_{OS}	Mass fraction of octamethylcyclotetrasiloxane bridges, L_1^o, that ultimately end up in the $OS\text{-}residue$
Γ	The gamma function
γ_i	Activity coefficient of the i^{th} species
γ_i^o	Activity coefficient at ambient pressure
G_f	Gas fraction
$G_{f,transition}$	Transition gas fraction described by eqn (37)
γ_i	Scaled sensitivity coefficient
γ_i^2	Importance factor (scaled sensitivity coefficient squared)
η	Foam viscosity, centipoises
h_{rxn}	Overall reaction enthalpy, cal/g
κ	Boltzman's constant
K_i	Vapor-liquid equilibrium ratio
k_j	Effective reaction rate coefficient for the j^{th} reaction
k_j^c	Kinetic rate constant for the j^{th} reaction
k_j^m	Mass transport rate constant for the j^{th} reaction
L_1	Bridge population composed of octamethylcyclotetrasiloxane
L_1^o	Initial bridge population composed of octamethylcyclotetrasiloxane
L_2	Bridge population composed of mixed products
L_2^o	Initial bridge population composed of mixed products

Nomenclature

L_3	Bridge population composed of bisphenol A
L_3^o	Initial bridge population composed of bisphenol A
μ	Vector representing the mean of the SREF model parameters
M_A	Molecular weight of species A, g/mol
$\bar{M}_b$	Average bridge molecular weight, g/mol
M_B	Molecular weight of species B, g/mol
M_{BPA}	Molecular weight of bisphenol A (228 g/mol)
$M_{VLE}^{condensed}$	Average molecular weight of the condensed-phase VLE species
M_{VLE}^{gas}	Average molecular weight of the gas-phase VLE species
M_{DGEBA}	Molecular weight of diglycidyl ether of bisphenol A (340 g/mol)
M_i	Molecular weight of species i, g/mol
M_L	Molecular weight of bridge L, g/mol
M_{L_1}	Molecular weight of bridge L_1, g/mol
M_{L_2}	Molecular weight of bridge L_2, g/mol
M_{L_3}	Molecular weight of bridge L_3, g/mol
$M_{L\text{-mer}}$	Molecular weight of the L-mer fragments
M_n	Molecular weight of the n^{th} polymer fragment or n-mer
M_{OS}	Molecular weight of octamethylcyclotetrasiloxane (296 g/mol)
M_{RER1}	Molecular weight of RER1 (964 g/mol)
MP	Mixed product population
m	Sample mass, g
m^o	Initial sample mass, g
m_i^c	Mass fraction of the condensed-phase i^{th} species
m_i^g	Mass fraction of the gas-phase i^{th} species
m_t	Mass of an extended site
m_p	Mass of polymer in element or computational cell, g
n	Number of sites in a polymer fragment
n	Number of gas moles in an element or computational cell, mole
n	Number of points used to calculate RMS errors
n^o	Initial number of gas moles in an element or computational cell, mole
OS	Octamethylcyclotetrasiloxane population
$OS\text{-}residue$	Octamethylcyclotetrasiloxane residue
P	System pressure, atm
P^o	Initial system pressure, atm
$P^{\text{Hot Cell}}$	Pressure in the decomposition chamber of the hot cell, atm
P^{SREF}	Pressure calculated with the SREF decomposition model, atm
$P_{c,i}$	Critical pressure of the i^{th} species, atm
P_i^*	Vapor pressure of the i^{th} species, atm

p	Bridge population described by eqn (44)
p_c	Critical bridge population (infinite lattice no longer exists when bridge population drops below the critical bridge population, $1/\sigma$)
Q_n	Number density of the n-site fragments on a per site basis
q_{DSC}	Heat flow from differential scanning calorimeter, cal/s
q_i	Reaction enthalpy for i^{th} reaction, cal/g
q_{rxn}	Heat flow required to sustain chemical reactions, cal/s
q_{sen}	Heat flow required to maintain sample temperature at the specified ramp rate, cal/s
ρ_f^o	Initial bulk density of the foam, g/cm^3
ρ_H	High-density foam, g/cm^3
ρ_L	Low-density foam, g/cm^3
ρ_p^o	Initial density of the polymer, g/cm^3
R	Ideal gas constant
R_j^c	Chemical resistance for reaction j
R_j^m	Mass transport resistance for reaction j
r_i	Rate of reaction i
r_1	Rate of reaction 1
r_2	Rate of reaction 2
r_3	Rate of reaction 3
r_4	Rate of reaction 4
r_1^c	Intrinsic rate of reaction 1
r_1^d	Rate of diffusion for reaction 1
residue	Mass fraction of initial foam that ultimately forms a residue
σ	Inverse of critical bridge population
$\sigma+1$	Lattice coordination number
σ_{AB}	Collision diameter for species A and B
σ_i	Collision diameter of the i^{th} species
σ_i	Standard deviation of the i^{th} SREF model parameter
σ_j	Distributed activation energy model coefficient for the j^{th} reaction
σ_{S_f}	Standard deviation of the solid fraction
s	Number of bridges in a polymer fragment
S	“Sorbed” species population
S^o	Initial “sorbed” species population
S^*	Population of “sorbed” species absorbed on to the REF polymer at the reaction site
S_f	Solid fraction
S_f^{SREF}	Calculated solid fraction
S_f^{TGA}	Measured solid fraction
$S_{f,VLE}$	Solid fraction of the VLE species (mass of the condensed VLE species divided by the mass of the combined condensed and gas-phase VLE species)

τ	Number of broken bridges on the perimeter of a polymer fragment with *s*-bridges connecting n-sites
T	Temperature, K
T^o	Initial temperature of the system, element, or computational cell, K
T_o	Parameter used in optimization method to obtain prefactors
t	Time, s
T^*	Temperature normalized by the Lennard-Jones potential well depth, ε, and the Boltzmann constant, κ
T_c	Critical temperature, K
V	Moles of VLE vapor
$\tilde{V}_c$	Critical molar volume, cm^3/mol
V_e	Volume of element or computational cell, cm^3
V_g	Gas volume in an element or computational cell, cm^3
V_g^o	Initial gas volume in an element or computational cell, cm^3
V_p	Volume occupied by condensed mass in the element or computational cell, cm^3
$\Omega_{D_{AB}}$	Collision integral
ω_{BAS}	Mass fraction of *BAS*
ω_{BPA}	Mass fraction of *BPA*
$\omega_{C\text{-}residue}$	Ultimate *C-residue* mass fraction
ω_{DGEBA}	Initial mass fraction of DGEBA in the REF100 polymer
ω_i^{VLE}	Mass fraction of the VLE species
ω_L^o	Initial mass fraction of bridge L
$\omega_{L_1}^o$	Initial mass fraction of bridge L_1
$\omega_{L_2}^o$	Initial mass fraction of bridge L_2
$\omega_{L_3}^o$	Initial mass fraction of bridge L_3
ω_{MP}	Mass fraction of *MP*
$\omega_{L\text{-mer}}$	Mass fraction of the *L*-mers
$\omega_{n\text{-mer}}$	Mass fraction of the *n*-mers
ω_{OS}	Mass fraction of *OS*
$\omega_{OS\text{-}residue}$	Ultimate *OS-residue* mass fraction
ω_{RER1}	Initial mass fraction of RER1 in the REF100 polymer
$\omega_{XL\text{-mer}}$	Mass fraction of the *XL*-mer fragments
ξ	Vector representing the SREF model parameters
x_i	Mole fraction of the i^{th} gas-phase VLE species
ψ	Weighting function defined by eqn (36)
y_i	Mole fraction of the i^{th} condensed-phase VLE species
z	Number of standard deviations
z_i	Mole fraction of the i^{th} combined-phase VLE species
Z_{NV}	Mass fraction of the non-VLE species

Nomenclature

SREF – A SIMPLE REMOVABLE FOAM DECOMPOSITION CHEMISTRY MODEL

1. Introduction and Background

The United States has developed weapons with a safety theme that minimizes the possibility of inadvertent nuclear detonation in abnormal thermal environments. Consequently, US nuclear weapons are designed to be safe (less than 1 in 1,000,000 chance of inadvertent detonation) in fire environments. This is accomplished by designing components in the weapon to fail at specific temperatures. This design philosophy requires an accurate representation of the thermal environment within systems that are encapsulated with rigid, closed-cell foams.

This report describes a Simple Removable Epoxy Foam (SREF) decomposition chemistry model developed to predict the decomposition behavior of a closed-cell, rigid epoxy foam (REF) exposed to fire-like heat fluxes. REF is used to encapsulate shock and vibration sensitive components within metal enclosures. The enclosures may have cable openings that provide pathways for the decomposition gases to exit the system. Thus, the decomposition model should be able to predict mass loss for unconfined systems. Conversely, some enclosures may be hermetically sealed to prevent gases from entering or exiting the system. Consequently, the decomposition model must also have the ability to predict pressurization or liquid formation associated with confinement of the decomposition gases.

Traditionally, encapsulants were not designed for easy removal. These encapsulants were difficult to remove because of their cross-linking, solvent resistance, and mechanical toughness. Such encapsulants were removed for component maintenance by using aggressive solvents and/or mechanical chiseling, which can easily damage electronic assemblies. Loy et al. [1-3] have recently patented a method to make thermally removable epoxies that can be removed from potted assemblies with a mild solvent (e.g., n-butanol) at 90ºC. Removability was achieved by incorporating chemically labile linkages within the cross-linked polymeric network using the reversible Diels-Alder reaction. The reverse (retro) Diels-Alder reaction is favored by heating the foamed encapsulant to temperatures near 90ºC and a mild solvent promotes dissolution of the foam.

The SREF model was developed specifically for removable epoxy foam referred to as REF100 [3]. However, the formulation for the REF foam has evolved in order to increase the glass transition temperature to be well above normal design operating temperatures. Two additional formulations, referred to as REF200 and REF300, primarily differ in the amount of blowing and curing agents used in the synthesis. Rather than develop separate models for each new series of foam, a single mechanism was developed to describe decomposition of all three removable epoxy foam types. Decomposition of REF100, REF200, and REF300 type foam has been modeled using the same kinetic coefficients. The only differences in the decomposition model parameters are in the initial constituents making up the polymeric foam.

The framework used to develop the SREF model is based on three previously developed *polyurethane* foam decomposition models--referred to as the PUF, CPUF, and SPUF models [6-8]. The PUF [6] and CPUF [7] models were based on the chemical-structure of the polyurethane foam with 9 and 16 reaction steps, respectively. The overall RMS error between measured and predicted mass loss for a typical thermal gravimetric analysis (TGA) experiment for the PUF and CPUF models was 8% and 2%, respectively; suggesting that better predictions could be obtained by increasing the number of reaction steps. However, the derivative of the mass loss curves with respect to temperature for the polyurethane foam suggested that there were only two primary mass loss mechanisms. Consequently, the SPUF model [8] was developed based on two mass loss reactions using distributed activation energies. The significantly simplified SPUF model gave an RMS error between measured and predicted mass loss for a typical TGA experiment of 1%. Although the TGA mass loss predictions were better using the simpler SPUF model, gas-phase and condensed-phase compositions were not predicted, since the SPUF model was not based on the chemical structure of the polymer.

The SREF model discussed in the current report is based on improved concepts from the chemical-structure-based polyurethane models, PUF [6] and CPUF [7], yet uses a mass-based progress variable approach to obtain accurate mass loss predictions with a small number of reaction steps, similar to the SPUF model [8]. The SREF model has additional physics not in any of the previously developed polyurethane models. Not only is the SREF model based on the chemical structure of the removable epoxy foam polymer, but the model also includes adsorbed and/or absorbed gases (blowing agents and surfactants referred to as “sorbed” gases) that are not intimately bonded to the polymer.[*] The SREF network statistics model has also been simplified by using lattice sites without mass; assuming the polymer mass is located in the bridges that connect the sites. This new lattice structure allows specific bridge mass to be based on observed decomposition products. A mixed-product species was used to insure that the elemental composition of the SREF model polymer matched elemental composition of the REF polymer.

In the PUF and CPUF models, pressure dependent decomposition was accounted for by using a vapor-liquid-equilibrium (VLE) model. These models were capable of simulating TGA mass loss profile shifts to higher temperatures with higher pressures as measured in Brigham Young University’s (BYU) high pressure TGA (HPTGA) apparatus. However, the HPTGA apparatus did not confine the decomposition gases within the TGA sample pan since a high-pressure purge gas was used to sweep the gases away from the decomposing sample.

Erickson et al. [5] studied the effect of retaining the decomposition gases near the decomposing sample by using hermetically sealed aluminum sample pans with orifices as small as 0.06-mm (60-μm). Erickson et al. [5] observed a shift in the mass loss profile to higher temperatures, similar to the shift with pressure observed at BYU; however, Erickson’s samples were at ambient pressure. Confining the decom-

---

[*] *Absorption* is the process of taking in the blowing agent and surfactant as part of the condensed foam. *Adsorption* refers to adhesion in an extremely thin layer of molecules (gases, solutes, or liquids) to the surfaces of solid bodies or liquids with which they are in contact. *Absorbed* is used when the blowing agent and surfactant is taken up throughout the existent whole of the polymer and *absorbed* is used when the blowing agent and surfactant is taken up near the surface of the polymer. The word *sorbed* refers to either adsorption or absorption. The words *absorbed*, *adsorbed*, and *sorbed* are sometimes used interchangeably in this report.

position gases caused the mass loss profile to shift to higher temperatures as the orifice became smaller, even at atmospheric pressure. This shift with increasing levels of confinement is modeled in the current report using a mass transport resistance. As the concentration of gases build-up in the reaction cell, the driving potential for mass transport (concentration differences) decreases and the subsequent effect is a shift in the mass loss profile towards higher temperatures. In the SREF model, the mass transport resistance is modeled in parallel with the chemical resistance. These resistances are defined later in the report.

Two types of experiments were used to validate the SREF model—1) TGA experiments and 2) a hot-cell experiment. Numerous TGA experiments were used to validate the SREF decomposition chemistry model. The TGA experiments included 25 separate operating conditions covering pressures from ambient conditions to 70-atm, unconfined decomposition using open platinum pans, partially-confined decomposition using hermetically sealed aluminum pans with lids having various orifice sizes, sample temperature ramp rates from 5ºC/min to 50ºC/min, isothermal experiments with sample temperatures quickly ramped to various temperatures and held. The hot cell experiment considered dynamic pressurization caused by confining decomposition products within a reaction cell using an experiment originally designed for confinement of energetic materials. The hot cell experiment was used to measure the pressure in a constant volume reaction cell with temperature ramped from room temperature to 300ºC and held for 2 hours. The pressure in the cell increased due to generation of gaseous decomposition products.

This report only describes the SREF foam decomposition chemistry model. The SREF decomposition chemistry model was subsequently incorporated into a three-dimensional thermal diffusion finite element model that includes finite rate kinetics with enclosure radiation. The full three-dimensional foam response model will be discussed in a separate report. The remainder of this report describes the most probable structure of the removable epoxy foam as determined by Clayton [4]; the decomposition kinetics; the mass transport model; the polymer network used in the lattice statistics model; the vapor-liquid-equilibrium model; model parameters; auxiliary models to predict pressurization, viscosity, and reaction enthalpy; and validation using TGA experiments and a hot-cell experiment. The report ends with a summary and conclusion section.

2. Chemical Structure of the REF Polymer

Detailed information regarding the chemical structure of the removable epoxy foam (REF) polymer is required to predict foam decomposition using lattice statistics. Clayton [4] determined probable chemical structures for the REF polymer using molar ratios and postulating relative reactivities of functional groups. Clayton assumed the following reactive hierarchy for various functional groups associated with part of the resins: $-NH_2$, -OH associated with nonyl phenol > -NH > N, -OH associated with pentaerythritol triacrylate. Clayton also assumed that the amount of minor ingredients were negligible, the blowing agent and surfactant do not incorporate into the polymer structure, no reactions occur between pentaerythritol triacrylate (PETA) and the diglycidyl ether of bisphenol A (DGEBA), no small species were generated in the polymerization reactions, the reactivity of the acrylate groups are higher than the reactivity of the epoxy groups, etc. Clayton [4] gives more detail on the chemical structure of the REF polymer.

Figure 1 shows the most common repeating unit of the REF polymer, which is essentially an infinite network composed of various sites and bridges made from 5 primary ingredients used to synthesize the polymer: 1) diglycidyl ether of bisphenol A [DGEBA], 2) ancamine 2049, which is commonly called dimethyldicyane [DMDC], 3) a removable epoxy resin referred to as RER1 in [3], 4) pentaerythritol triacrylate [PETA], and 5) nonyl phenol [NP]. A small amount (2.35 wt.%) of n-aminoethylpiperazine [n-AEP] was also used to make the polymer. Table 1 gives the primary ingredients used to make the REF polymer. The elemental composition of the REF polymer listed in Table 2 was determined from the primary ingredients given in Table 1. The foam is composed of 80.8 wt% REF polymer (composition in Table 2), 14.1 wt% perfluorohexane (C_6F_{14}), and 5.1 wt% surfactant with a proprietary composition.

Figure 2 shows the most probable structural unit with 6 potential lattice sites. A site is a point from which a lattice or network can be propagated, by connecting to other sites. The exact definition of a site is discussed in more detail in the lattice statistics section of this report. Each of the graphic shapes corresponds to part of the polymer, which can propagate via reactive functional groups. For example, site 5, associated with PETA in Fig. 2, has four potentially reactive groups--three of the acrylate functional groups

Table 1. Chemical ingredients in the REF polymer [4]

Name	Acronym	Formula	Mw, g/mol	wt. %
diglycidyl ether of bisphenol A	DGEBA	$C_{21}H_{24}O_4$	340	16.8
dimethyldicyane	DMDC	$C_{15}H_{30}N_2$	238	21.7
removable epoxy resin [3]	RER 1	$C_{44}H_{56}N_2O_{15}Si_4$	964	42.0
pentaerythritol triacrylate	PETA	$C_{14}H_{18}O_7$	298	11.2
nonyl phenol	NP	$C_{15}H_{24}O$	220	6.0
n-aminoethylpiperazine	n-AEP	$C_6H_{15}N_3$	129	2.4

Table 2. Elemental composition of the REF polymer[1]

Element:	C	H	N	O	Si
wt. %:	64.4	8.0	4.5	18.2	4.9

[1] The REF foam is composed of 80.8 wt.% REF polymer, 14.1 wt.% perfluorohexane blowing agent (C_6F_{14}), and 5.1 wt.% surfactant (composition unknown). The REF polymer composition given in this table was determined from the ingredients in Table 1.

have already reacted and one functional group labeled as a hydroxyl group (-OH) can potentially react. The coordination number (σ+1) for site 5 is 4, which implies that this site can propagate the lattice from 4 locations. The average coordination number for the entire structural unit is 3. The critical bridge population for the REF lattice is $1/\sigma$ or 0.5 implying that the infinite lattice structure disappears when ½ of the bridges are unoccupied. The hexagonal graphic figure representing nonyl phenol is not considered a site since there are no lattice-propagating reactive groups associated with this moiety. The only reactive group on the nonyl phenol is the hydroxyl group, -OH. The hydroxyl group can react with other functional groups such as the acrylate groups associated with PETA or any of the hydrogen associated with the $-NH_2$ functional groups. Once the nonyl phenol's hydroxyl group reacts, there are no other functional groups to continue the chain propagation. Thus, nonyl phenol is considered a "terminating dangler" (terminology used in other network statistics models).

Figure 1 also shows a model REF polymer composed of the most probable structural unit shown in black and white. In Fig. 1, the removable epoxy resin (RER1) is shown connecting the white polymer sections to the black polymer segments. As the temperature is increased, these segments separate and cause the polymer to unzip. Of course the representative polymer in Fig. 1 is more orderly than would be expected in the actual polymer network, and the unzipping would create various polymer fragments that are soluble in mild solvents. When exposed to fire-like heat fluxes, the polymer will decompose and create polymer fragments that behave similarly to solvent-like molecules, which promote liquefaction of the REF polymer.

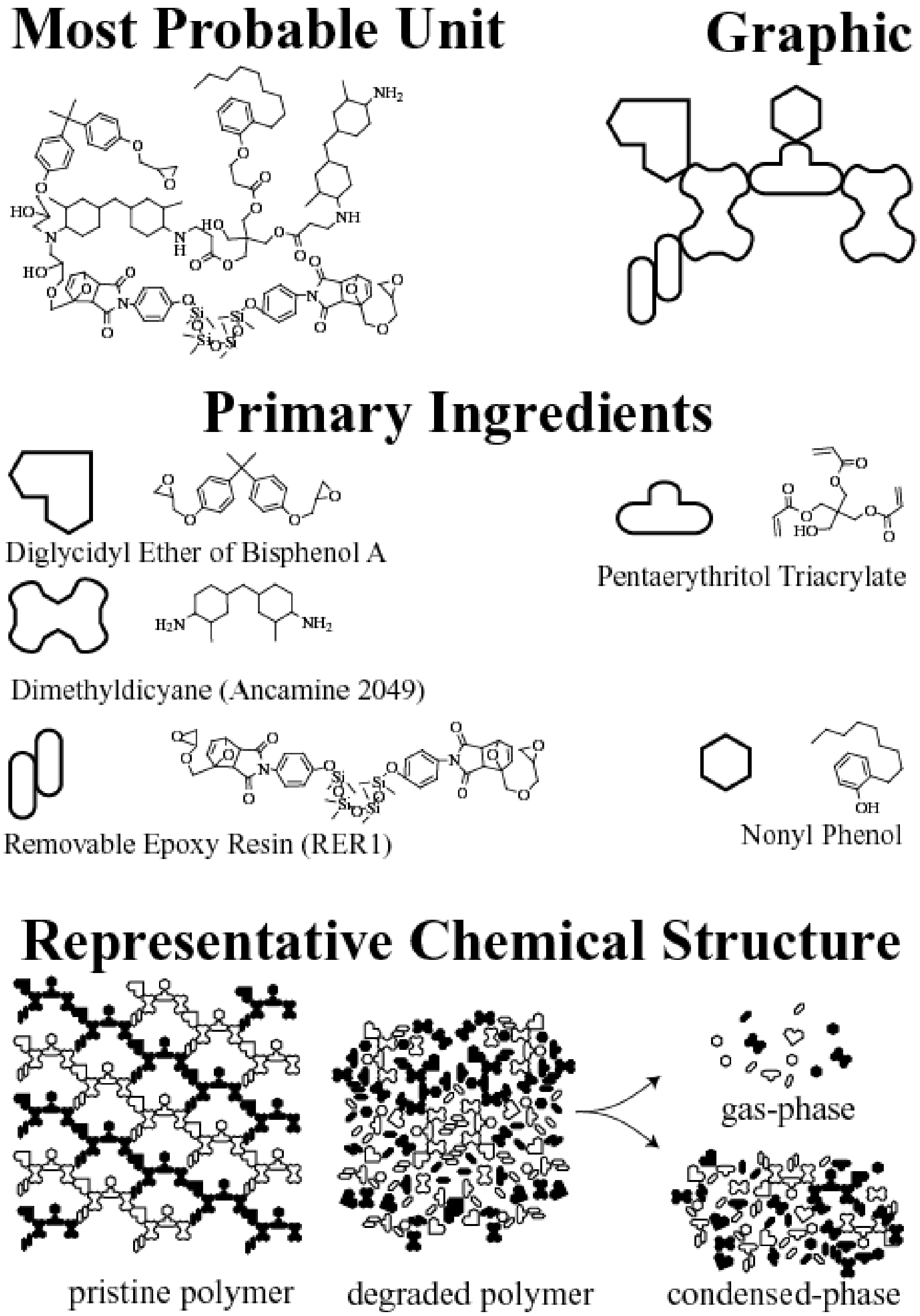

Fig. 1. Most common chemical structural unit and hypothetical chemical structure of the REF polymer. The graphic symbols represent ingredients used to make the polymer.

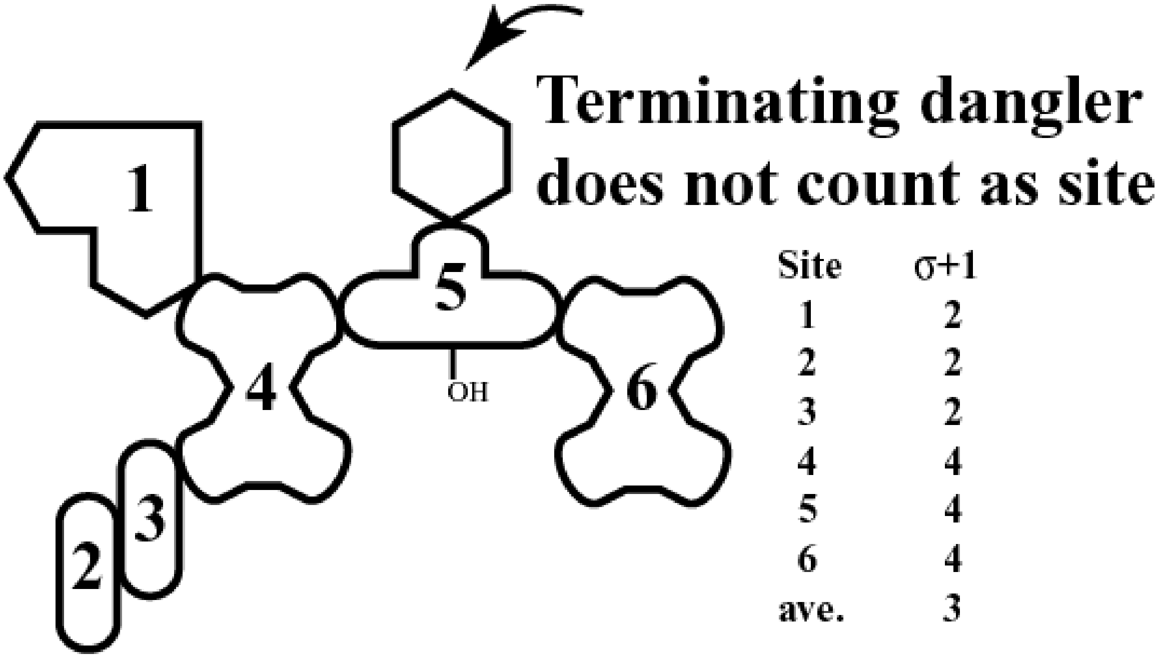

Site	σ+1
1	2
2	2
3	2
4	4
5	4
6	4
ave.	3

Fig. 2. Most probable structural unit showing 6 sites. σ+1 is the coordination number. The alcohol functional group on site 5 is a potential reaction site.

3. Kinetics

3.1 Observations

Figure 3.A shows a picture and schematic of a thermogravimetric analysis (TGA) apparatus. Figure 3.B shows the mass loss behavior of a 4.7-mg sample of REF foam that was heated at 20ºC/min in a the TGA apparatus at ambient pressure [4, 5]. The TGA apparatus is composed of 1) a microbalance used to measure mass loss associated with thermal decomposition, 2) a thermocouple in close proximity to the sample to determine sample temperature, and 3) purge gas to sweep away decomposition gases from the surface of the sample. Sample sizes were chosen to minimize size effects and to maximize the signal-to-noise ratio. TGA data from two laboratories [4,5] located at Brigham Young University (BYU) and Sandia National Laboratories (SNL) are presented in this report. The BYU experiments were performed in a high-pressure TGA apparatus (HPTGA, shown in Fig. 3.A) and the SNL experiments were performed in a low-pressure TGA apparatus (LPTGA). The HPTGA is capable of decomposition at pressures up to 100 bars, and results up to 70 bars are presented in the current report. A high thermal conductivity purge gas was needed in the HPTGA experiments to insure that the thermocouple temperature was sufficiently close to the sample temperature [4]. References [4] and [5] give more information regarding the HPTGA and LPTGA experiments, respectively.

The TGA records the sample mass (m) versus temperature (T) and time (t). Typically, the normalized sample mass or solid fraction ($S_f = m/m_o$) is plotted as a function of temperature or time. Figure 3 shows the TGA mass loss and rate of mass loss divided by the heating rate ($-dS_f/dT$) for a typical REF sample heated at 20ºC/min. The four peaks labeled A-D in Fig. 3.B indicate multiple, temperature-dependent reaction steps. The decomposition of REF involves multiple decomposition pathways that include both forward and reverse (retro) reactions. For example, the reverse Diels-Alder reaction occurs at temperatures near 100ºC.

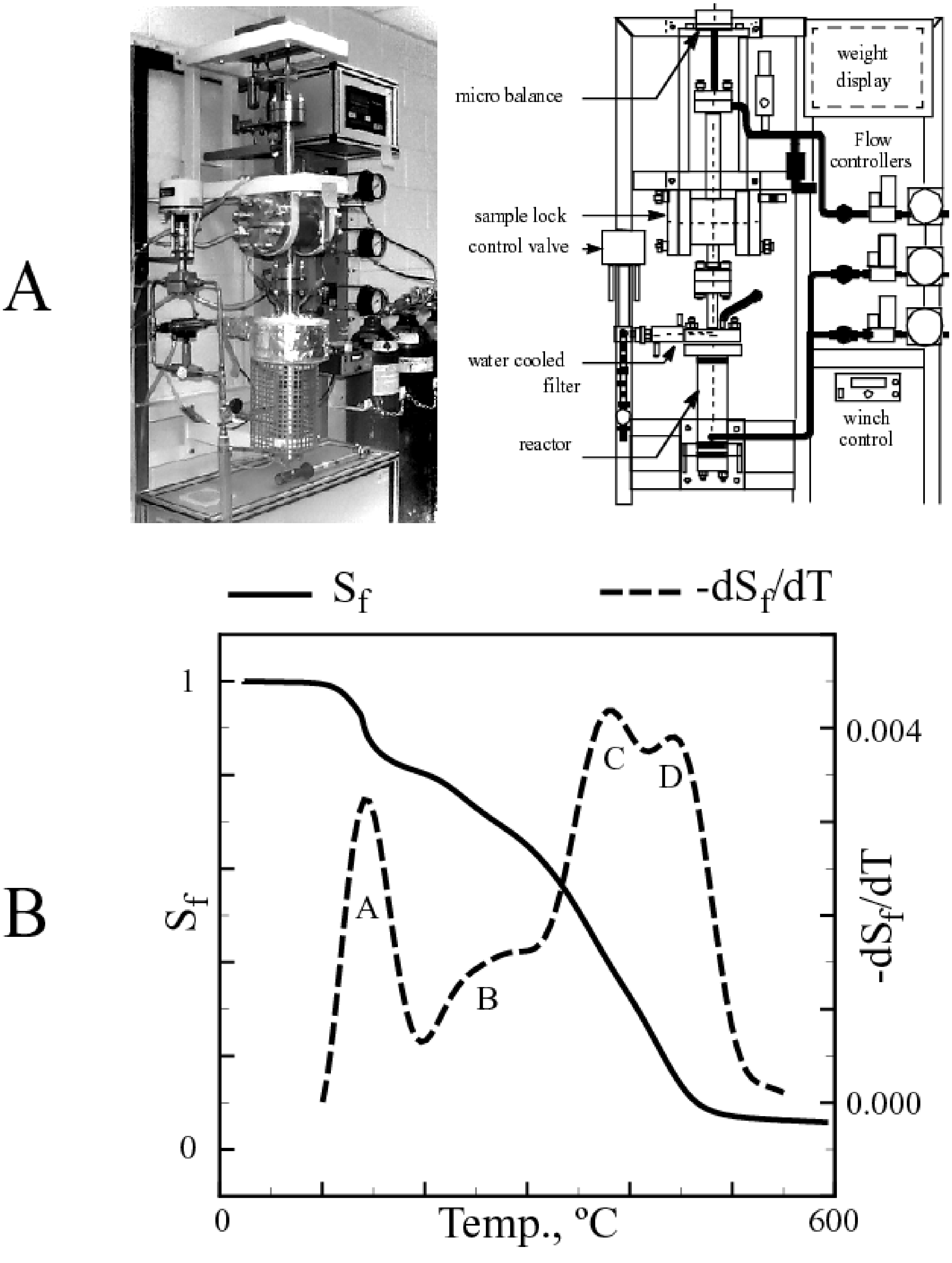

Fig. 3. A) Picture and schematic of HPTGA [4]. B) TGA mass loss and rate of mass loss from unconfined 4.7 mg REF sample heated at 20ºC/min [4]. In B, A-D show four primary decomposition steps.

Erickson et al. [5] have monitored the decomposition gases from the TGA using real-time FTIR and have periodically analyzed gas samples using a gas chromatograph and mass spectrometer (GC/MS). From room temperature to about 140ºC, the most abundant decomposition products are the blowing agent (perfluorohexane, C_6F_{14}, b.p. 58-60ºC) and siloxanes associated with the surfactant, which corresponds to peak A in Fig. 3.B. From about 140-300ºC, the major decomposition product is octamethylcyclotetrasiloxane (OS, B.P. 175-176ºC), corresponding to peak B in Fig. 3.B. The OS peak was not observed for the partially-confined experiments using small orifice sizes. Peak C and D are associated with a mixture of organic products that include 2-methylfuran, phenol, toluene, nonylphenol (NP), and bisphenol-A (BPA). Less volatile products such as BPA are probably more prevalent in the fourth peak labeled D in Fig. 3.B.

3.2 Mechanism

The minimum number of reactions needed to reproduce the mass loss rate profiles shown in Fig. 3.B is four. Since the SREF mechanism will be used for computationally intense three-dimensional finite element simulations, a minimum number of reaction steps were desired, even though known reversible reactions are present at lower reaction temperatures (e.g. retro Diels-Alder reaction). The four-step SREF reaction mechanism is given in Table 3 along with rate equations, populations and initial conditions.

Table 3. Mechanism, rate equations, and initial conditions for the SREF model

Reactions	**Mechanism**	**Rate Equations**	**Populations**	**Initial Conditions**[1]		
				REF100	**REF200**	**REF300**
1	$S \xrightarrow{1} BAS$	$r_1 = k_1 S$	S	0.192	0.150	0.130
2	$L_1 \xrightarrow{2} OS$	$r_2 = k_2 L_1$	L_1	$0.104\times(1-f_{OS})$	$0.104\times(1-f_{OS})$	$0.104\times(1-f_{OS})$
3	$L_2 \xrightarrow{3} MP$	$r_3 = k_3 L_2$	L_2	0.563	0.537	0.589
4	$L_3 \xrightarrow{4} BPA$	$r_4 = k_4 L_3$	L_3	0.091	0.091	0.091
			$S+L_1+L_2+L_3$	0.950	0.882	0.914
			C-residue	0.050	0.118	0.086
			OS-residue	$0.104\times f_{OS}$	$0.104\times f_{OS}$	$0.104\times f_{OS}$

[1] The initial L_1 condition has an empirical confinement model to predict the "ultimate" OS-residue. The term "ultimate" is used to describe the fixed compositions of the residues throughout the SREF calculation. The residue fractions are assumed to be at the equilibrium value and are not determined with any kinetic reaction mechanism. f_{OS} is the fraction of the L_1 bridges that ultimately end up in the residue and is correlated to pressure and confinement [see eqns (7) and (8)].

The mass-based populations; *S*, L_1, L_2, and L_3; represent the “sorbed” blowing agent and surfactant (BAS), the labile bridges composed of octamethylcyclotetrasiloxane (OS), the labile bridges composed of mixed products (MP), and the labile bridges composed of bisphenol-A (BPA), respectively. *BAS*, *OS*, *MP*, and *BPA*[*] are also mass-based population variables; and rate equations can also be written for each of these variables. However, since there are no reversible reactions in the SREF mechanism, the populations of *BAS*, *OS*, *MP*, and *BPA* can be obtained using conservation of mass as follows:

$$BAS = S^o - S \tag{1}$$

$$OS = L_1^o - L_1 \tag{2}$$

$$MP = L_2^o - L_2 \tag{3}$$

$$BPA = L_3^o - L_3\,, \tag{4}$$

where $S^o, L_1^o, L_2^o,$ and L_3^o represent the initial mass fraction of the “sorbed” blowing agent and surfactant, the siloxane moiety in the removable resin (RER1) that decomposes as octamethylcyclotetrasiloxane at high temperatures, the portion of the polymer that evolves as a variety of mixed products at high temperatures, and the portion of the polymer that decomposes into bisphenol-A at elevated temperatures.

3.3 Initial Conditions

The initial mass fraction of the “sorbed” blowing agent (0.141) and surfactant (0.051) is based on the REF100 formulation as reported by Clayton [4]. For simplicity, the blowing agent and the surfactant are treated in the SREF model as one pseudo species, referred to as BAS. The molecular weight of the S and BAS was taken to be 120 g/mol based on the molecular weight of the blowing agent, perfluorohexane (C_6F_{14}, 338 g/mol), and the molecular weight contribution of the surfactant. The composition and molecu-

---

[*] *BAS*, *OS*, *MP*, and *BPA* are italicized when referring to the population variables. BAS, OS, MP, and BPA are not italicized when referring to the species.

lar weight of the surfactant is a commercial trade secret and was not made available. Thus, the average molecular weight of *BAS* is an estimate.

Clayton [4] reported the initial mass fraction of RER1 in the REF100 polymer, ω_{RER1}, as 0.42 which can be used to determine the initial siloxane moiety in the removable resin (RER1) that decomposes as octamethylcyclotetrasiloxane at high temperatures, L_1^o, as follows:

$$L_1^o = (1 - S^o)(\omega_{RER1})\left(\frac{M_{OS}}{M_{RER1}}\right) = (1 - 0.192)(0.42)\left(\frac{296}{964}\right) = 0.104\,, \tag{5}$$

where M_{OS} and M_{RER1} represent the molecular weights of octamethylcyclotetrasiloxane (296 g/mol) and the removable epoxy resin (964 g/mol), respectively. The term $(1 - S^o)$ is used to convert the mass fraction from a polymer basis to a foam basis that includes blowing agent and surfactant. Similarly, the initial portion of the polymer that decomposes into bisphenol-A (BPA) at elevated temperatures, L_3^o, can be determined using the initial mass fraction of DGEBA in the REF polymer, ω_{DGEBA}, reported by Clayton [4] as 0.168:

$$L_3^o = (1 - S^o)(\omega_{DGEBA})\left(\frac{M_{BPA}}{M_{DGEBA}}\right) = (1 - 0.192)(0.168)\left(\frac{228}{340}\right) = 0.091\,, \tag{6}$$

where M_{BPA} and M_{DGEBA} represent the molecular weight of BPA (228 g/mol) and DGEBA (340 g/mol), respectively.

Figure 3 shows that about a 5 wt% solid fraction remains in the TGA pan at the end of the experiment. This "residue" is primarily composed of carbon, but may contain hydrogen, nitrogen, oxygen and silicon. Residue from most of the unconfined low pressure REF100 TGA experiments at low pressure was near 5 wt%. Thus, 5 wt% of the initial population was assumed to form a nonvolatile residue as listed in Table 3 as *C-residue*. The *C-residue* is assumed to be composed of carbon. At elevated pressures and increased levels of confinement, the residue was slightly greater than the 5 wt% observed in the low pressure, unconfined experiments. To account for these slight differences, an empirical correlation was used to force residue mass fraction to increase a little with increasing pressure and confinement.

The ultimate weight fractions of the residues, $\omega_{C\text{-}residue}$ and $\omega_{OS\text{-}residue}$, are also the initial conditions for the *C-residue* and *OS-residue* in Table 3. The term “ultimate” is used to describe the fixed compositions of the residues throughout the SREF calculation. The *C-residue* and *OS-residue* fractions are assumed to be at the equilibrium value and are not determined with any kinetic reaction mechanism. The weight fraction of the *C-residue* was assumed to be constant regardless of confinement or pressurization. However, for unconfined decomposition, the fraction of the L_1 bridge converted to *OS-residue* was assumed to be a function of pressure based on the following empirical equation:

$$f_{OS} = 0.005\left(P-1\right), \tag{7}$$

where P is in atmospheres and $0 \leq f_{OS} \leq 1$. For partially-confined decomposition,

$$f_{OS} = 0.444 - 0.000101 d_{orifice} \tag{8}$$

where $d_{orifice}$ is in micrometers and $0 \leq f_{OS} \leq 0.444$. For fully-confined decomposition f_{OS} is set to 0.444. The empirical correlations in eqns (7) and (8) were used to force the residue mass fraction to increase a little with increasing pressure and confinement. Equation (7) was determined using the HPTGA data. Equation (8) was determined simultaneously with the d^*/ϕ parameters using the partially-confined TGA data from [4].

The initial mixed product mass fraction, L_2^o, was determined by using an overall mass balance:

$$L_2^o = 1 - residue - S^o - L_1^o - L_3^o = 1 - 0.05 - 0.104 - 0.091 = 0.563\ . \tag{9}$$

The only difference between the REF100, REF200 and REF300 series foam is the initial mass fractions of S and L_2 that eventually form *BAS* and *MP*. The initial populations for the REF100, REF200, and REF300 series of foam are given in Table 3.

3.4 Distributed Activation Energies

The four SREF reactions were distributed normally with respect to the extent of reaction to approximate the effect of thermal damage. Thermal damage includes mechanical damage such as cracks, fissures, density changes, and phase change as well as chemical damage caused by thermal decomposition. The SREF model considers distributed activation energies for each of the reactions shown in Table 3. For the desorption reaction (reaction 1 in Table 3), the activation energy was distributed based on the extent of reaction 1 as follows:

$$\Phi(z) = 1 - S / S^o = \int_{-\infty}^{z} \tfrac{1}{\sqrt{2\pi}} \exp(-\tfrac{1}{2} z^2) dz \tag{10}$$

where 1-S/S^o and z represent the extent of the BAS desorption reaction and the ordinate of the cumulative distribution function (CDF) representing the number of standard deviations above or below the mean activation energy, respectively.

All of the polymer degradation reactions (reactions 2-4 in Table 3) were distributed based on the extent of bridge breaking as follows:

$$\Phi(z) = 1 - p = \int_{-\infty}^{z} \tfrac{1}{\sqrt{2\pi}} \exp(-\tfrac{1}{2} z^2) dz \ , \tag{11}$$

where p is the normalized bridge population calculated using

$$p = \left(L_1 + L_2 + L_3\right) / \left(1 - S^o\right) . \tag{12}$$

The factor $\left(1 - S^o\right)$ is used to normalize the populations to convert from a foam basis to a polymer basis. The normalized bridge population is used in the lattice statistics model discussed further in Section 5.

The cumulative distribution function (CDF), Φ, and the probability density function (PDF) of a standard normal distribution are shown in Fig. 4. Figure 4 also gives an example for an instance where the extent of reaction is 0.8413. In Fig. 4, the shaded area under the PDF corresponds to a Φ-value of 0.8413, which corresponds to a z-value of 1. Thus, when the extent of reaction is 0.8413, the activation energy is evaluated at the mean plus one standard deviation above the mean.

Kinetics

As shown in Table 3, the four reaction rates, r_1 through r_4, were assumed to be first order in S, L_1, L_2, and L_3, respectively. Reverse reactions were not included in the SREF kinetic mechanism. The rate constants, k_j, given in Table 3 are effective rate constants, $k_j = 1/[(1/k_j^c + 1/k_j^m)]$, that include both kinetic and mass transport resistances. The kinetic rate constants, k_j^c, include the effect of the distributed activation energies as follows:

$$k_j^c(T) = A_j \exp\left[-\left(E_j + z_j\sigma_j\right)/RT\right] \tag{13}$$

where A, E, z, σ, R, and T represent the pre-exponential factor, activation energy, number of standard deviations as given in eqns (10) and (11), standard deviation of the activation energy, gas constant, and temperature, respectively. The subscript j refers to reactions 1-4 listed in Table 3. Distributing the activation energies tends to smooth the mass loss reaction rates and eliminates abrupt changes in calculated solid fractions, which is in agreement with experimental observations. The effective rate constants, k_j, and the mass transport rate constants, k_j^m are discussed further in the following mass transport section.

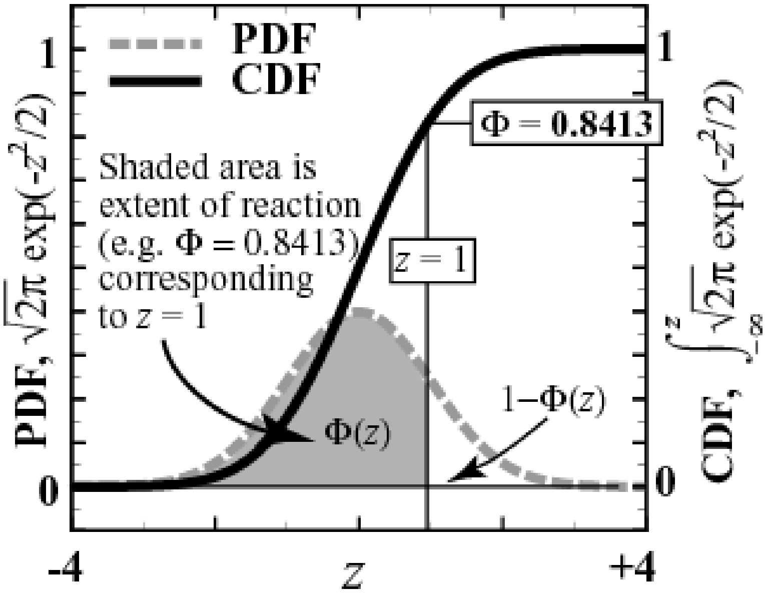

Fig. 4. Cumulative distribution function (shaded) of a standard normal curve.

4. Mass Transport

In the SREF kinetic mechanism, *S*, L_1, L_2, L_3 represent the populations of potentially volatile species. *BAS*, *OS*, *MP*, and *BPA* represent mixed-phase or combined-phase mass fractions. An expression for the effect of mass transport will be derived using the desorption reaction (reaction 1). Figure 5 shows a unit foam cell with blowing agent and surfactant adsorbed onto a polymer strut. In Fig. 5, the "sorbed" species diffuses to the surface of a bubble. Let *S** represent the population of the blowing agent and surfactant absorbed on to the REF polymer. The rate of desorption from the polymer can be written:

$$r_1^c = k_1^c (S^*) , \tag{14}$$

which is similar to the desorption rate equation given in Table 3, except that the rate constant is the chemical rate constant, k_1^c, given in eqn (13) rather than the effective rate constant, k_1. Another difference is that the driving potential for the chemically limited reaction in eqn (14) is S^*, which is the population of adsorbed gases at the reaction site.

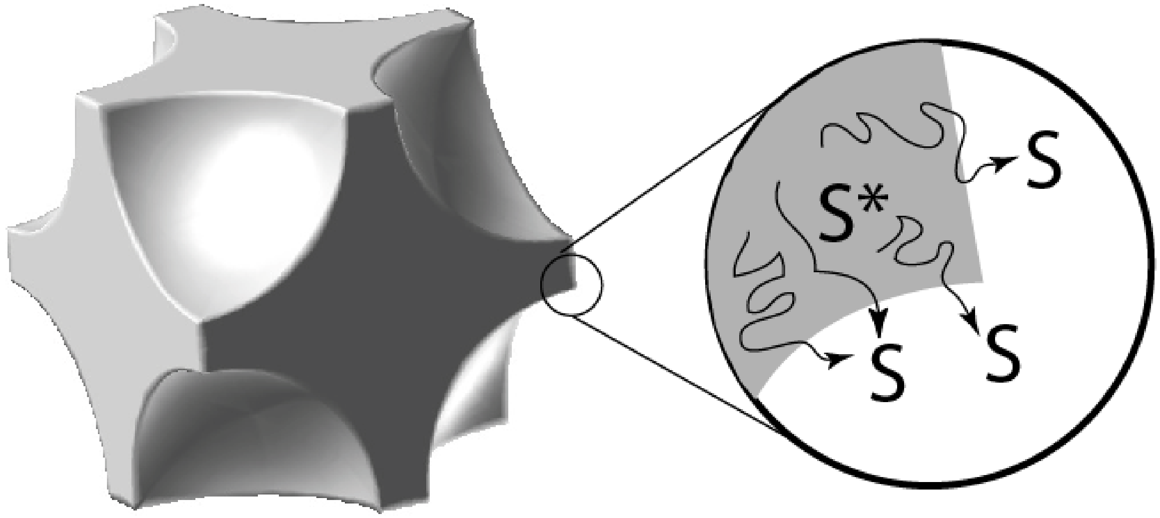

Fig. 5. Unit foam cell showing the "sorbed" species at the reaction site and the tortuous diffusion path to the bulk gas within a bubble.

The rate of diffusion of the “sorbed” species from the site of the reaction to a neighboring surface, which may be a bubble in the polymer matrix, is given by the following equation:

$$r_1^m = k_1^m (S - S^*) \,, \tag{15}$$

where the driving potential is the concentration difference between the population at the reaction site (S^*) and the population in the bulk mixture (S). k_1^m is the effective mass transport coefficient, which accounts for condensed-phase and film diffusion.

The population at the reaction site (S^*) can be eliminated by setting the desorption rate equal to the diffusion rate ($r_1 = r_1^c = r_1^d$) given in eqns (14) and (15). The reaction rate expression becomes:

$$r_1 = \frac{1}{\dfrac{1}{k_1^c} + \dfrac{1}{k_1^m}} S \,. \tag{16}$$

In a similar fashion, the general form of the effective rate constants for all four SREF reactions can be written as:

$$k_j = \left(\frac{1}{k_j^c} + \frac{1}{k_j^m} \right)^{-1} = \frac{1}{R_j^c + R_j^m} \,, \tag{17}$$

where k_j^c is given in eqn (13) and k_j^m is the effective mass transport coefficient. R_i^c and R_i^m are resistances due to chemistry and mass transport, respectively. The chemical resistance is only a function of the kinetic rate constant given by eqn (13). The effective mass transport resistance can be determined from the following equation:

$$R_j^m = \frac{1}{k_j^m} = \frac{S_f d^*}{2 D_j^e} \,, \tag{18}$$

where S_f, d^*, and D_j^e represent the solid fraction discussed previously, the characteristic diffusion length, and the effective diffusivity for the j^{th} reaction in the reacting foam and film. Equation (18) describes the resistance of the decomposition products as they move from the reaction site to the bulk gas. The product $S_f \times d^*$ is the characteristic diffusion length, which forces the diffusion resistance to behave correctly in the limit as the condensed mass approaches zero. Equation (18) was derived assuming heat and mass transport are analogous as discussed by Bird et al. [16]. The factor “2” in the denominator of eqn (18) is the Sherwood number for a motionless fluid. As the solid fraction goes to zero, the mass transport resistance in the foam also approaches zero. Equation (18) is discussed further in Section 4.2.

4.1 Effective Diffusivity

The effective diffusivity, D_j^e, can be estimated using the molecular diffusivity, D_j^m, as follows:

$$D_j^e = \phi D_j^m \tag{19}$$

where ϕ is a constant that is based on the developing porosity of the degraded foam. Laurendeau [9] shows that ϕ can be estimated by the porosity of the degraded material divided by two. The value two is an estimate of the tortuosity squared. Laurendeau [9], Walker et al.[10], Park and Edgar [11], Thorsness and Kang [12], Wang and Wen [13], and Hobbs et al. [14] give more information and other methods of calculating effective diffusivities. Hobbs et al.[14] used a value between 0.03 and 0.3 for decomposition in large coal particles in fixed-bed gasifiers. For the REF foam, ϕ is expected to vary between 0.001 and 0.1.

Gas theory is appropriate for diffusion of gases in solids with complex, evolving pore structures. The effective diffusivity approach utilized by the SREF model has also been used by many investigators to model mass transport in reactive systems (e.g. refs [9-14]). Froment and Bishoff [15] discuss using effective diffusivities to describe diffusion in porous catalyst with the same form used by the SREF model [eqn (19)]. Other diffusion models [15] such as the “dusty-gas” model, random pore model, parallel cross-linked pore mode, the pore network mode, etc. could have been used in the SREF model with added complexity. However, each of these models also requires information such as the porosity and tortuosity of the developing solid, and the added complexity of these alternative models is not warranted. However, the SREF model provides a framework for implementation of these mass transport models.

The molecular diffusivity for binary mixtures of arbitrary species *A* and *B* can be determined using Chapman-Enskog kinetic theory as discussed by Bird et al.[16]:

$$D_{AB}^{m} = 0.0018583 \times \frac{\sqrt{T^3\left(\frac{1}{M_A}+\frac{1}{M_B}\right)}}{P\sigma_{AB}^2\Omega_{D_{AB}}}, \tag{20}$$

where *T*, *M*, *P*, σ, and Ω represent temperature (K), molecular weight (g/mol), pressure (atm), collision diameter (Å), and collision integral (dimensionless), respectively. The diffusivity of adsorbed gas population (*S*) and polymer fragments (L_1, L_2,and L_3) is more complicated than given in eqn (20); however, the temperature and molecular weight dependencies are probably acceptable for both the sorbed gases and the polymer fragments. The pressure dependency for the sorbed gases and polymer fragments are not expected to follow Chapman-Enskog theory since the populations behave more like fluids than gases.

To simplify the diffusivity calculation, the diffusivity of the "sorbed" species populations were assumed to have the following temperature and pressure dependency:

$$D_{S}^{m} = D_{S,STP}^{m}\left(\frac{T}{298.15}\right)^{1.5} \Big/ \sqrt{P}, \tag{21}$$

where $D_{S,STP}^{m}$ is the mass diffusivity of the blowing agent and surfactant that are absorbed within the foam at standard temperature and pressure (STP) assumed to be 298.15 K and 1 atm. The temperature dependency is assumed to be the same as predicted using Chapman-Enskog theory; however, the pressure has an inverse square-root dependency rather than a simple inverse dependency.

The mass diffusivity for the polymer fragments, D_{L}^{m}, are also assumed to have the same temperature dependency as Chapman-Enskog theory:

$$D_{L}^{m} = D_{L,STP}^{m}\left(\frac{T}{298.15}\right)^{1.5}. \tag{22}$$

However, the diffusivities of the polymer fragment populations are assumed to be independent of pressure. Theoretical liquid diffusivities as well as empirical diffusivity correlations are also independent of pressure

[16]. The dependence on pressure is more significant for gases, somewhat significant for "sorbed" gases, insignificant for the condensed polymer fragments.

Equation (20) was used to estimate the diffusivities at standard temperature (298.15 K) and pressure (1 atm) by assuming self-diffusion rather than complex multi-component diffusion as follows:

$$D_{i,STP}^{m} = 0.0018583\times\left(298.15\right)^{1.5}\frac{\sqrt{\left(2/M_i\right)}}{\sigma_i^2\Omega_{D_i}} \tag{23}$$

The collision diameter, σ_i, can be estimated using the critical molar volume in cm^3/mol, $\tilde{V}_c$, using simple corresponding state theory with Argon as the reference state [16]:

$$\sigma_i = 0.841\tilde{V}_c^{1/3}. \tag{24}$$

The collision integrals, Ω_{D_i}, have been correlated with the following equation [16]:

$$\Omega_{D_i} = \frac{1.06036}{T^{*0.15610}} + \frac{0.19300}{\exp(0.47635T^*)} + \frac{1.03587}{\exp(1.52996T^*)} + \frac{1.76474}{\exp(3.89411T^*)}, \tag{25}$$

where T^* is temperature normalized by the Lennard-Jones potential well depth, ε, and the Boltzmann constant, κ:

$$T^* = \kappa T/\varepsilon. \tag{26}$$

ε/κ can also be obtained using simple corresponding state theory using the following equation:

$$\varepsilon/\kappa = 0.77T_c \tag{27}$$

where T_c is the critical temperature in K.

Table 4 gives the populations, species associated with the populations, molecular weights, critical temperatures, critical volumes, characteristic diameters, potential well depths normalized by the Boltzmann constant, dimensionless temperature, collision integral, and STP diffusivities for SREF reactions 1-4. Properties of the S and L_2 populations were also estimated. The diffusivities listed in Table 4 are for the product species. The SREF model does not require the diffusivities for the reactants, which are the sorbed gases and the foam polymer. The product species represented by BAS, OS, MP, and BPA are really mixtures of products. The assumption implied by Table 4 is that the molecular diffusivities of these mixtures at STP can be represented by the "pure component" diffusivities listed in Table 4.

Table 4. Mass transport parameters used to calculate molecular diffusivity at STP with eqn (23)

Reactions	**Populations**	**Species**	**M, g/mol**	**T_c, K**	**V_c, cc/mol**	**σ (Å)**	**ε/κ, K**	**T^*_{STP}**	**Ω_{Di}**	**$D^m_{i,STP}$**
1	S	*BAS*	120[1]	451[2]	2045[2]	10.7	371	0.80	1.612	0.0067
2	L_1	*OS*	296	587	970	8.3	482	0.62	1.845	0.0062
3	L_2	*MP*	140[3]	694[4]	229[4]	5.1	570	0.52	2.026	0.0213
4	L_3	*BPA*	228	849	677	7.4	698	0.43	2.238	0.0073

[1] M estimated from blowing agent ($C_6F_{14,}$ 338 g/mol) and surfactant of unknown molecular weight

[2] Critical properties from product specification sheet for blowing agent, FC72

[3] M estimated from mixed products such as furan (68 g/mol), phenol (94 g/mol), cresols (108 g/mol), etc.

[4] Critical properties from phenol

4.2 Diffusion Parameters

By combining eqns (18) and (19), the resistance due to diffusion can be written in terms of the solid fraction (S_f) , characteristic diffusion length (d^*), ratio of the effective diffusivity to the molecular diffusivity (ϕ), and molecular diffusivity (D_j^m) as follows:

$$R_j^m = \frac{S_f d^*}{2\phi D_j^m} \ . \tag{28}$$

The solid fraction is determined assuming vapor-liquid-equilibrium between the sorbed gases and polymer fragments determined using the SREF kinetic mechanism and the lattice statistics model discussed further in Section 6. The specific method of determining the solid fraction will be deferred to the vapor-liquid-equilibrium section of this report. Determination of molecular diffusivity, D_j^m , was discussed in Section 4.1. The molecular diffusivity for reaction 1 was given by eqn (21) and the molecular diffusivities for the polymer reactions 2-3 was given by eqn (22). The diffusivities at STP for these four reactions were given in Table 4.

Equation (28) was determined using the well-known Chilton Colburn relationship. The Chilton Colburn relationship is a convenient method to obtain mass transfer coefficients from an applicable heat transfer correlation by substituting the dimensionless Nusselt (Nu) and Prandtl (Pr) number by the Sherwood (Sh) and Schmidt number (Sc) with Reynolds number (Re) unchanged. The limiting value of Nu for heat transfer from spheres at low Reynolds numbers is 2 (see ref 16, problem 10.B.1 on p 321). Thus by the Chilton Colburn analogy:

$$Sh = k_j^m L / D_j^e = 2\,. \tag{29}$$

L is the dynamic diffusion length defined as $S_f d^*$ and the effective diffusivity, D_j^e, is determined from eqn (19) as ϕD_j^m giving

$$Sh = k_j^m d^* / \phi D_j^m = 2\,. \tag{30}$$

giving

$$R_j^m = 1/k_j^m = \frac{S_f d^*}{2\phi D_j^m}\,, \tag{31}$$

which is the same as eqn (28).

The only unknown diffusion parameters in eqns (28) and (31) are the characteristic diffusion length, d^*, and the ratio of the effective diffusivity to the molecular diffusivity, ϕ. d^* is related to the distance from the reaction site to the bulk gases that surround the REF polymer, and ϕ is related to the porosity and tortuosity of the degraded material. Diffusion of the desorbed gases and polymer fragments is a complex problem that is not completely understood. When exposed to high heat fluxes, the REF polymer softens at the glass transition temperature and can liquefy at higher temperatures. The physical structure of the original foam is different than the degraded foam; although the original bubble structure within the foam may act as nucleation sites where decomposition products accumulate. Reaction products either diffuse directly to the surface of the foam polymer or to nearby bubbles that are convectively transported to the foam polymer surface. Diffusion to a bubble is assumed to be slower than convective bubble transport.

In the SREF model, the unknown diffusion parameters, d^*/ϕ for reactions 1-4, were chosen empirically using unconfined TGA experiments and partially-confined TGA experiments. As mentioned in

Section 4.1, ϕ for the REF polymer may range from 0.001 to 0.1. For an effective diffusion length of 0.2-cm, d^*/ϕ may range between 2 and 200 cm. The value of d^*/ϕ may even be less than this range for the adsorbed species since the effective diffusion length for the adsorbed species is probably less than the diffusion length for the polymer fragments. As a starting point, d^*/ϕ for the SREF model was chosen to be 2 for the unconfined TGA data. Partially-confined TGA data were used to further refine the d^*/ϕ estimates. The partially-confined TGA data were obtained using hermetically sealed aluminum sample pans with various orifice diameters used to restrict the gases from leaving the TGA pan. The SREF model formulation assumes that mass transport resistance is responsible for mass loss profiles shifting to higher temperatures as orifice diameters decrease.

The SREF model formulation further assumes that constant values of d^*/ϕ can be used for unconfined decomposition as well as fully-confined decomposition. For partially-confined decomposition, d^*/ϕ values were assumed to be empirical functions of the orifice diameter. The basis of the d^*/ϕ assumption is that the concentration of the bulk gases within the reaction cell varies with the orifice diameter. As the orifice diameter becomes smaller, the concentration of the decomposition products in the bulk gas increases since the gas does not freely exit the reaction cell, causing the driving potential for diffusion to decrease. Consequently, the reaction rates decrease with smaller and smaller orifice diameters causing the TGA mass loss profiles to shift to higher temperatures. For fully-confined decomposition, the decomposition gases are not allowed to leave the vicinity of the decomposing foam polymer. For fully-confined decomposition d^*/ϕ's were obtained by taking the limit as $d_{orifice}$, approaches zero.

For unconfined decomposition; the empirical values of d^*/ϕ used in the SREF model are:

$$\left(d^* / \phi\right)_{BA}^{unconfined} = 0.542 \tag{32}$$

$$\left(d^* / \phi\right)_{S}^{unconfined} = 2 \tag{33}$$

$$\left(d^* / \phi\right)_{L_1}^{unconfined} = \left(d^* / \phi\right)_{L_2}^{unconfined} = \left(d^* / \phi\right)_{L_3}^{unconfined} = 2\,, \tag{34}$$

where the subscripts *BA*, *S*, and *polymer fragments* refer to the blowing agent; surfactant; and polymer fragments L_1, L_2, L_3; respectively. The superscript, *unconfined*, refers to decomposition where the reacted products are not constrained to be near the degrading foam.

Note that the d^*/ϕ for the blowing agent and surfactant are different, even though a single species, BAS, is used to describe these products. In the SREF model, separate mass transport values are used for the blowing agent (BA) and surfactant (S) to reflect differences in mass transport for these two species. Figure 6.A shows the necessity of using separate d^*/ϕ for the blowing agent and surfactant. In Fig. 6.A, different mass loss rates are shown at the onset of decomposition for TGA samples ramped at 20ºC/min in partially-confined sample pans with orifice diameters ranging from an open pan to a 60-μm orifice. The polymer does not degrade appreciably at the onset of mass loss; and the primary gas-phase products from 90ºC to 140ºC are FC-72, which is the blowing agent (BA), and some siloxanes (S) associated with the surfactant [5]. As the orifice diameter decreases (i.e. level of confinement increases), the TGA profiles shift to higher temperatures. Figure 6.A also shows that the mass loss profiles are not smooth. A change in the rate of mass loss occurs near the "transition boundary" that is marked with a thick gray line in Fig. 6.A.

In Fig. 6.A, the TGA profile shift with confinement is modeled as a mass transport effect. Diffusion is assumed to be different for the blowing agent (BA) and the surfactant (S). To incorporate these differences, d^*/ϕ for the BAS species was determined using the following equation:

$$\left(d^*/\phi\right)_{BAS} = \left(1-\psi\right)\times\left(d^*/\phi\right)_{BA} + \psi\left(d^*/\phi\right)_S, \tag{35}$$

where the weighting function, ψ plotted in Fig. 6.B, is

$$\psi = 0.5\times\left[1-\tanh\left(\frac{1-S_f-G_{f,transition}}{width}\right)\right]. \tag{36}$$

The transitional gas fraction, $G_{f,transition}$, was obtained using data from 14 TGA experiments (runs 13-16, 27-36), which are described in detail later in this report. The width of the transition denoted as *width* was chosen to be 0.001 for the simulations in the current report. Fig. 7.A shows the transitional gas fraction as a

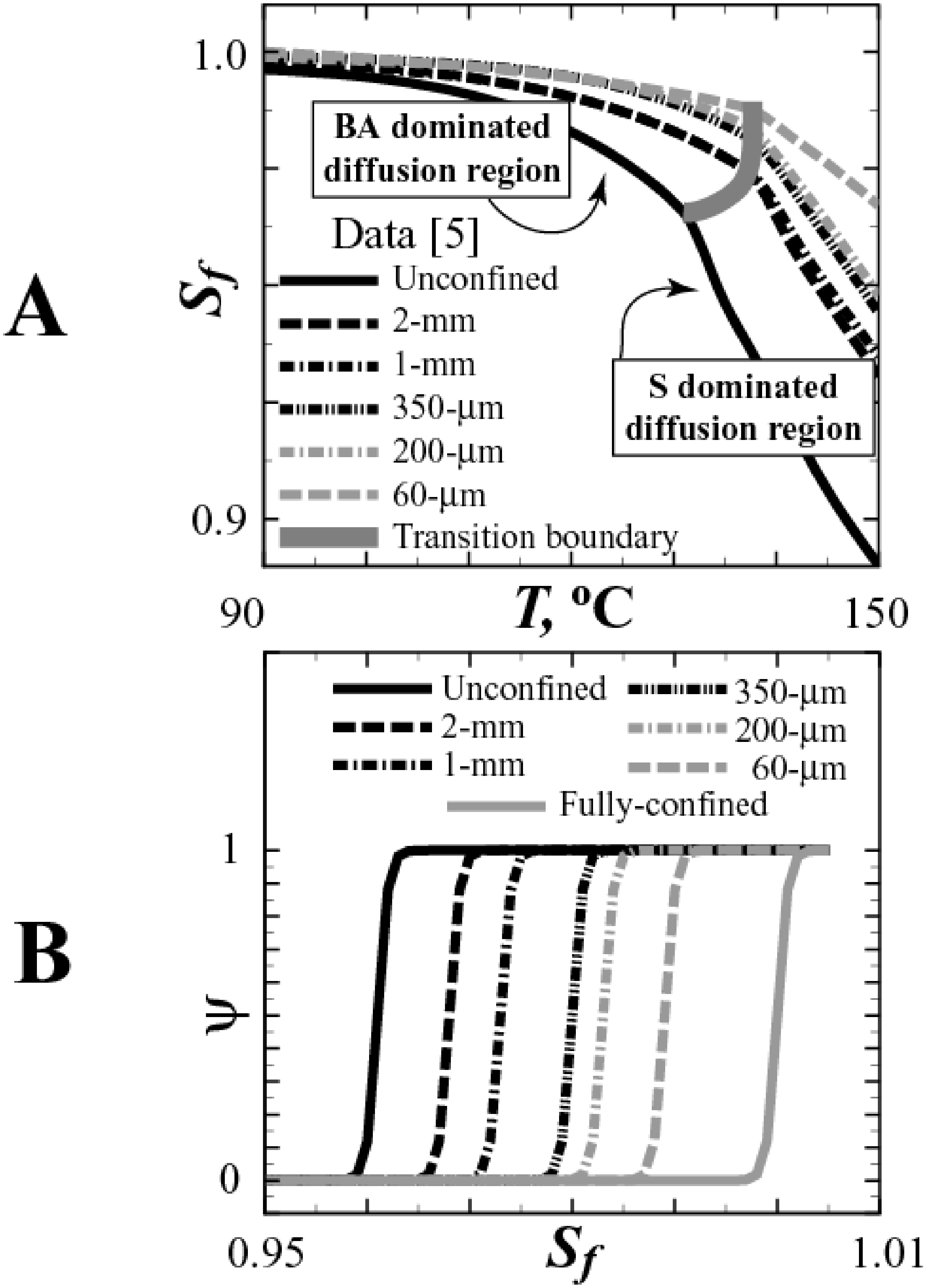

Fig. 6. A) Measured [5] mass loss for TGA samples ramped at 20ºC/min in partially-confined sample pans with orifice diameters indicated in the legend. Unconfined data was taken using an open pan. B) Weighting function used in eqn (36).

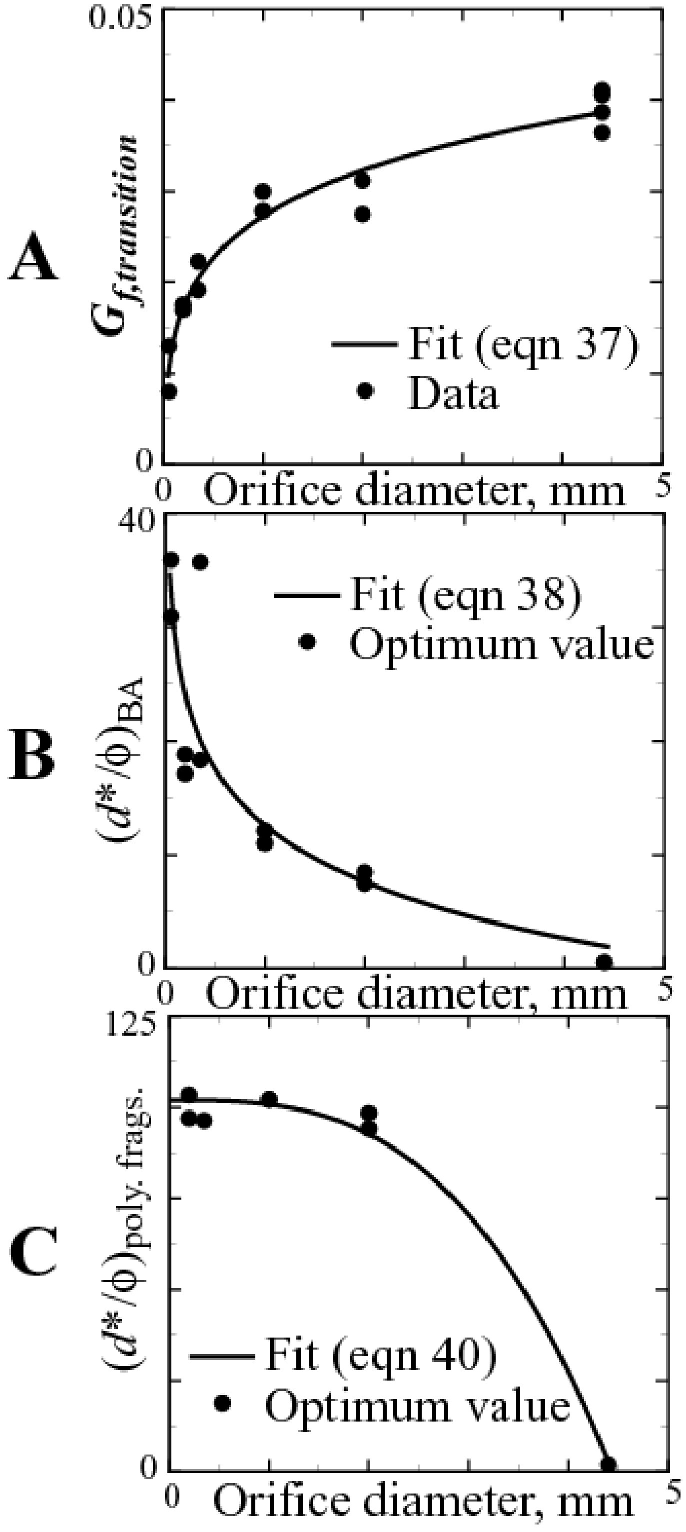

Fig. 7. A) Transitional gas fraction, B) $(d^*/\phi)_{BA}$, and C) $(d^*/\phi)_{polymer\ fragments}$.

function of the orifice diameter. The solid line in Fig. 7.A is represented by the following empirical equation:

$$G_{f,transition} = \begin{cases} 0.039 & Unconfined \\ 0.0215 \times d_{orifice}^{0.131} - 0.0259 & Partially\,confined \\ 0.00 & Fully\,confined \end{cases} , \tag{37}$$

where the orifice diameter, $d_{orifice}$, is in μm. The weighting function, plotted in Fig. 6.B for various levels of confinement, provides a smooth transition between the d^*/ϕ for the blowing agent and surfactant.

For partially-confined decomposition; the empirical values of d^*/ϕ for the blowing agent are:

$$\left(d^*/\phi\right)_{BA}^{partially\text{-}confined} = 62.1 - 7.17\ln\left(d_{orifice}\right), \tag{38}$$

with the limits $0.542 \le \left(d^*/\phi\right)_{BA}^{partially\text{-}confined} \le 36.0$. The orifice diameter, $d_{orifice}$, in eqn (38) is in μm. The empirical fit in eqn (38) was chosen to give good agreement to the partially-confined TGA data. The best estimates for $(d^*/\phi)_{BA}$ are also given in Fig. 7.B. The d^*/ϕ for the surfactant was assumed to be the same as the unconfined decomposition:

$$\left(d^*/\phi\right)_{S}^{partially\text{-}confined} = 2, \tag{39}$$

and the d^*/ϕ for the polymer fragments were assumed to be

$$\left(d^*/\phi\right)_{L_1}^{partially\text{-}confined} = \left(d^*/\phi\right)_{L_2}^{partially\text{-}confined} = \left(d^*/\phi\right)_{L_3}^{partially\text{-}confined} = 102 - 1.17\times10^{-9}\, d_{orifice}^{3}, \tag{40}$$

with the limits $2 \le \left(d^*/\phi\right)_{L}^{partially\text{-}confined} \le 102$. Figure 7.C shows the best estimates of d^*/ϕ for the polymer fragments. The orifice diameter, $d_{orifice}$, in eqn (40) is in μm. The superscript, *partially-confined*, refers to decomposition where the reacted products are constrained by an orifice.

The d^*/ϕ values for the fully-confined systems were obtained using the partially-confined d^*/ϕ equations evaluated at the limit as the orifice diameter approached zero. This limit becomes:

$$\left(d^*/\phi\right)_{BA}^{fully\text{-}confined} = 36 \tag{41}$$

$$\left(d^*/\phi\right)_{S}^{fully\text{-}confined} = 2 \tag{42}$$

$$\left(d^{*}/\phi\right)_{L_1}^{fully\text{-}confined}=\left(d^{*}/\phi\right)_{L_2}^{fully\text{-}confined}=\left(d^{*}/\phi\right)_{L_3}^{fully\text{-}confined}=102 \tag{43}$$

The superscript, *fully-confined*, refers to decomposition where the reacted products do not leave the system.

The method of choosing d^{*}/ϕ for the SREF model is based on empirical correlation using TGA data. The values of d^{*}/ϕ are constant throughout the SREF calculations. The constants in the SREF model are set without regard to the evolution of diffusion lengths or developing tortuosity. The SREF d^{*}/ϕ models discussed in this section should only be used for experiments similar to the TGA experiments where the decomposing gases are in intimate contact with the degrading foam. The decomposing gases should also be in the neighborhood of the decomposing foam. The hot-cell experiment, discussed in Section 9, satisfies this "local" requirement and will be used to evaluate the fully-confined values of d^{*}/ϕ. If the decomposition products cannot be kept in intimate "local" contact with the decomposing foam, even though the system may be sealed, the constant values of d^{*}/ϕ for "unconfined systems" represented by eqns (32) to (34) are recommended. The large-scale radiant heat experiments discussed in Ref. (5) do not satisfy this "local" restriction and constant values of d^{*}/ϕ using eqns (32) to (34) are recommended. Further research regarding confinement in large-scale systems is also recommended.

5. Lattice Statistics

Hobbs et al. [6-7] have used percolation theory to describe thermal decomposition of polymeric foams by relating a postulated chemical structure to a Bethe lattice network composed of sites connected by bridges. Bethe lattices are "tree-like" structures with sites continually branching to other sites without any branch reconnecting to a parent site. The algebraic lattice statistics for these "idealized" networks can be solved efficiently for three-dimensional geometries. The REF polymer lattice was approximated with Bethe lattices to determine the distribution of various polymer fragments. A polymer fragment containing *n*-sites is referred to as an *n*-mer. Polymer fragments containing 1, 2, 3, or an infinite number of sites are referred to as a monomer (or 1-mer), a dimer (or 2-mer), a trimer (or 3-mer), and an infinite-mer (or ∞-mer), respectively.

The population variable determined from the kinetic mechanism can be used to determine the fraction of sites that are connected by bridges. For example, the fraction of intact bridges, *p*, can be determined as follows:

$$p = (L_1 + L_2 + L_3)/(1 - S^o)\,, \tag{44}$$

where L_1, L_2, and L_3 are the different bridge types calculated with the kinetic mechanism and the factor $(1 - S^o)$ puts the bridge population, *p*, on a polymer basis. The mass fraction of finite polymer fragments produced from the thermally degrading foam depends on the population of intact bridges, *p*, determined from the kinetic mechanism and the coordination number, $\sigma+1$, which represents the number of possible bridges that can radiate from a site. As the number of broken bridges increases, the fraction of sites belonging to finite polymer fragments increases relative to the fraction of sites belonging to the infinite network. Since *p* is the probability that a bridge is intact and σ bridges radiate from the adjoining site, an infinite cluster exists only when $\sigma p_c > 1$ or $p_c > 1/\sigma$. The infinite network no longer exists when the bridge population is less than p_c.

For Bethe lattices, the number of finite polymer fragments can be determined from the coordination number and the bridge population, p. The probability, F_n, that any given site is a given member of a finite polymer fragment of n sites with s bridges is

$$F_n = a_n p^s (1-p)^\tau \tag{45}$$

where

$$s = n - 1 \tag{46}$$

and

$$\tau = n(\sigma - 1) + 2 \tag{47}$$

τ is the number of broken bridges on the perimeter of the polymer fragment with s-bridges connecting n-sites. Equation (45) formally states that the probability that any given bridge belongs to an n-mer is the probability that the given bridge is occupied (p^s) multiplied by the probability that the nearest neighbor bridges are unoccupied $(1\text{-}p)^\tau$ with a_n accounting for the distinct number of configurations possible for the n-mer. a_n is also used to convert the probability from a bridge basis to a site basis.

The number of different ways to form an n-mer is represented by a_n [17]:

$$a_n = \frac{\sigma+1}{\tau+s}\binom{\tau+s}{n-1}. \tag{48}$$

The binomial expression in eqn (48) represents the number of distinct n-mer configurations that can be obtained from $\tau + s$ potential bridges. The factor $\frac{\sigma+1}{\tau+s}$ converts F_n from a bridge probability to a site probability. a_n can also be written in terms of gamma functions for use with non-integer values of the coordination number:

$$a_n = \left(\frac{\sigma+1}{\tau+s}\right)\frac{\Gamma(n\sigma+2)}{\Gamma(n)\Gamma\left[\tau+1\right]}. \tag{49}$$

For chain statistics with a coordination number of two ($\sigma + 1 = 2$), a_n is equal to n.

The mass fraction and molecular weight of polymer fragments can be determined by relating the total mass and mass associated with the finite polymer fragments on a site basis. Up to this point, a site has been loosely defined in Section 2 as a point from which a lattice or network can be propagated by connecting to other sites. Figure 2 presented six potential sites and gave an average coordination number for the REF polymer as three. A more detailed description of sites in the REF polymer will be given in this section.

Figure 8.A shows the most common chemical structural unit for the REF polymer with the pentaerythritol triacrylate (PETA) site highlighted. A detailed schematic of the "extended PETA site" is shown in Fig. 8.B. A simpler "extended PETA site", used in the SREF lattice statistics model, is shown in Fig. 8.C. The "PETA site" is enclosed in a circle in Fig. 8.A and 8.B. The detailed extended site, shown in Fig. 8.B, is enclosed in a black square. Atoms associated with bridges that connect sites are shown in gray in Fig. 8.B. The "extended site" in Fig. 8.B includes the atoms associated with the "site" as well as atoms associated with the bridges. Having atoms associated with both the site and the bridges complicates the lattice statistics considerably. The lattice used in the SREF model assumes that there is no mass associated with the sites and that all of the polymer mass is located in bridges. The extended site for the SREF model contains mass associated only with bridges.

Figure 8.C shows the simplified lattice structure used in the SREF model. The coordination number, (σ + 1), was chosen based on the average coordination number of sites in the structural unit as discussed previously in Section 2. The "extended site" used in the SREF model is shown in Fig. 8.C enclosed in the black square. The mass of the SREF extended site, m_t, is based on the average molecular weight of the bridges connecting the sites, $\bar{M}_b$:

$$m_t = \tfrac{\sigma+1}{2}\bar{M}_b \tag{50}$$

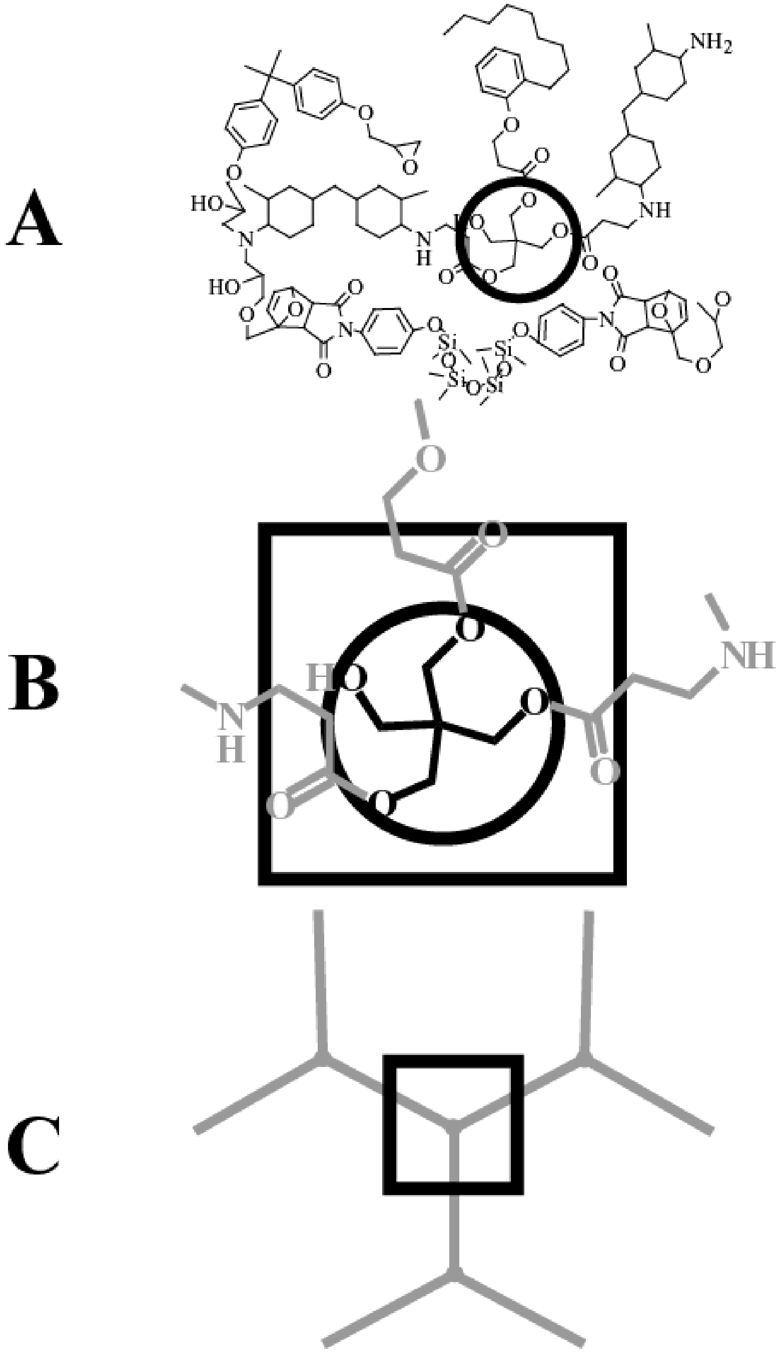

Fig. 8. A) Most common chemical structural unit with the pentaerythritol triacrylate (PETA) site highlighted, B) detailed “extended site” in black square, and C) simple “extended site” in black square used in the SREF model. In part B, the "site" contains atoms that are colored black. The atoms associated with the bridges connecting other sites are colored gray. The "extended site" includes the black site atoms and half of the gray bridge atoms connecting neighboring sites. In part C, there are no atoms associated with the "site." The "extended site " in part C is only composed of bridge atoms.

For the SREF model, the coordination number is 3 and m_t is equal to $\frac{3}{2}\bar{M}_b$. The factor $\frac{3}{2}$ represents three of the half bridges enclosed within the black square in Fig. 8.C. The average molecular weight of the bridges connecting the sites, $\bar{M}_b$, can be obtained from the initial bridge populations.

The average molecular weight of the bridges; L_1, L_2, and L_3; can be determined from the initial mass fractions, ω_L^o, and molecular weights, M_L, of these bridges as follows (see eqn M, p 534 in ref. 16):

$$\bar{M}_b = \frac{1}{\dfrac{\omega_{L_1}^o}{M_{L_1}} + \dfrac{\omega_{L_2}^o}{M_{L_2}} + \dfrac{\omega_{L_3}^o}{M_{L_3}}}, \tag{51}$$

where the mass fractions; $\omega_{L_1}^o$, $\omega_{L_2}^o$, and $\omega_{L_3}^o$ are determined from the initial bridge populations as:

$$\omega_{L_1}^o = \frac{L_1^o}{L_1^o + L_2^o + L_3^o} \tag{52}$$

$$\omega_{L_2}^o = \frac{L_2^o}{L_1^o + L_2^o + L_3^o} \tag{53}$$

$$\omega_{L_3}^o = \frac{L_3^o}{L_1^o + L_2^o + L_3^o}. \tag{54}$$

The initial bridge populations; L_1^o, L_2^o, and L_3^o; were given in Table 3 for REF100, REF200, and REF300. The molecular weights of the three bridges; M_{L_1}, M_{L_2}, and M_{L_3}; were given in Table 4 as 296, 140 and 228 g/mol, respectively. The composition of L_1 and L_3 are the same as for octamethylcyclotetrasiloxane, $((CH_3)_2SiO)_4$, and bisphenol A, $[(C_6H_4)OH]_2C(CH_3)_2$, respectively. The composition of the L_2 is the same as the mixed products, $C_{7.44}H_{12.5}N_{0.65}O_{1.74}$, with a molecular weight of 140 g/mol. The L_2 composition was determined by using the elemental composition of the REF polymer listed Table 2 and assuming the C-residue in Table 3 was carbon and f_{OS} is zero for unconfined decomposition.

A monomer contains a single site. Likewise, a dimer contains two sites and a trimer contains three sites. In the SREF lattice model, bridges are either occupied or unoccupied and danglers are not allowed. The term "dangler" was used in previous polyurethane decomposition lattice models [6,7] to represent a "broken" bridge that was attached to a site. "Danglers" were used in reversible reactions where a dangler could be reattached to the polymer structure. To simplify the lattice statistics, reverse reactions and danglers are not used in the SREF lattice statistics model. Since an SREF site contains no mass and danglers are not allowed, a monomer does not contain mass. On the other hand, a dimer contains two sites connected by a single bridge. Thus the molecular weight of a dimer is the same as the molecular weight of a single bridge, $\bar{M}_b$. Likewise, the molecular weight of an n-mer, M_n, can be determined from the average bridge molecular weight as follows:

$$M_n = (n-1)\bar{M}_b \,. \tag{55}$$

The mass fractions of the *BAS*, *OS*, *MP*, and *BPA* species; ω_{BAS}, ω_{OS}, ω_{MP}, and ω_{BPA}; can be determined directly from the population variables calculated using eqns (1)-(4) since *BAS*, *OS*, *MP*, and *BPA* are mass-based progress variables. Mass based progress variables track the reaction in terms of mass fractions. The mass fractions of *BAS*, *OS*, *MP*, and *BPA* are:

$$\omega_{BAS} = BAS \tag{56}$$

$$\omega_{OS} = OS \tag{57}$$

$$\omega_{MP} = MP \tag{58}$$

$$\omega_{BPA} = BPA \,. \tag{59}$$

The mass fractions of the polymer fragments, $\omega_{n\text{-}mer}$, can be calculated using the mass of an extended site, m_t, given previously in eqn (50) and mass of the *n-mer* expressed on an extended site basis, m_n, as:

$$\omega_{n\text{-}mer} = \frac{m_n}{m_t}\left(1 - S^o\right). \tag{60}$$

The factor $\left(1 - S^o\right)$ puts the mass fraction on a foam basis rather than a polymer basis. The mass of the finite polymer fragments expressed on an extended site basis, m_n, can be determined from:

$$m_n = M_n Q_n \,, \tag{61}$$

where M_n is the molecular weight of the n-mer given previously in eqn (55). Q_n is the number density of n-site fragments on a per site basis [17]:

$$Q_n = F_n / n = \left[a_n p^s (1-p)^\tau \right] / n \,. \tag{62}$$

The primary variables of interest for the SREF lattice statistics model are the mass fractions of *BAS*, *OS*, *MP*, *BPA*, and the *n*-mer species; which can be calculated using eqns (56)-(60). Molecular weights of theses species are also necessary for the vapor-liquid-equilibrium model discussed in the next section. The molecular weights for the *BAS*, *OS*, *MP*, and *BPA* species were given in Table 4 and the molecular weight of the *n*-mer species is given by eqn (55). The SREF model formally considers 11 species – 1) BAS, 2) OS, 3) MP, 4) BPA, 5) 2-mers, 6) 3-mers, 7) 4-mers, 8) nonvolatile carbon residue, 9) nonvolatile OS residue, 10) L-mers, and 11) XL-mers. The L-mer population represents the *n*-mer ranging from the 5-mer populations up to a user defined *max*-mer population. The *max*-mer should be less than 500 to prevent computer overflow errors, although a value of 10 gives essentially the same results as 500 and was used for the calculations in the current report. The mass fraction and molecular weight of the *L*-mer population are calculated as follows:

$$\omega_{L\text{-mer}} = \sum_{n=5}^{\text{nmax}} \frac{m_n}{m_t}\left(1 - S^o\right) \tag{63}$$

$$M_{L\text{-mer}} = \frac{1}{\displaystyle\sum_{n=5}^{\text{nmax}} \frac{m_n\left(1-S^o\right)}{m_t (n-1)\bar{M}_b}} = \frac{1}{\displaystyle\sum_{n=5}^{\text{nmax}} \frac{2Q_n\left(1-S^o\right)}{\left(\sigma+1\right)\bar{M}_b}} \tag{64}$$

The XL-mer population represents the *n*-mers that range from the *max*-mer population to the ∞-mer populations. The mass fractions of the XL-mer populations were determined using continuity constraints:

$$\omega_{XL\text{-mer}} = 1 - \omega_{BAS} - \omega_{OS} - \omega_{MP} - \omega_{BPA} - \left(\sum_{n=2}^{\text{nmax}} \omega_{n\text{-mer}} \right) - \omega_{C\text{-}residue} - \omega_{OS\text{-}residue} \,. \tag{65}$$

The user defines the molecular weight of the XL-mer population, which was specified to be 4,000 g/mol in the current report. The mass fractions of the residues were given in Table 3 and are functions of pressure and the degree that the decomposition gases are confined. The user defines the molecular weight of the C-residue and OS-residue, which were both specified to be 1,000 g/mol in the current report.

6. Vapor-Liquid-Equilibrium

The previous section provided a method to calculate the mass fractions of 11 species considered in the SREF decomposition chemistry model. Seven of these species – 1) BAS, 2) OS, 3) MP, 4) BPA, 5) 2-mers, 6) 3-mers, 7) 4-mers – are referred to as "VLE-species" since vapor-liquid equilibrium is used to determine whether or not these species reside in the condensed-phase, the gas-phase, or in both phases. The remaining four species – 8) nonvolatile carbon residue, 9) nonvolatile OS residue, 10) L-mers, and 11) XL-mers – are referred to as "non-VLE-species" since they have extremely large molecular weights and are assumed to remain in the condensed-phase. Figure 9 shows an instance where the VLE-species and non-VLE species are partitioned using a pie chart. In Fig. 9, the mass fraction of the non-VLE species (Z_{NV}) is equal to the mass fraction of the VLE species (Z_{NV}). Figure 9 shows an instance where the mass fraction of the VLE-condensed-phase species ($S_{f,VLE}$) is equal to the mass fraction of the VLE-gas-phase species ($1-S_{f,VLE}$).

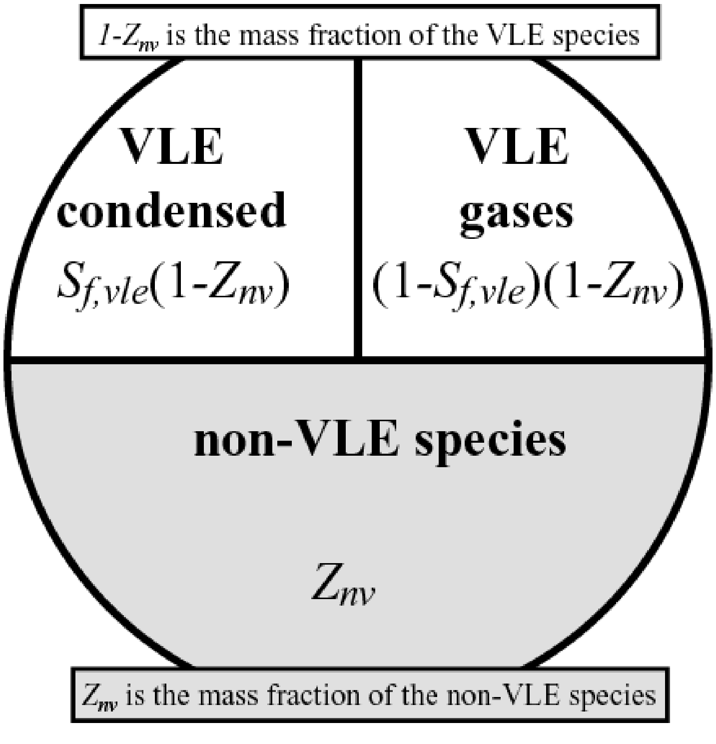

Fig. 9. Pie chart showing the relationship between the VLE species and the non-VLE species. Only the VLE species are considered in the VLE calculation that determines the mass fraction of the condensed VLE species, $S_{f,vle}$.

Section 5 outlined the method used by the SREF model to determine the 11 mass fractions, which sum to unity, without regard to whether or not the species are VLE-species or non-VLE-species. In this section, equations will be derived to determine the mole fractions for the VLE-species. The VLE-species mole fractions are used with an isothermal flash calculation (VLE calculation) to determine which VLE-species are in the condensed-phase and which VLE-species are in the gas-phase. Following, the flash calculation, the VLE species will be recombined with the non-VLE-species to determine the overall condensed and gas-phase compositions. The molecular weight of the condensed and gas-phase, the viscosity of the evolving foam, the hydrodynamic pressure rise in fully confined systems, etc. can be determined with the composition in both phases determined.

The mass fractions for the 7 VLE-species determined with eqns (56) to (60) do not sum to unity since these mass fractions are based on all 11 species summing to unity. In order to calculate the vapor-liquid split for the VLE-species, the mass fractions were determined for the VLE-species as follows:

$$\omega_i^{vle} = \frac{\omega_i}{\sum_{i=1}^{7} \omega_i}, \tag{66}$$

where ω_i^{vle} represents the mass fraction of the i^{th} VLE-species when only VLE-species are considered. ω_i represents the mass fraction of the i^{th} VLE-species when all 11 SREF species are considered. The VLE-species mole fractions, z_i, can be determined from the ω_i^{vle} mass fractions as follows (see eqn N, p 534 in ref. 16):

$$z_i = \frac{\omega_i^{vle} / M_i}{\sum_{j=1}^{7} \left(\omega_j^{vle} / M_j \right)}, \tag{67}$$

where the i and j represent the i^{th} and j^{th} VLE species, respectively. For the VLE species, a z is used for the mole fraction of the combined-phase products; an x is used for the mole fraction of the condensed-phase VLE products; and a y is used for the mole fraction of the gas-phase VLE products.

A standard *multicomponent isothermal flash calculation* based on the Rachford-Rice equation is used to determine the split between vapor and liquid *V/F* [18]:

$$f\left\{\frac{V}{F}\right\}=\sum_{i=1}^{z}\frac{z_i(K_i-1)}{(K_i-1)\frac{V}{F}+1}=0\ , \tag{68}$$

where *K*, *V*, and *F* are the vapor-liquid equilibrium ratio or *K-value*, total moles in the vapor-phase, and total moles in the combined-phase, respectively. The nomenclature for the combined-phase is an "*F*" since the combined-phase is commonly referred to as the "feed." Equation (68) can be solved by trial-and error by guessing values of *V/*F between 0 and 1 until $f\left\{\frac{V}{F}\right\}=0$. In the SREF model, the ratio *V/F* in eqn (68) was determined iteratively using the *zeroin* solver [19]. Once *V/F* is known, the condensed fraction of the VLE species, $S_{f,vle}$, can be determined. $S_{f,vle}$ is defined as the mass of the condensed VLE species divided by the total mass of the VLE species.

The VLE mixture is a subcooled liquid (*V/F* = 0, $S_{f,vle}$ = 1, $x_i = z_i$) when $f\left\{\frac{V}{F}=1\right\}>0$ and $f\left\{\frac{V}{F}=0\right\}>0$. The mixture is a super heated vapor (*V/F* =1, $S_{f,vle}$ = 0, $y_i = z_i$) when $f\left\{\frac{V}{F}=1\right\}<0$ and $f\left\{\frac{V}{F}=0\right\}<0$. Otherwise the value of *V/F* is between zero and one and the mixture is multiphase. For multiphase mixtures, the composition of the VLE liquid (x_i) and VLE vapor (y_i) phases can be determined as follows:

$$x_i=\frac{z_i}{\left(K_i-1\right)\frac{V}{F}+1} \tag{69}$$

$$y_i=K_ix_i \tag{70}$$

where x_i, y_i, and z_i represents the mole fractions of the condensed-phase, gas-phase, and combined-phase of the VLE species, respectively.

The average molecular weight of the condensed-phase VLE species, $M_{vle}^{condensed}$, and gas-phase VLE species can be determined from the following equations:

$$M_{vle}^{condensed} = \sum_{i=1}^{7} x_i M_i \tag{71}$$

$$M_{vle}^{gas} = \sum_{i=1}^{7} y_i M_i \tag{72}$$

The $S_{f,vle}$, can be determined by assuming a basis of 1 mole of VLE feed, $F = 1$, so that the V/F ratio determined by solving eqn (68) is equal to V:

$$V = \frac{V}{F} \,. \tag{73}$$

The moles of L can then be determined since F (assumed to be unity) is equal to the sum of the vapor moles (V) and the liquid moles (L):

$$L = 1 - V \,. \tag{74}$$

The VLE solid fraction, $S_{f,vle}$, can be determined using V and L from eqns (73) and (74):

$$S_{f,vle} = \frac{\sum_{i=1}^{7} x_i L M_i}{\sum_{i=1}^{7} x_i L M_i + \sum_{i=1}^{7} y_i V M_i} \,. \tag{75}$$

6.1 Foam Composition

Foam response depends on the solid fraction of the foam, S_f, defined as the mass normalized by the initial mass, which can be determined from the VLE solid fraction as follows:

$$S_f = Z_{nv} + S_{f,vle}(1 - Z_{nv}) \,, \tag{76}$$

where Z_{nv} is the mass fraction of the non-VLE species shown in the pi chart in Fig. 9. The second term in eqn (76), $S_{f,vle}(1 - Z_{nv})$, represents the mass fraction of the VLE condensed-phase species, as shown in Fig. 9. Z_{nv} can be determined from the following equation:

$$Z_{nv} = \omega_{L\text{-}mer} + \omega_{XL\text{-}mer} + \omega_{C\text{-}residue} + \omega_{OS\text{-}residue} \,, \tag{77}$$

where the mass fractions of the nonvolatile species are represented by $\omega_{L\text{-}mer}$, $\omega_{XL\text{-}mer}$, $\omega_{C\text{-}residue}$, and $\omega_{OS\text{-}residue}$. The *L-mer* and *XL-mer* mass fractions, $\omega_{L\text{-}mer}$ and $\omega_{XL\text{-}mer}$, can be determined using eqns (63) and (65). The ultimate residue mass fractions, $\omega_{C\text{-}residue}$ and $\omega_{OS\text{-}residue}$, can be determined using Table 3.

The mass fractions of species in the foam were represented in Section 5 by ω_i with $\sum_{i=1}^{11} \omega_i = 1$. ω_i's do not differentiate whether or not a species exists in the gas-phase or condensed-phase. Two additional mass fractions, m_i^c and m_i^g, will be used to differentiate between the condensed-phase composition and gas-phase composition, with $\sum_{i=1}^{11} m_i^c = 1$ and $\sum_{i=1}^{7} m_i^g = 1$. The four nonvolatile species reside only in the condensed-phase making the number of possible species in the condensed-phase and gas-phase, 11 and 7, respectively. The composition of the gas-phase portion of the foam, composed of the VLE-species, is:

$$m_i^g = \frac{y_i M_i}{\sum_{j=1}^{7} y_j M_j}. \tag{78}$$

The mass fraction of the nonvolatile species in the condensed-phase portion of the foam is the same as the mass fraction in the foam since the nonvolatile species only reside in the condensed-phase:

$$m_{C\text{-}residue}^c = \omega_{C\text{-}residue} \tag{79}$$

$$m_{OS\text{-}residue}^c = \omega_{OS\text{-}residue} \tag{80}$$

$$m_{L\text{-}mer}^c = \omega_{L\text{-}mer} \tag{81}$$

$$m_{XL\text{-}mer}^c = \omega_{XL\text{-}mer} \tag{82}$$

The portion of the VLE-species that reside in the condensed-phase portion of the foam is

$$m_i^c = \frac{x_i M_i}{\sum_{j=1}^{7} x_j M_j} \times S_{f,vle}\left(1 - Z_{nv}\right), \tag{83}$$

where i represents the seven VLE-species. The first term on the right-hand-side (rhs) of eqn (83), $x_i M_i \Big/ \sum_{j=1}^{7} x_j M_j$, represents the condensed-phase mass fractions of the VLE-species. The second term on the rhs of eqn (83), $S_{f,vle}\left(1-Z_{nv}\right)$, represents the mass fraction of the condensed-VLE in the foam as depicted in Fig. 9. The condensed-phase molecular weight (M_c) is then

$$M_c = \left(\sum_{i=1}^{11} \frac{m_i^c}{M_i} \right)^{-1}, \tag{84}$$

where m_i^c represents all of the SREF species mass fractions given in eqns (79)-(83).

6.2 Activity Coefficients

The vapor-liquid equilibrium ratio, or *K-value*, is defined as:

$$K_i = \frac{y_i}{x_i} = \frac{\gamma_i P_i^*}{P}, \tag{85}$$

where x_i, y_i γ_i, P_i^*, and P represent mole fractions in the condensed-phase, mole fraction in the vapor-phase, activity coefficients, pure component vapor pressures at the system temperature, and thermodynamic pressure, respectively. Activity coefficients represent deviations from ideality.

The activity coefficients were chosen to limit the influence of pressure above critical conditions using the following equation:

$$\gamma_i = \begin{cases} \gamma_i^o & \text{if } P \le P_{c,i} \\ \gamma_i^o \dfrac{P}{P_{c,i}} & \text{if } P > P_{c,i} \end{cases} \tag{86}$$

where γ_i^o, P, and $P_{c,i}$ represent the activity coefficient of the i^{th} species at ambient conditions, the thermodynamic pressure, and the critical pressure of the *ith* species, respectively. The effect of the SREF activity coefficient model is to prevent the *K-value* from approaching zero as the thermodynamic pressure exceeds the critical pressure. Table 5 gives the values of γ_i^o and $P_{i,c}$ used for each of the VLE species. The data from which the vapor pressures were obtained are only good to about 400ºC. Above 400ºC, the extrapolations are well behaved.

A potential problem with use of the activity coefficient eqn (86) is that the properties of the individual components do not adequately represent the mixture critical pressure. On method to alleviate this problem is to use a mixture critical pressure with an applicable mixture rule. A mixture critical pressure should be considered for future development of the decomposition chemistry model.

Table 5. Parameters used in eqn (86)

VLE-Species	γ_i^{o} (estimated)	$P_{i,c}$ [1]
BAS	30	5.0[2]
OS	0.5	13.1 [22]
MP	3	52[3] [22]
BPA	0.5	28.9 [22]
2-mer	0.5	38.7[2]
3-mer	0.5	38.7[2]
4-mer	0.5	38.7[2]

[1] Critical pressures in atmospheres.

[2] Estimated.

[3] Average of o-, m-, p-cresol, phenol, and furan [22].

6.3 Vapor Pressures

The vapor pressure of the BAS species was assumed to be a weighted average of the vapor pressures for the blowing agent (BA) and the surfactant:

$$P^*_{BAS} = 0.735P^*_{BA} + 0.265P^*_S, \tag{87}$$

where

$$P^*_{BA} = 52892 \times 10^{(-1562/T)} \tag{88}$$

and

$$P^*_S = 40500 \times 10^{(-1946/T)}. \tag{89}$$

In eqns (87) and (88), T is the system temperature in Kelvin and P^* is the vapor pressure in atmospheres. The vapor pressure correlation for the blowing agent in eqn (88) was obtained from the physical properties data sheets obtained for FC-72 [20]. The vapor pressure correlation for the surfactant in eqn (89) was obtained by fitting three vapor pressure points obtained for DC-193 (REF surfactant)– 1) 5-mm Hg at 21ºC, 2) 25-mm Hg at 54.4ºC and 760-mm at 148.9ºC (boiling point) [21].

The specific composition of the surfactant is unknown and only the general composition was available – 9% polyethylene glycol, 71% silicone, and 20% ethylene oxide polymer by mass. Since the composition of the surfactant is a trade secret, a mole fraction weighted vapor pressure for the BAS species was not available. However a mass fraction weighted vapor pressure should give reasonable vapor pressures for the BAS components, which is given in eqn (87). Recall that the blowing agent and surfactant account for 19.2% of the foam by mass, with 14.12% blowing agent and 5.08% surfactant.

The following vapor pressure correlation was used for the OS, MP, and BPA species:

$$P_i^* = 9.87\times10^{-6}\exp\left(A+\frac{B}{T}+C\ln T+DT^E\right), \tag{90}$$

where the units of P_i^* and T are in atmospheres and degrees Kelvin, respectively. The coefficients in eqn (90) are given in Table 6. The coefficients in Table 6 for OS were obtained by fitting a similar correlation in ref [22] from 17-312ºC. The coefficients for OS were not taken from [22] since the extrapolation for temperatures greater than 400ºC diverged significantly from expected vapor pressures. The OS vapor pressures predicted with the coefficients given Table 6 are well behaved for temperatures up to 1000ºC. The vapor pressure for the mixed-product species, MP, was assumed to be the same as phenol with the coefficients obtained from [22]. The coefficients for the BPA species were also obtained from [22].

Table 6. Vapor pressure coefficient used in eqn (90)

Species	A	B	C	D	E
OS[1]	19.37	0	0	-75000.0	-1.5
MP[2]	59.08	-8050	-4.899	2.8×10^{-4}	1
BPA[3]	401.21	-33771	-54.854	2.7596×10^{-2}	1

[1] Octamethylcyclotetrasiloxane coefficients fit using data in [22] from 17-312ºC. Coefficients were refit to obtain better extrapolations.

[2] Mixed product coefficients assumed to be same as phenol from [22].

[3] Bisphenol A coefficients from [22].

The vapor pressures for the 2-mer, 3-mer, and 4-mer VLE-species were calculated from the following correlation proposed by Fletcher et al. [23] for organic molecules:

$$P_n^* = 87100\exp\left(\frac{-299M_n^{0.59}}{T}\right), \tag{91}$$

where P_n^* is the vapor pressure of the pure n^{th}-polymer fragment in atmospheres, M_n is the molecular weight of the n^{th}-polymer fragment in g/mol as determined from eqn (55), and T is the temperature in K. The functional form of eqn (91) is similar to the Clausius-Clapeyron equation. The coefficients in eqn (91) were obtained from coal tars with molecular weights ranging from 110-315 g/mol. The vapor pressure predicted with eqn (91) increases with lower molecular weight species.

7. SREF Model Parameters

The SREF model includes a kinetic mechanism described in Section 3, a mass transport model described in Section 4, a lattice statistics model described in Section 5, and a vapor-liquid equilibrium model described in Section 6. Each of these various sections provided most of the input parameters required for the SREF model. The only SREF parameters that were not discussed in detail in Sections 3-6 are the reaction rate parameters for the four reaction steps. This section will present how the reaction rate parameters were obtained as well as provide a summary of the remaining SREF model parameters. The uncertainty in some of the SREF model parameters will also be presented.

Tables 7, 8, and 9 give the SREF model parameters; Table 7 gives the kinetic parameters; Table 8 gives the parameters for the lattice statistics model; and Table 9 gives parameters for the VLE, mass transport, and some physical properties of the REF encapsulant. There are approximately 54 parameters for the SREF model – 12 chemical kinetic parameters, 14 lattice statistics parameters, and 28 miscellaneous parameters. In Tables 7-9, ξ, μ, and σ represent the model parameters, mean value of the model parameters, and uncertainty in the model parameters, respectively. Uncertainty in the response due to lattice statistics uncertainty was negligible as shown in [24]. The uncertainties in the remaining parameters were used to investigate model sensitivity to these various input parameters.

Three types of chemistry parameters are listed in Table 7 – the pre-exponential factors (A_i), the activation energies (E_i), and the standard deviation used with the distributed activation energy model (σ_E). The chemistry parameters for the desorption reaction (reaction 1) was obtained using an isothermal TGA experiment where the sample temperature was ramped quickly (20ºC/m) to 140ºC and held for few hours. The chemistry parameters for the remaining three polymer reactions were obtained from a single ramped TGA experiment where the sample temperature was ramped at 20ºC/m to about 575ºC.

Optimization techniques [25] were used to obtain the chemistry parameters in Table 7 by minimizing the absolute root mean squared (RMS) error between the calculated and measured mass loss for each of these experiments:

SREF Model Parameters

$$absolute\,RMS\,error = \sqrt{\sum_{i=1}^{n}\left(S_f^{TGA} - S_f^{SREF}\right)}\,. \tag{92}$$

The summation refers to the measured and calculated solid fraction at selected times during the TGA experiments. The solid fraction refers to the mass of the sample divided by the initial mass of the sample. Absolute error was used for the optimization routine rather than relative error since the solid fraction approaches a small number. Using relative error for the cost function would bias results near the end of the experiments.

The prefactors, A_i, were obtained using Clayton's [4] stability criterion for Arrhenius prefactors:

$$A_i = 10^{b_i}\exp\left(\frac{E_i}{RT_o}\right), \tag{93}$$

where b_i is used in the optimization procedure to maintain stability, since A_i is a function of the activation energy. A number of optimizations were performed with various TGA experiments with temperatures ramped at 20ºC/m to obtain chemistry uncertainty represented by σ_i in Table 7. The mean values of the chemistry parameters obtained from these runs could not be used for mean value analysis due to the high degree of correlation between the prefactors and activation energies. A single experiment was used to obtain the mean values of the activation energies (E_i), and the distributed activation energy model parameters (σ_E).

Table 7. Kinetic Parameters

ξ_i	μ_i	σ_i	Units
A_1	1×10^{13}	NA	1/s
A_2	2×10^{15}	NA	1/s
A_3	2×10^{16}	NA	1/s
A_4	6×10^{12}	NA	1/s
E_1	28.6	0.761	Kcal/mol
E_2	53.7	1.082	Kcal/mol
E_3	58.1	0.513	Kcal/mol
E_4	45.8	1.910	Kcal/mol
σ_{E1}	1.39	0.297	Kcal/mol
σ_{E2}	4.96	0.426	Kcal/mol
σ_{E3}	7.29	0.922	Kcal/mol
σ_{E4}	4.99	1.010	Kcal/mol

Table 8. Lattice Statistic Parameters

ξ_i	μ_i	Units
$\sigma+1$	3	NA
S_o	0.192	NA
L^o_1	0.104[1]	NA
L^o_2	0.563	NA
L^o_3	0.091	NA
OS-residue	0[1]	NA
M_{BAS}	120	g/mol
M_{OS}	296	g/mol
M_{MP}	140	g/mol
M_{BPA}	228	g/mol
$M_{C\text{-residue}}$	1000	g/mol
$M_{OS\text{-residue}}$	1000	g/mol
$M_{XL\text{-mer}}$	4000	g/mol
nmax	10	NA

[1] Value for unconfined decomposition only. See Table 3 for other conditions.

Table 9. VLE, mass transport, and various physical parameters

Species	ξ_i	μ_i	σ_i	Units[1]
BAS	Pc, Vc, γ	5, 2045, 30	0, 0, 3	atm, cc/mol, NA
OS	Pc, Vc, γ	13.1, 970, 0.5	0, 0, 0.05	atm, cc/mol, NA
MP	Pc, Vc, γ	52.0, 229, 3.0	0, 0, 0.3	atm, cc/mol, NA
BPA	Pc, Vc, γ	28.9, 677, 0.5	0, 0, 0.05	atm, cc/mol, NA
2-mer	Pc, Vc, γ	38.7, NA, 0.5	0, 0, 0.05	atm, cc/mol, NA
3-mer	Pc, Vc, γ	38.7, NA, 0.5	0, 0, 0.05	atm, cc/mol, NA
4-mer	Pc, Vc, γ	38.7, NA, 0.5	0, 0, 0.05	atm, cc/mol, NA
Surfactant	d/ϕ	2	1.3	NA
Blowing Agent	d/ϕ	0.542	0.035	NA
Polymer Fragments	d/ϕ	2	1.3	NA
Pressure	P	1	0.1	atm
Foam Density	ρ_{foam}	0.312	0.03	g/cc
Polymer Density	$\rho_{polymer}$	1.09	0.1	g/cc
Hot Cell Volume	$V_{element}$	0.638	0.06	cc

[1] "cc" and "NA" refer to cm^3 and "not applicable", respectively.

SREF Model Parameters

8. Auxiliary Models

The SREF model provides the necessary framework to incorporate a variety of models. The activity coefficient model presented in Section 6.2 is an example of such a model. Any uncertainty in the vapor pressure for unknown species such as the surfactant and the mixed-product gases are approximated with the activity coefficient model. More sophisticated activity coefficient models can be implemented into the SREF model framework if deemed necessary. The following sections provide simple models for pressurization and viscosity. The reaction enthalpy model, which has been calibrated using differential scanning calorimeter (DSC) data, is also presented.

8.1 Pressurization

Decomposition of the removable epoxy foam encapsulant is pressure dependent as shown by Clayton [4]. In the SREF model, the ultimate OS-residue given by eqn (7), the mass transport coefficients given by eqn (21), the K-values given by eqn (85), and the activity coefficients given by eqn (86) depend on pressure. Pressure can be regulated for well-controlled experiments. However, in practice pressure increases dynamically as the decomposition products accumulate in the control volume. The pressure within closed containers increases as the foam decomposes into gaseous products.

The pressurization model is based on the ideal gas equation with the initial pressure (P^o) and temperature (T^o) in an element specified:

$$P = P^o \left(\frac{V_g^o}{V_g} \right) \left(\frac{n}{n^o} \right) \left(\frac{T}{T^o} \right), \tag{94}$$

where P, P^o, V_g^o, V_g, n, n^o, T, and T^o are the dynamic pressure, initial pressure, initial gas volume, dynamic gas volume, dynamic gas moles, initial gas moles, dynamic element temperature, and initial element temperature, respectively. The dynamic variables are the variables that are not specified by the user or initialized. Dynamic variables include V_g, n, and T. The variables V_g and n depend on the solid fraction as calculated using the SREF model with eqn (76).

The condensed-phase mass in an element is:

$$m_p = S_f \rho_f^o V_e \,, \tag{95}$$

where m_p, S_f, ρ_f^o, and V_e represent the mass of the polymer in the element or computational cell, the solid fraction as defined by eqn (76), the initial bulk density of the foam, and the volume of the element or computational cell. The volume occupied by the condensed-phase mass in the element, V_p, can be determined using the density of the polymer, ρ_p^o:

$$V_p = \frac{m_p}{\rho_p^o} = \frac{S_f \rho_f^o V_e}{\rho_p^o} \,. \tag{96}$$

The volume of the gas-phase species in the element, V_g, can be determined by

$$V_g = V_e - V_p \,. \tag{97}$$

By combining eqns (96) and (97), the initial gas volume and dynamic gas volume can be determined

$$V_g^o = V_e \left[1 - \left(\frac{\rho_f^o}{\rho_p^o} \right) \right] \tag{98}$$

$$V_g = V_e \left[1 - S_f \left(\frac{\rho_f^o}{\rho_p^o} \right) \right] . \tag{99}$$

The initial gas volume can be determined from eqn (99) by setting the solid fraction equal to unity.

The initial gas moles in an element depend on the initial volume in the element given in eqn (98) as well as the initial temperature and pressure of the element:

$$n^o = P^o V_g^o \big/ R T^o \,, \tag{100}$$

where R is the ideal gas constant. The dynamic gas moles in an element depend on the mass of gas that evolves from the REF encapsulant as determined using the SREF chemistry model:

$$n = n^o + \frac{m_g}{M_{vle}^{gas}}, \tag{101}$$

where m_g represents the mass of gas evolved from the REF encapsulant due to reaction and M_{vle}^{gas} represents the molecular weight of the VLE gases as determined from eqn (72). The mass of the decomposition product gases is

$$m_g = \left(1 - S_f\right)\rho_f^o V_e. \tag{102}$$

Combining eqns (101) and (102) gives

$$n = n^o + \frac{\left(1 - S_f\right)\rho_f^o V_e}{M_{vle}^{gas}}. \tag{103}$$

The pressurization model is intimately coupled to the SREF chemistry model. The parameters in the pressurization model that are specified by the user include the initial pressure (P^o), temperature (T^o), bulk foam density (ρ_f^o), and REF polymer density (ρ_p^o), respectively. The parameters in the pressurization model that are initialized from the user specified parameters include the initial gas volume (V_g^o) and the initial gas-phase moles (n^o). The dynamic variables are the pressure (P), gas volume (V_g), gas moles (n) and the temperature (T).

8.2 Viscosity

Viscosity is not used in the SREF chemistry model, but would be important for future models that address flow of the decomposing polymer. Viscosity of the decomposition polymer would also be required for future bubble growth and coalescence models. A simple model for the viscosity of the decomposing REF encapsulant was postulated based on Flory's correlation [page 309 in ref 26] with molecular weight:

$$\log_{10}\eta = 0.0823\sqrt{M_c} - 0.712, \tag{104}$$

where M_c in g/mol is determined using eqn (84). The units on the viscosity, η, are in centipoises. Flory [26] states that the form of eqn (104) is remarkably accurate for a number of undiluted molten polymer melts composed of linear condensation polymers.

The coefficients in eqn (104) , 0.0823 and 0.712, were selected to give a viscosity of 10,000 centipoises when the foam temperature reaches about 300ºC (M_c = 3290 g/mol) and 100-centipoise when the foam temperature reaches about 500ºC. (M_c = 1090 g/mol). Although the coefficients in eqn (104) were arbitrarily chosen to give reasonable viscosities, the coefficients should be determined with viscosity data when available. The value 10,000 centipoises gives a viscosity, which is roughly 3½ times the viscosity of molasses at 25ºC. The value 100 centipoises is approximately the viscosity of the Ancamine 2049 curative (DMDC in Table 1) used to synthesis the removable epoxy foam. The removable epoxy foam polymer is composed of about 22% by mass Ancamine 2049.

8.3 Reaction Enthalpy

The reaction enthalpy is needed for multidimensional foam response models used to predict thermal transport within the foam. Data from a differential scanning calorimeter (DSC, ref 27) was used to determine the energy changes for conditions similar to the TGA experiment run at 20ºC/min shown previously in Fig. 3.B. The reaction energy is determined by measuring the energy required to heat a sample at a given rate and accounting for the energy required to heat the sample pan as well as the sensible enthalpy required to heat the sample. The reaction enthalpy is defined as:

$$q_{rxn} = q_{sen} - q_{DSC} \, , \tag{105}$$

where q_{rxn}, q_{sen}, and q_{DSC} represent the reaction enthalpy, the sensible enthalpy, and the heat flow to the sample in cal/s. The heat flow to the sample is determined by subtracting the energy required to heat the sample pan *without the foam sample* from the energy required to heat the sample pan with the foam sample. A separate experiment is used to determine the energy required to heat just the sample pan.

The sensible enthalpy is determined using the following equation:

$$q_{sen} = mC_p \frac{dT}{dt} \, , \tag{106}$$

where m, C_p, and dT/dt represent the sample mass, sample heat capacity, and sample temperature ramp rate, respectively. The sample mass can be determined using the initial mass, m^o, and the solid fraction calculated with the SREF chemistry model since

$$m = m^o S_f \, . \tag{107}$$

The SREF predictions of the solid mass fraction will be shown in Section 9.3 (Table 12) to give a root mean squared error of 2.6% for an unconfined sample ramped at 20ºC/min. Thus, error associated with using the SREF model to predict the mass in the DSC is negligible.

Figure 10 shows reported heat capacity data [28-29] for REF100 and a preliminary heat capacity model [30] based on this data as a black solid line. The open circles represent Dobranich and Gill's data [28] up to about 100ºC and Aselage's data [29] is represented as triangles with results up to 350ºC. Aselage reported three additional experiments represented as gray lines in Fig. 10. Aselage's 2nd through 4th experiments having similar shapes. The four experiments were all run with the same sample. One problem with running the same sample for all four experiments is that almost half of the initial sample mass decomposes at 350ºC as indicated by a similar TGA experiment which was shown in Fig. 3.B. Also, the heat capacity data in Fig. 10 was evaluated without considering reaction enthalpies. Neglecting reaction enthalpy is acceptable provided the sample temperature is below significant reaction thresholds. Only heat capacity data up to the glass transition temperature is considered in the current report to avoid confounding sensible enthalpy with reaction enthalpy effects.

Figure 11 shows the heat capacity used to evaluate the sensible enthalpy given by eqn (106) as a black line. In Fig. 11, the thick gray line is the heat capacity used in a preliminary model of the removable epoxy foam encapsulant [30] and the dashed line is the heat capacity of pyrolytic graphite [31]. The SREF heat capacity model, shown as the thick black line in Fig. 10, is

$$C_p = \begin{cases} 0.0011T + 0.033535 & T < 343.15\,\mathrm{K}\ \ (70°\mathrm{C}) \\ 0.411\dfrac{cal}{g\text{-}K} & T \geq 343.15\,\mathrm{K}\ \ (70°\mathrm{C}) \end{cases} \tag{108}$$

where C_p and T represent heat capacity in cal/g-K and temperature in K, respectively.

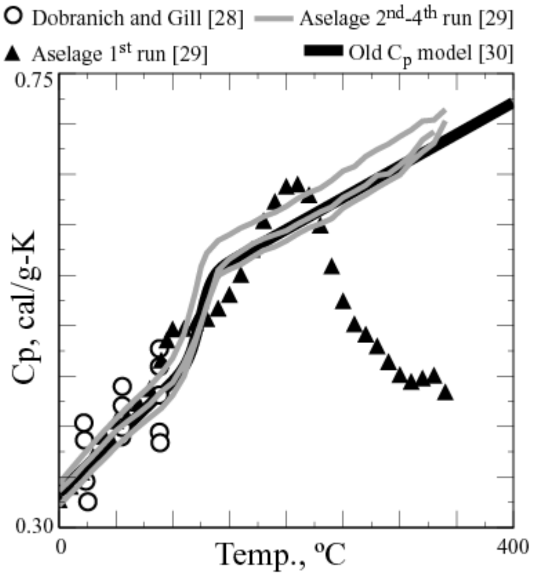

Fig. 10. Heat capacity for removable epoxy foam. Aselage's four runs were made with the same foam sample. The thick black line was used by Hobbs et al. [30] in a preliminary decomposition model.

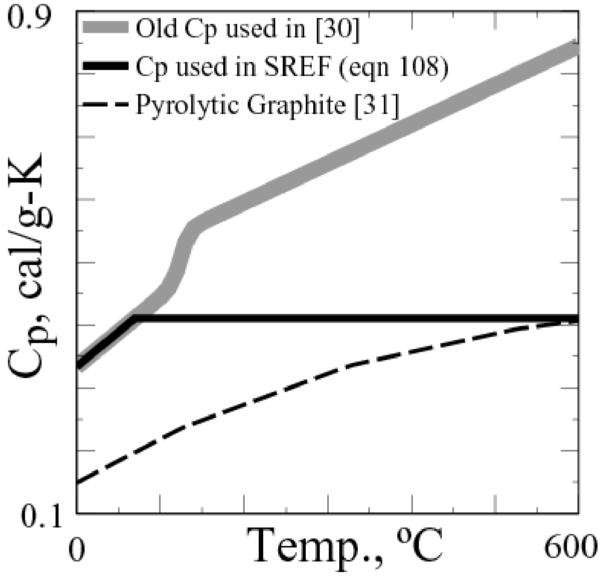

Fig. 11. Models of removable epoxy foam heat capacity (solid lines) and heat capacity data for pyrolytic graphite (dashed-line).

Initially, the old heat capacity model, represented as the thick gray line in Fig. 10, was used to determine the sensible enthalpy described by eqn (106). Using this old heat capacity model resulted in *exothermic* reaction enthalpies that are known to be endothermic as determined using the DSC data. The problem with the old heat capacity model was that the data was reduced without regard to reaction enthalpy. Reactions would bias the heat capacity results above the glass transition temperature. The new SREF heat capacity model described by eqn (108) only uses data up to the glass transition temperature, 70ºC. The heat capacity is assumed to be constant for temperatures greater than the glass transition temperature. The pyrolytic graphite heat capacity converges to the constant SREF heat capacity value at high temperatures where the degraded foam consists primarily of nonvolatile residues.

Figure 12.A shows the reaction enthalpy determined from eqn (105), the sensible enthalpy determined using eqn (106), and the measured heat flow to samples heated at 20ºC/min for three separate experiments. The sensible enthalpy is the same for each experiment since the heating rates were nearly identical. The measured heat flows to the samples were similar for experiment 1 and 3. The heat flow to the sample in experiment 2 is somewhat higher than experiment 1 and 3. The heat flow to the sample should be close to the sensible enthalpy at the end of each experiment when mass loss becomes negligible

In Fig. 12.A, the heat flow to the sample, q_{DSC}, near 1400 seconds starts to plateau indicating the end of significant reactions. The plateau should be equal to the sensible enthalpy. After 140 seconds, the differences between q_{sen} and q_{DSC} may be caused by an inadequate heat capacity model, drift in the DSC signal, or inaccuracy caused by extremely small residue mass at the end of the experiment. Data from runs 1 and 3 were used to obtain the SREF reaction enthalpy.

Figure 12.B shows the integral of the reaction enthalpy normalized by the initial mass of the sample for three experiments. The overall reaction enthalpy for the three experiments is determined when the extent of reaction is high, or in other words, the decomposition is complete. The reaction enthalpy [q_{rxn} in

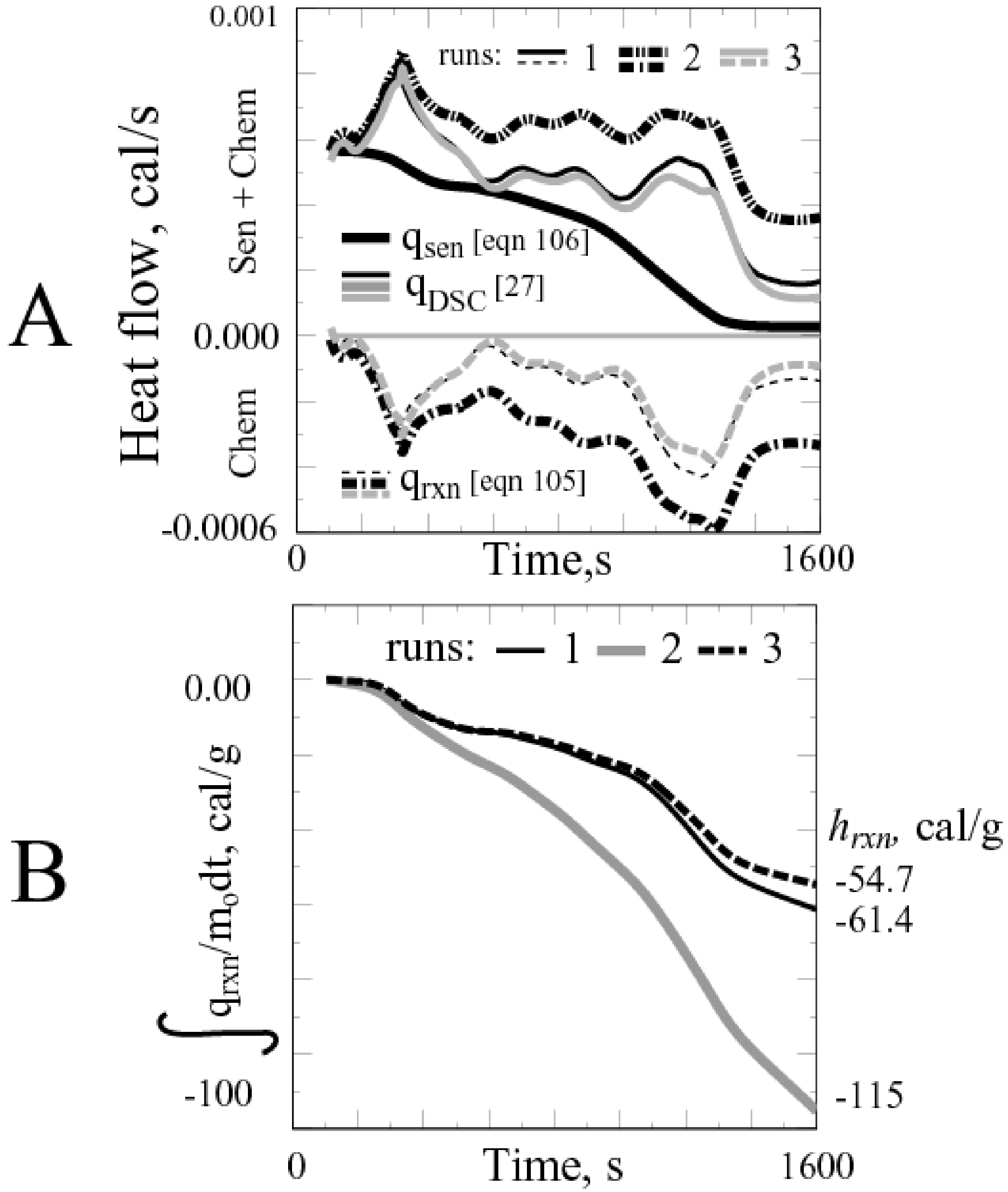

Fig. 12. A) Reaction enthalpy, q_{rxn}, determined from eqn (105), the sensible enthalpy, q_{sen}, determined using eqn (106), and the measured heat flow, q_{DSC}, to samples heated at 20ºC/min for three separate experiments. B) Integral of reaction enthalpy showing overall heat of reaction for three experiments. Results from experiment 2 are suspect

eqn (105)] must be integrated and normalized by the sample mass to obtain the overall reaction enthalpy for the REF encapsulant, as follows:

$$h_{rxn} = \int_0^T \frac{q_{rxn}}{m^o} dt \ , \tag{109}$$

where the units on the heat of reaction is cal/g. The heat of reaction in eqn (109) can be multiplied by the initial density of the foam to convert the heat of reaction into a volumetric source.

The value of the overall reaction enthalpy for the three experiments is -61.4, -115.0, and -54.4 cal/g as shown in Fig. 12.B, where a negative sign signifies that the overall reaction mechanism is endothermic. Again, the second reaction is suspect and the overall reaction enthalpy is expected to be the average of the reaction enthalpies measured in the 1 and 3 experiments, -57.9 cal/g. The overall reaction enthalpy for the rigid polyurethane foam was reported as -100 cal/g [6-8]. In Fig. 12.A, the heat flow due to chemistry accounts for the overall reaction enthalpy, which is associated with numerous reactions. The SREF model has four reaction steps with different reaction enthalpies associated with each reaction. The reaction enthalpies for the four SREF reactions were obtained using optimization techniques [25] to match the overall reaction enthalpy.

Figure 13.A shows the reaction enthalpy determined using the DSC data compared to the reaction enthalpy calculated with the SREF chemistry model for experiments 1 and 3. The SREF reaction enthalpies in Fig. 13 ware calculated by summing the enthalpy contributions from each of the four SREF reactions as follows:

$$q_{rxn} = \sum_{i=1}^{4} r_i q_i \, / \, m^o \tag{110}$$

where r_i and q_i represent four SREF reaction rates given previously in Table 3 and the individual reaction enthalpies associated with each of these reactions, respectively. Figure 13.B shows a comparison between the integral of the reaction enthalpies determined using the DSC data and the integral of the reaction enthalpies calculated with the SREF model.

Figure 13.C shows the contributions of the individual reaction enthalpies for the four SREF reactions to the overall reaction enthalpy for run 1 and run 3. The recommended reaction enthalpies for the SREF model are the average of these values. In other words, the reaction enthalpies for the SREF reactions 1 through 4 are -61, -11, -101, and +82 cal/g, respectively. The overall reaction enthalpy is –57.9 cal/g. The individual reaction enthalpies do not sum to the overall reaction enthalpy. The overall reaction enthalpy depends on the individual reaction rates as shown in eqn (110). The plots in Fig. 13.A show that the SREF prediction of the overall reaction enthalpy and the measured reaction enthalpy are within 4% of each other.

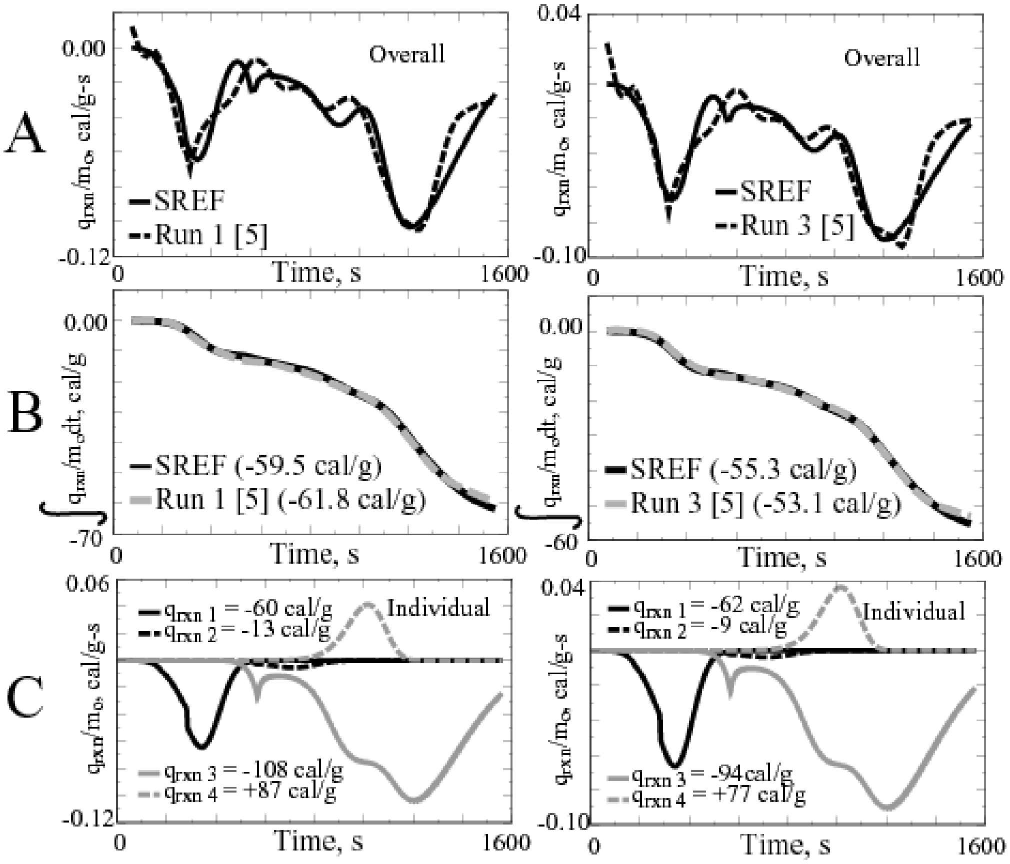

Fig. 13. A) Reaction enthalpy, q_{rxn}, B) integral of reaction enthalpy showing overall heat of reaction, and C) individual SREF reaction enthalpies for two samples heated at 20ºC/min. Both measured [27] and predicted enthalpy results are shown in A and B.

9. TGA Experiments and Predictions

The TGA apparatus is composed of 1) a microbalance used to measure mass loss associated with thermal decomposition, 2) a thermocouple in close proximity to the sample to determine the foam temperature, and 3) purge gas to sweep away decomposition gases from the surface of the sample. Sample sizes were chosen to minimize size effects and to maximize the signal-to-noise ratio. TGA data was obtained from two laboratories located at Sandia National laboratories (SNL) in Albuquerque, NM, and Brigham Young University (BYU) in Provo, UT.

Table 10 lists 68 REF100 LPTGA experiments, two LPTGA experiments using REF200, and two LPTGA experiments using REF300. The 68 REF100 TGA experiments at SNL are referred to as low-pressure TGA (LPTGA) experiments since the experiments were performed at ambient pressure. Table 11 lists 65 experiments performed at BYU using REF100 samples. The 65 REF100 experiments performed at BYU are referred to as high-pressure TGA (HPTGA) experiments since the BYU apparatus can be operated at pressures as high as 100-atm using a high-pressure purge gas. A high thermal conductivity purge gas was used with the HPTGA experiments to insure that the thermocouple temperature was sufficiently close to the sample temperature. Erickson et al. [5] and Clayton [4] give more information regarding the LPTGA and HPTGA experiments, respectively.

Table 10. Low-pressure TGA experiments [5] and RMS error

Primary Effect	Secondary Effect	Orifice	Foam Type	Run #	Description	Mass, mg	RMS, %	Time, s
5°C/m ramp	High-density unconfined powders	open pan	100	1	r05.h.u.p.0620	4.542	4.40	6935
		open pan	100	2	r05.h.u.p.0620r	4.508	4.08	6878
	Low-density unconfined powders	open pan	100	3	r05.l.u.p.0501	4.309	2.38	6907
		open pan	100	4	r05.l.u.p.0523	4.576	2.73	6871
20°C/m ramp	High-density unconfined cylinders	open pan	100	5	r20.h.u.c.0612	4.476	4.02	1725
		open pan	100	6	r20.h.u.c.0627	4.619	3.09	1727
		open pan	100	7	r20.h.u.c.0627r	4.577	3.01	1728
	High-density unconfined powders	open pan	100	8	r20.h.u.p.0612	4.516	4.46	1734
		open pan	100	9	r20.h.u.p.0807	2.491	1.29	1729
		open pan	100	10	r20.h.u.p.0808	2.53	1.31	1728
	Low-density unconfined cylinders	open pan	100	11	r20.l.u.c.0524	4.61	3.11	1704
		open pan	100	12	r20.l.u.c.0529	4.384	4.04	1647
	Low-density unconfined powders	open pan	100	13	r20.l.u.p.0522	4.709	1.37	1721
		open pan	100	14	r20.l.u.p.0809	2.503	1.85	1727
		open pan	100	15	r20.l.u.p.1103	4.478	1.19	2317
		open pan	100	16	r20.l.u.p.1214	4.348	1.38	1722
	High-density confined powders	2-mm	100	17	r20.h.2mm.p.0613	4.427	3.54	1716
		2-mm	100	18	r20.h.2mm.p.0614	4.523	3.40	1729
		1-mm	100	19	r20.h.1mm.p.0615	4.464	2.66	1730
		1-mm	100	20	r20.h.1mm.p.0615r	4.566	2.80	1726
		350-µm	100	21	r20.h.350.p.0626	4.454	2.21	1722
		350-µm	100	22	r20.h.350.p.0627	4.497	2.03	1726
		200-µm	100	23	r20.h.200.p.0621	4.584	2.85	1727
		200-µm	100	24	r20.h.200.p.0626	4.548	2.76	1727
		60-µm	100	25	r20.h.60.p.0613	4.462	3.74	1728
		60-µm	100	26	r20.h.60.p.0613r	4.564	2.78	1720
	Low-density confined powders	2-mm	100	27	r20.l.2mm.p.0613	4.524	1.57	1729
		2-mm	100	28	r20.l.2mm.p.0614	4.572	1.64	1727
		1-mm	100	29	r20.l.1mm.p.0606	4.509	1.85	1731
		1-mm	100	30	r20.l.1mm.p.0606r	4.487	1.79	1727
		350-µm	100	31	r20.l.350.p.0605	4.541	2.18	1728
		350-µm	100	32	r20.l.350.p.0605r	4.471	2.10	1730
		200-µm	100	33	r20.l.200.p.0604	4.269	2.50	1731
		200-µm	100	34	r20.l.200.p.0605	4.381	2.41	1730
		60-µm	100	35	r20.l.60.p.1103	4.266	3.57	1706
		60-µm	100	36	r20.l.60.p.1215	4.68	3.09	1719
50°C/m ramp	Low-density unconfined powder	open pan	100	37	r50.l.u.p.0501	4.532	1.87	929
		open pan	100	38	r50.l.u.p.0524	4.494	1.74	923
140°C isothermal	Low-density unconfined powder	open pan	100	39	i140.l.u.p.0710	4.5	1.37	54332
		open pan	100	40	i140.l.u.p.0716	4.468	3.11	86726
		open pan	100	41	i140.l.u.p.0720	4.519	4.64	240264
		open pan	100	42	i140.l.u.p.0726	4.503	4.67	320694
270°C isothermal	High-density unconfined powder	open pan	100	43	i270.h.u.p.0618	4.538	4.22	18285
		open pan	100	44	i270.h.u.p.0625	4.506	3.86	18289
270°C isothermal	Low-density unconfined powder	open pan	100	45	i270.l.u.p.0502	4.371	5.55	18291
		open pan	100	46	i270.l.u.p.0529	4.483	5.12	18295
		open pan	100	47	i270.l.u.p.0711	4.502	10.5	87107
		open pan	100	48	i270.l.u.p.0712	4.635	11.0	264573
300°C isothermal	High-density confined powder	60-µm	100	49	i300.h.60.p.0705	4.511	8.44	18327
		60-µm	100	50	i300.h.60.p.0706	4.451	8.23	18323
		60-µm	100	51	i300.h.60.p.0719	4.5	8.95	6329
		60-µm	100	52	i300.h.60.p.0719r	4.545	8.36	3326
		60-µm	100	53	i300.h.60.p.0720	4.522	11.4	2128
		60-µm	100	54	i300.h.60.p.0720r	4.617	1.74	443

Table 10 (cont.) Low-pressure TGA experiments [5] and RMS error

Primary Effect	Secondary Effect	Orifice	Foam Type	Run #	Description	Mass, mg	RMS, %	Time, s
300°C isothermal	Low-density confined powder	60-μm	100	55	i300.l.60.p.0702	4.468	8.64	18328
		60-μm	100	56	i300.l.60.p.0703	4.488	9.28	18324
350°C isothermal	High-density confined powder	60-μm	100	57	i350.h.60.p.0723	4.478	6.90	2189
140/270°C dual	High-density unconfined powder	open pan	100	58	i140-270.h.u.p.0615	4.49	5.00	9915
140/270°C dual isothermal	Low-density unconfined powder	open pan	100	59	i140-270.l.u.p.0514	4.89	2.28	9915
		open pan	100	60	i140-270.l.u.p.0525	4.566	2.40	9904
		open pan	100	61	i140-270.l.u.p.0531	4.518	2.21	9922
		open pan	100	62	i140-270.l.u.p.0628	4.534	2.25	9917
		open pan	100	63	i140-270.l.u.p.0802	4.498	2.42	9912
140/300°C dual	High-density confined powder	60-μm	100	64	i140-300.h.60.p.0618	4.469	10.2	9832
140/300°C dual	Low-density confined powder	60-μm	100	65	i140-300.l.60.p.0530	5.023	8.15	9834
		60-μm	100	66	i140-300.l.60.p.0531	4.389	10.4	9833
		60-μm	100	67	i140-300.l.60.p.0607	4.487	8.99	9833
		60-μm	100	68	i140-300.l.60.p.0607r	4.487	8.99	9833
					Average (68 runs)	**4.426-mg**	**4.24%**	

20°C/m ramp	Low-density confined powder	open pan	200	134	r20.l.u.p.0206.200	4.551	0.90	1723
		open pan	200	135	r20.l.u.p.0207.200	4.640	1.39	1727
		open pan	300	136	r20.l.u.p.0207.300	4.420	2.29	1718
		open pan	300	137	r20.l.u.p.0207r.300	4.495	2.29	1715
					Average (4 runs)	**4.527-mg**	**1.72%**	

Table 11. High-pressure TGA experiments [4] and RMS error

Primary Effect	Secondary Effect	P, atm	Run #	Description	Mass, mg	RMS, %	time, s
10°C/m ramp	High-density polyhedron samples	1	69	r10.h.1.1	2.044	3.14	3402
			70	r10.h.1.2	2.015	3.65	3402
	Low-density polyhedron samples	1	71	r10.l.1.1	2.428	3.65	3402
			72	r10.l.1.2	2.801	2.67	3402
			73	r10.l.1.3	2.401	3.66	3402
			74	r10.l.1.4	2.445	2.71	3402
20°C/m ramp	High-density polyhedron samples	1	75	r20.h.1.1	3.206	2.20	1811
			76	r20.h.1.2	2.232	6.04	1811
			77	r20.h.1.3	2.459	2.49	1811
	Low-density polyhedron samples	1	78	r20.l.1.1	4.712	1.78	1811
			79	r20.l.1.2	3.029	2.38	1811
			80	r20.l.1.3	3.725	2.30	1811
			81	r20.l.1.4	5.086	2.35	1811
	High-density polyhedron samples	10	82	r20.h.10.1	2.52	3.85	1811
			83	r20.h.10.2	2.793	4.92	1811
			84	r20.h.10.3	2.115	5.01	1811
			85	r20.h.10.4	1.31	3.83	1811
	Low-density polyhedron samples	10	86	r20.l.10.1	3.191	4.14	1811
			87	r20.l.10.2	2.789	3.44	1811
			88	r20.l.10.3	1.844	2.13	1811
			89	r20.l.10.4	1.704	2.96	1811
			90	r20.l.10.5	1.794	2.42	1811
	High-density polyhedron samples	30	91	r20.h.30.1	1.982	5.06	1811
			92	r20.h.30.2	2.4	6.31	1811
	Low-density polyhedron samples	30	93	r20.l.30.1	3.315	8.31	1811
			94	r20.l.30.2	2.601	5.27	1811
			95	r20.l.30.3	3.226	5.02	1812
	High-density polyhedron samples	50	96	r20.h.50.1	2.665	5.80	1811
			97	r20.h.50.2	3.497	5.26	1811
	Low-density polyhedron samples	50	98	r20.l.50.1	4.063	5.30	1811
			99	r20.l.50.2	2.469	4.42	1811
			100	r20.l.50.3	2.503	6.52	1811
			101	r20.l.50.4	2.653	3.65	973
			102	r20.l.50.5	2.119	5.62	1260
	Low-density polyhedron samples	70	103	r20.l.70.1	2.167	7.82	1811
			104	r20.l.70.2	2.825	10.6	1811
			105	r20.l.70.3	1.919	12.2	1811
			106	r20.l.70.4	2.212	10.2	1811
			107	r20.l.70.5	2.612	6.83	1811
40°C/m ramp	High-density polyhedron samples	1	108	r40.h.1.1	2.419	1.94	1043
	Low-density polyhedron samples	1	109	r40.l.1.1	2.774	3.60	1043
			110	r40.l.1.2	1.995	3.23	1044
			111	r40.l.1.3	1.875	2.84	1043
			112	r40.l.1.4	2.764	2.71	1043

Table 11 (cont.) High-pressure TGA experiments [4] and RMS error

Primary Effect	Secondary Effect	P, atm	Run #	Description	Mass, mg	RMS, %	time, s
200°C isothermal	High-density polyhedron samples	1	113	i200.h.1.1	3.827	2.19	3616
			114	i200.h.1.2	3.81	1.18	2102
			115	i200.h.1.3	2.054	3.38	5430
	Low-density polyhedron samples	1	116	i200.l.1.1	4.061	2.17	7243
			117	i200.l.1.2	2.98	2.57	7243
200°C isothermal	High-density polyhedron samples	1	118	i300.h.1.1	2.438	8.16	7243
			119	i300.h.1.2	2.532	4.40	3637
			120	i300.h.1.3	2.213	6.76	4666
	Low-density polyhedron samples	1	121	i300.l.1.1	5.509	5.64	7243
			122	i300.l.1.2	3.815	6.42	7244
300°C isothermal	High-density polyhedron samples	10	123	i300.h.10.1	1.8	4.23	4766
			124	i300.h.10.2	1.731	5.82	7243
			125	i300.h.10.3	2.636	7.18	7243
			126	i300.h.10.4	2.964	2.62	2473
			127	i300.h.10.5	2.215	4.27	3681
			128	i300.h.10.6	1.707	4.44	5387
400°C isothermal	High-density polyhedron samples	1	129	i400.h.1.1	4.107	0.516	7243
			130	i400.h.1.2	2.054	1.12	5387
			131	i400.h.1.3	2.212	2.94	3695
	Low-density polyhedron samples	1	132	i400.l.1.1	2.081	2.89	7243
			133	i400.l.1.2	2.215	3.37	2616
				Average (65 runs)	**2.687-mg**	**4.35%**	

9.1 LPTGA Experimental Matrix

The LPTGA experiments listed in Table 10 are separated into primary and secondary effects. The primary effects describe the thermal history of each of the samples. The thermal history of each of the LPTGA experiments is given in Figs. 14.A, 14.B, and 14.C. The secondary effects in Table 10 describe the density and state of the samples. The samples were obtained from either high-density foam (ρ_H = 0.32 g/cm^3) or low-density foam (ρ_H = 0.13 g/cm^3). A detailed description of each experiment is also given in Table 10. In the description column of Table 10, five descriptors are separated by periods. The first descriptor represents the thermal history of the sample. The first descriptor starts with either an "r" or an "i" which represents either a nonisothermal ramped experiment or an isothermal experiment.

The TGA records the sample mass (*m*) versus temperature or time. Typically, the normalized sample mass or solid fraction ($S_f = m/m_o$) is plotted as a function of temperature if the sample is ramped at a constant heating rate. If the sample is held at a constant temperature, the normalized sample mass is plotted as a function of time. The TGA experiments discussed in the current report were performed using a variety of heating conditions that included nonisothermal "ramped" experiments as well as "isothermal" experiments. The temperatures of the samples in the ramped experiments were increased at constant heating rates (5ºC/min, 10ºC/min, 20ºC/min, 40ºC/min and 50ºC/min) from ambient temperature to about 575ºC. The five nonisothermal ramped experiments in this report are referred to in the first descriptor as 5, 10, 20, 40, and 50 representing temperature ramp rates of 5ºC/min, 10ºC/min, 20ºC/min, 40ºC/min, or 50ºC/min, respectively.

Two types of isothermal experiments were considered – "one-step isothermal" and "two-step isothermal" experiments. The "one-step isothermal" experiments addressed samples quickly heated (20ºC/min) from ambient temperature to various set temperatures; the sample temperature was then held at the set temperature for two hours or longer. The "two-step isothermal" experiments addressed samples quickly heated (20ºC/min) from ambient temperature to a temperature of 140ºC; the samples were then held at 140ºC for about an hour. Following this first constant temperature period, the "two-step isothermal"

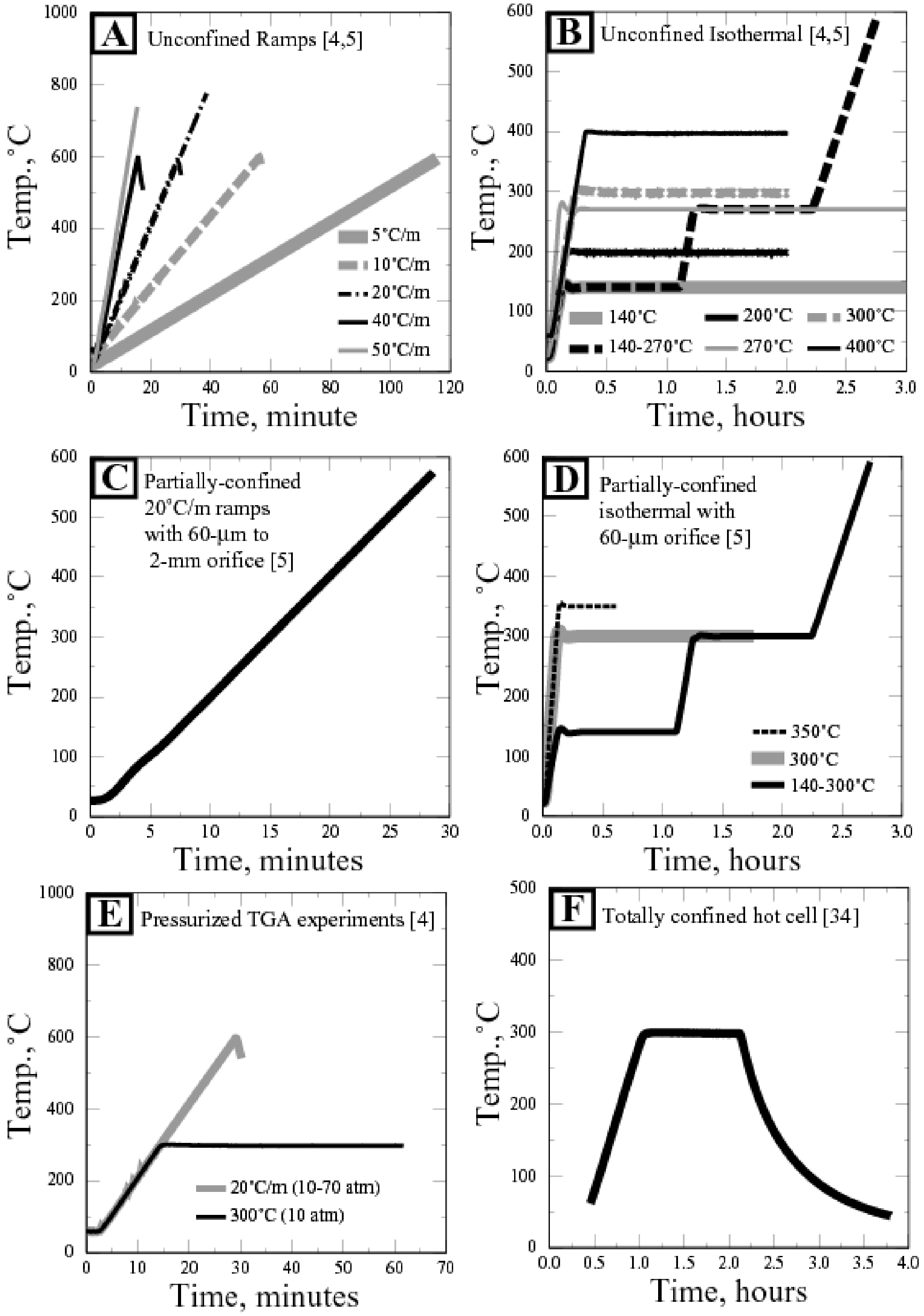

Fig. 14. Measured temperature histories for the 133 TGA experiments [4,5] described in Tables 10-12 and the two hot cell temperature histories described in Section 10. The sample temperatures for the unconfined TGA experiments are given in A and B; the sample temperatures for the partially-confined TGA experiments are given in C and D; and the sample temperatures for the pressurized TGA experiments are given in E.

samples were then quickly heated (20ºC/min) from 140ºC to 270ºC, the samples were then held at 270ºC for about an hour or more. The isothermal experiments are referred to in the first descriptor in Table 10 as 140, 140/270, 200, 270, 300, and 400 representing 140ºC one-step isothermal experiments, 140ºC/270ºC dual isothermal experiments, 200ºC one-step isothermal experiments, 270ºC one-step isothermal experiments, 300ºC one-step isothermal experiments, and 400ºC one-step isothermal experiments, respectively.

The second descriptor in Table 10 is either an “l” or an “h” which represents low-density or high-density foam, respectively. The third descriptor in Table 10 is either a “u”, “2mm”, “1mm”, “350”, “200”, or “60”, which represents the degree that the decomposition products are confined. The “u” represents unconfined decomposition using an open sample pan. The descriptors “2mm” and “1mm” represent 2-mm and 1-mm orifice diameters, respectively for the partially-confined LPTGA experiments. The partially-confined LPTGA experiments consider samples in hermetically sealed aluminum sample pans with various sizes of orifices in the crimp-sealed pans. The descriptors “350”, “200”, and “60” represent the orifice diameters in microns. The fourth descriptor in Table 10 is either a “p” or a “c” to represent whether or not the TGA sample was a powder or a cylinder. The fifth descriptor in Table 10 represents the month and day that the sample was run. If the fifth descriptor ends in an “r” then the run was a repeat or duplicate run. Only the REF200 and REF300 samples have a sixth descriptor that is either a 200 or 300, which represents REF200 or REF300, respectively.

Table 10 also gives the mass of the LPTGA sample for each of the runs. The average sample size for the 68 REF100 samples was 4.426-mg. The average sample size for the 4 REF200 and REF300 samples was 4.527-mg. Run number 13 was used to determine the kinetic parameters listed in Table 7 for the polymer decomposition reactions 2-4. Run number 39 was used to obtain the desorption kinetics for reaction 1 in Table 7. Run 13 and 39 were selected to obtain the SREF kinetics since these samples were low-density powders and were thought to have the least experimental uncertainty. Other experiments could have been used to determine the mean SREF kinetics, but runs 13 and 39 were thought to be representative of the unconfined TGA data set that were least influenced by confinement or mass transport effects. The average response of experiments performed with the high-density cylindrical foam samples was similar to the low-density powdered foams. However, the low-density powdered foams have less scatter than the high-density cylindrical samples.

9.2 HPTGA Experimental Matrix

Table 11 lists 65 HPTGA experiments performed at BYU using REF100 samples. The primary thermal history effects are similar to the LPTGA experiments. However, the HPTGA foam samples were always performed with polyhedron shaped foam samples rather than powdered samples. There are four descriptors listed for the HPTGA data. The first descriptor is the same as the first descriptor in Table 10 where an “r” represents a ramped experiment and an “i” represents an isothermal experiment. The second HPTGA descriptor is either an “h” or an “l” representing either high-density foam or low-density foam. The third descriptor represents the system pressure in atmospheres. The fourth descriptor represents the experiment number run at nominally the same conditions. The average HPTGA sample mass was 2.7-mg.

9.3 RMS errors

Tables 10 and 11 give the absolute percent root mean squared error (RMS error) for each of the TGA experiments:

$$\%\,\text{RMS error} = 100\sqrt{\frac{\sum_{i=1}^{n}\left(S_{f,i}^{SREF} - S_{f,i}^{data}\right)^2}{n}}\ . \tag{111}$$

The absolute percent RMS error for each TGA experiment was calculated by subtracting the measured solid fraction, $S_{f,i}^{data}$, from the solid fraction calculated with eqn (76), $S_{f,i}^{SREF}$, at various temperature history points i for a total of n points. Usually, 100 or more points were used to define the solid fraction profiles. The average of the RMS error for the LPTGA and HPTGA experiments was 4.2% and 4.4%, respectively.

The 133 REF100 LPTGA and HPTGA experiments can be classified into three test categories that include unconfined ambient pressure experiments (5 ramped and 6 isothermal runs), partially-confined ambient pressure experiments (5 ramped and 3 isothermal runs), and unconfined high-pressure experiments (4 ramped and 1 isothermal run) as shown in Table 12. The average RMS errors for each of these classifications are also given in Table 12. The average percent RMS errors for the unconfined ambient pressure experiments, the partially-confined ambient pressure experiments, and the unconfined high pressure experiments were 3.4%, 5.0%, and 5.5%, respectively. The average RMS error for all 133 experiments was 4.1%. The higher RMS errors for the partially-confined and high-pressure experiments were due to higher run-to-run experimental variability for these conditions.

Table 10 and 11 also list the length of the TGA experiments in the last column marked as “Time”. Even though some of the TGA experiments were run for many hours, the agreement between the measured mass loss and predicted mass loss was remarkably good. For example, samples 42 and 48 were held at 140ºC and 270ºC for 89 hours and 73 hours, respectively. The RMS errors for experiments 42 and 48 were 4.67% and 4.64%, respectively.

9.4 Mean Value Analysis

The mean value method [24] was used to calculate the mean and standard deviation of the solid fraction as a function of the heating conditions by assuming that the input parameters are independent random variables and that the response is linear. The mean solid fraction, μ_{Sf}, and the standard deviation of the solid fraction, σ_{Sf}, was determined using a simple Taylor series expansion of solid fraction, $S_f(\xi_i)$, about the mean of the individual random variables or input parameters, μ_i, by neglecting higher order terms as follows:

$$\mu_{s_f} = S_f(\xi)\big|_{\xi=\mu} \tag{112}$$

Table 12. 133 LPTGA [5] and HPTGA [4] experiments separated into categories

Unconfined Ambient Pressure

	°C/m	runs	# of runs	avg RMS, %
Ramps	5	1-4	4	3.40
	10	69-74	6	3.25
	20	5-16,75-81	19	2.61
	40	108-112	5	2.86
	50	37-38	2	1.80
		subtotal:	***36***	***2.80***
	T, °C	**runs**	**# of runs**	**avg RMS, %**
Isothermal	140	39-42	4	3.45
	140/270	58-63	6	2.76
	200	113-117	5	2.30
	270	43-48	6	6.70
	300	118-122	5	6.28
	400	129-133	5	2.17
		subtotal:	***31***	***4.01***

Partially-Confined Ambient Pressure

	Orifice diameter	runs	# of runs	avg RMS, %
Ramp 20°C/m	2-mm	17, 18, 27, 28	4	2.54
	1-mm	19, 20, 29, 30	4	2.27
	350-µm	21, 22, 31, 32	4	2.13
	200-µm	23, 24, 33, 34	4	2.63
	60-µm	25, 26, 35, 36	4	3.30
		subtotal:	***20***	***2.57***
	T, °C	**runs**	**# of runs**	**avg RMS, %**
Isothermal 60-mm	300	49-56	8	8.14
	350	57	1	6.90
	140/300	64-68	5	9.35
		subtotal:	***14***	***8.48***

Unconfined High Pressure

	P, atm	runs	# of runs	avg RMS, %
Ramp 20°C/m	10	82-90	9	3.63
	30	91-95	5	5.99
	50	96-102	7	5.23
	70	103-107	5	9.53
		subtotal:	**26**	**5.65**
Isothermal, 300°C	**P, atm**	**runs**	**# of runs**	**avg RMS, %**
	10	123-128	6	4.76
		subtotal:	**6**	**4.76**

$$\sigma_{S_f}^2 = \sum_{i=1}^{n}\left[\sigma_i \frac{\partial S_f(\xi)}{\partial \xi_i}\Big|_{\xi=\mu}\right]^2 . \tag{113}$$

Equation (112) is a single-sample approximation of the mean solid fraction calculated as a function of temperature with eqn (76) with all input parameters, ξ, equal to the mean values, μ. In eqn (113), σ_{Sf} is the standard deviation of the solid fraction; σ_i is the standard deviation of the i^{th}-input parameter (random variable); and μ is a vector representing the mean input parameters.

The relative importance of each input variable to the uncertainty in the calculated solid fraction can be determined from the scaled sensitivity coefficients, γ_i, defined as:

$$\gamma_i = \tfrac{\sigma_i}{\sigma_{sf}} \times \frac{\partial S_f(\xi)}{\partial \xi_i} , \tag{114}$$

where

$$-1 \le \gamma_i \le 1 \tag{115}$$

and

$$\sum_{i=1}^{n} \gamma_i^2 = 1 . \tag{116}$$

The input variables that contribute the most to the uncertainty in the calculated solid fraction also have the largest absolute sensitivity values. The sign of the scaled sensitivity coefficients indicate that an increase in the input parameter value causes an increase in the value of the response function or solid fraction. Likewise, a negative sensitivity coefficient indicates that an increase in the input parameter value causes a decrease in the response function value. The square of the sensitivity coefficient is referred to as the importance factor, γ_i^2, which can be used to easily identify important input variables that contribute to the calculated uncertainty. The term "importance factor" is a misnomer. The importance factor only shows the relative importance of a parameter with respect to the uncertainty calculation. All model parameters are important and necessary to determine the foam response. The importance factors merely indicate which parameters contribute most to the response uncertainty. The importance factors are highly dependent on the estimates of the individual parameter uncertainty expressed in this report as a standard deviation.

Nineteen of the SREF parameters were included in the mean value analysis: four activation energies (E_i), four distribution parameters (σ_{Ei}), three diffusion parameters (d^*/ϕ_{BA}, d^*/ϕ_S, and $d^*/\phi_{polymer\ fragments}$), seven activity coefficient parameters (γ_i), and the system pressure (P). In eqns (113) and (114) the derivative were obtained using a central difference technique with a finite difference step size of 0.1 times the mean input parameter. Thirty-nine function evaluations were required to obtain the derivatives: two for each of the nineteen parameters considered in the sensitivity analysis and one evaluation using the mean input values.

The SREF model depends on pressure as given by eqns (7), (21), and (85). The user specifies the pressure if the pressure is regulated as in the high pressure TGA experiments discussed in Section 9.2. If the pressure is dynamic, as in the hot cell experiments discussed in Section 10, then the pressure is not specified, and other parameters such as the initial pressure, foam density, polymer density, and element volume need to be specified.

9.5 Ramped Run 13 (20ºC/min) and Isothermal Run 129 (400ºC)

Various predictions and measurements for a representative ramped and isothermal TGA experiment are presented in this section. Figure 15 shows various predictions and measurements for run 13, which is the 20ºC/min LPTGA run from which the kinetic parameters were extracted. Figure 16 shows various predictions and measurements from run 129 where the HPTGA sample temperature was held at 400ºC for two hours at ambient pressure. A temperature of 400ºC was high enough for all four of the SREF reaction steps to be significant.

Figure 15 shows the solid fraction, gas-phase mass fractions and gas fraction, populations, rate of gas species evolution, importance factors, and condensed mass for a sample temperature ramped at 20ºC/min. The gas fraction is defined as the mass of the gas products normalized by the initial condensed mass. The gas fraction can be obtained from the solid fraction as follows:

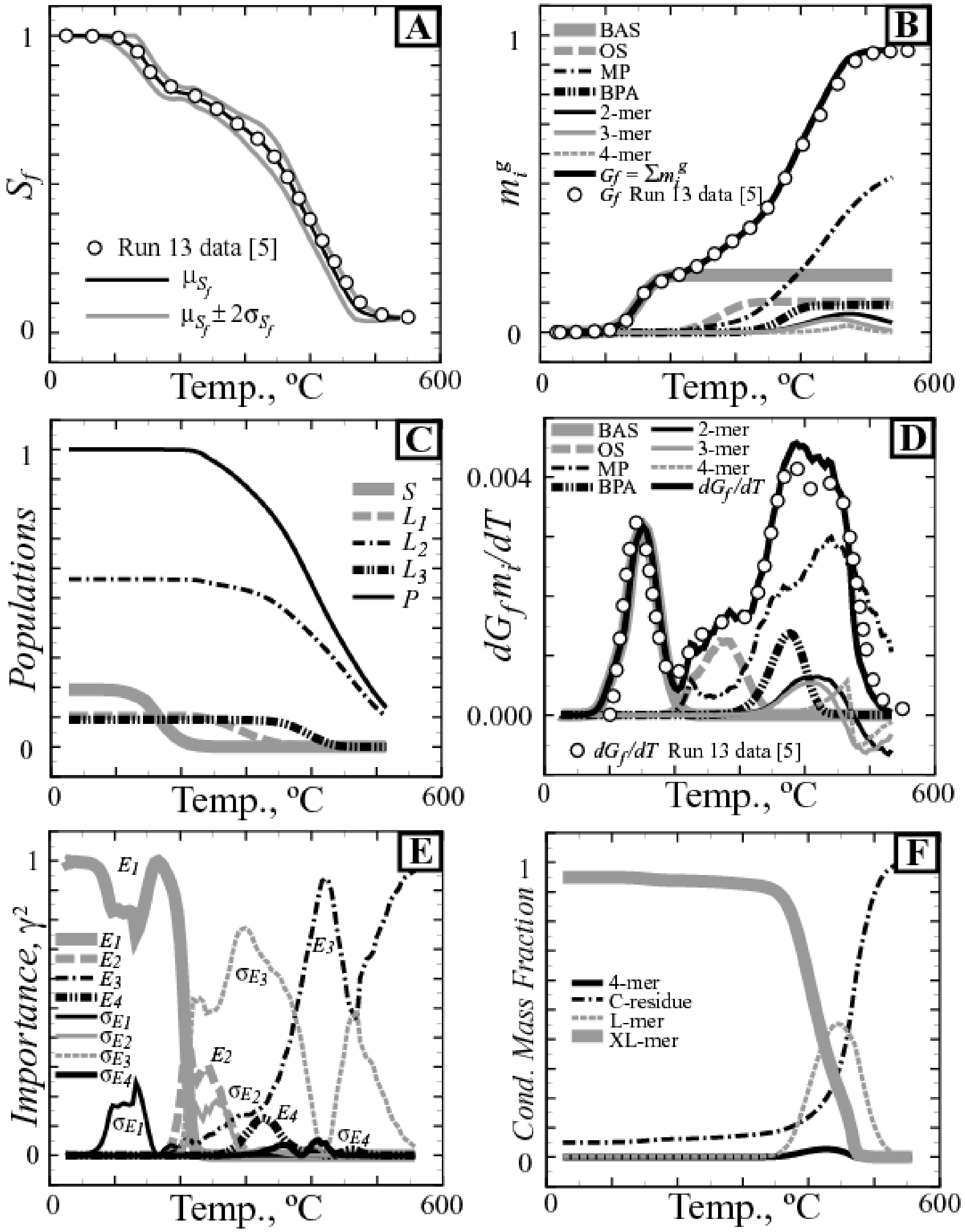

Fig. 15. Various predictions (lines) and measurements (open circles) of run 13 [5] with LPTGA sample heated at 20°C/min (see Fig. 14.A for temperature history): A) solid fraction, B) gas-phase mass fractions and gas fraction (G_f), C) populations, D) rate of gas species evolution divided by sample heating rate ($\mathrm{d}T/\mathrm{d}t$), E) importance factors, and F) condensed mass fractions.

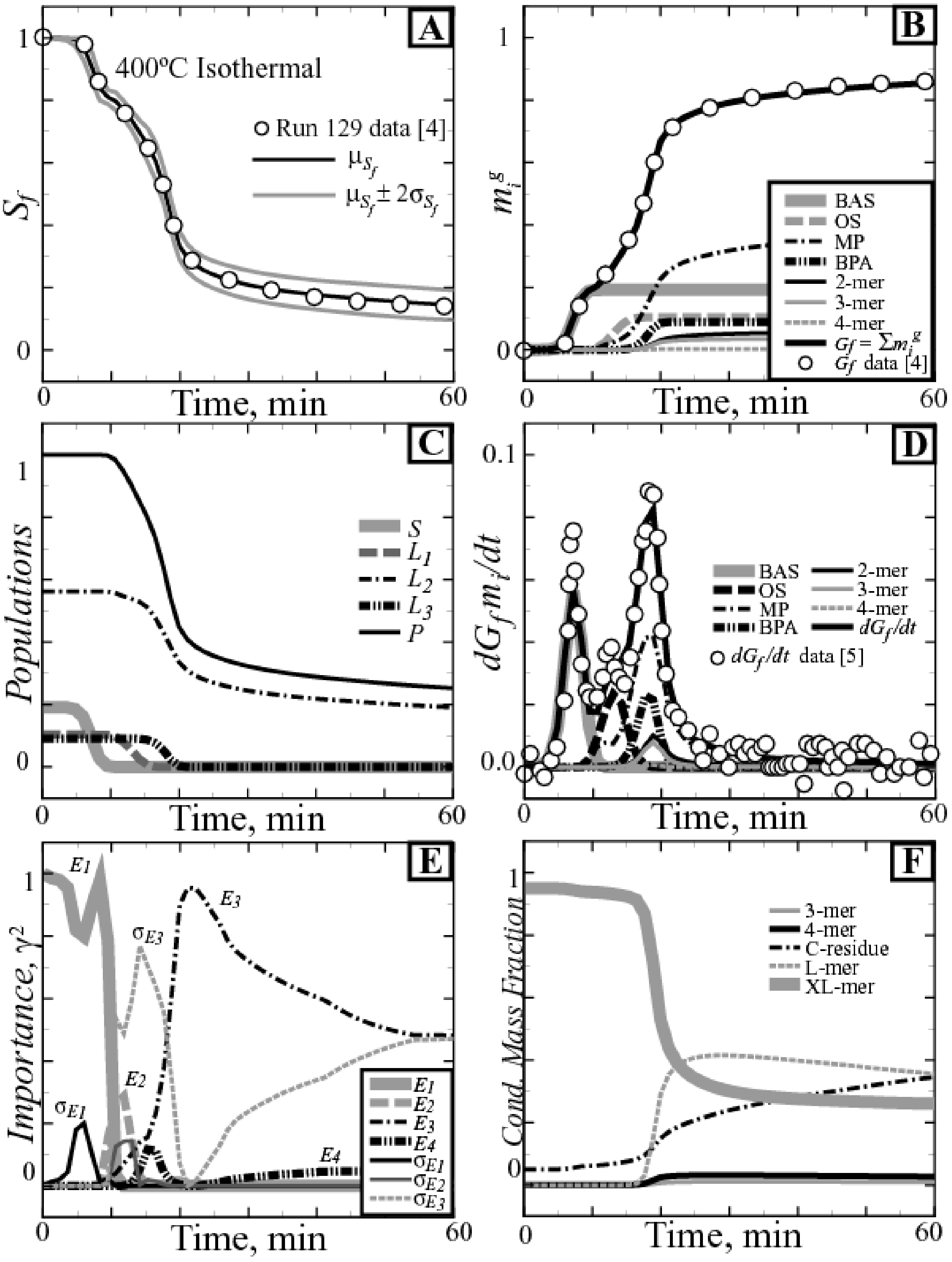

Fig. 16. Various predictions (lines) and measurements (open circles) of run 129 [4] with HPTGA sample heated quickly ramped to 400°C and held for 2 hours (see Fig. 14.B for temperature history): A) solid fraction, B) gas-phase mass fractions and gas fraction (G_f), C) populations, D) rate of gas species evolution, E) importance factors, and F) condensed mass fractions.

$$G_f = 1 - S_f \,. \tag{117}$$

In Fig. 15.A, the measured solid fraction, S_f, is plotted as open circles and the mean solid fraction, μ_{sf}, is plotted as a black line. The 95% prediction interval is plotted as gray lines and represents the mean solid fraction plus or minus two standard deviations, $\mu_{S_f} \pm 2\sigma_{S_f}$. The gas mass fractions and overall gas fraction in eqn (117) are plotted in Fig. 15.B. The rate of gas species evolution is plotted in Fig. 15.D. The rate of gas species evolution clearly shows which species are prevalent as the reaction progress. The overall rate of gas evolution is consistent with the measurements discussed in more detail by Erickson et al. [5].

The four SREF populations, S, L_1, L_2, and L_3 for run 13 are plotted in Fig. 15.C. The bridge population, p, is also plotted in Fig. 15.C. The critical bridge population, $p_c = 0.5$, occurs near a temperature of 400ºC. The primary reaction, from room temperature to about 200ºC, is reaction 1 that describes the desorption of the “sorbed” species, which evolve as BAS. Consequently the most important parameters in this region are the kinetic parameters for reaction 1 as shown in Fig. 15.E. The second reaction, responsible for OS evolution, is prominent between 200 and 300ºC. The reaction responsible for the mixed-product species (MP) is significant from about 200ºC to the end of the reaction. The fourth reaction, which is responsible for the BAS, is prevalent between 250 and 500ºC.

Figure 15.E displays the parameters that contribute the most to the uncertainty interval shown in Figure 15.A. All of the activation energies and distribution parameters contribute to the uncertainty in the solid fraction prediction. The other parameters, such as the diffusion lengths and activity coefficient parameters did not appreciably contribute to the uncertainty in the solid fraction prediction. The importance shows the parameters responsible for the uncertainty in the response variable, which was chosen as the solid mass fraction in Fig. 15. At the end of the run, the uncertainty approaches zero. Thus, the uncertainties at the tail end of the ramped experiments, where the uncertainty is essentially zero, do not have much meaning. Similar conclusions can be drawn from the various predictions and measurements for run 129 plotted in Fig. 16. The primary difference is that the last reaction that forms BPA does not go to completion. The RMS error for runs 13 and 129 were 1.37% and 0.52%, respectively.

9.6 Unconfined, Partially-Confined, Pressurized Data Comparisons

This section presents both predictions and measurements of mass loss for all of the TGA experiments listed in Tables 10-12. The plots are divided into categories similar to the categories listed in Table 12 where the unconfined, partially-confined, and pressurized TGA runs were grouped together. Figure 17, 18, and 19 show ramped TGA experiments that were unconfined, partially-confined, and pressurized, respectively. Figure 20 presents all of the isothermal TGA experiments including those that were unconfined, partially-confined, and pressurized. In Figs. 17-20, the measured solid fraction is compared to the mean SREF predictions. Ninety-five percent prediction intervals for each of the runs are shown in Figs. 17-20. Importance factors for some of the experiments are also given in Figs. 17-20.

Figure 17 shows the effect of temperature ramp rate for unconfined decomposition where the foam samples are decomposed in open pans at ambient pressure. The overall percent RMS error for the experiments shown in Fig. 17 is 2.8%. The importance factors for the 50ºC/min and 5ºC/min runs are shown in Fig. 17.H and 17.I. The sensitivity to the initial pressure is higher for the high-pressure experiments as shown in Fig. 19. Figure 18 shows the effect of confinement of the decomposition gases. The partially-confined samples were contained in a hermetically sealed aluminum pan with orifices of various dimensions. Partial-confinement of the decomposition gases cause the mass loss profiles to shift to higher temperatures as shown in Fig. 18.A and 18.B. The shift in the profile to higher temperatures is modeled empirically as a mass transport effect. Figure 18 shows the difference between the measured TGA profiles for different densities of foam with ρ_h and ρ_L representing the low-density and high-density foam samples, which were nominally 0.13 g/cm^3 (8 lb/ft^3) and 0.32 g/cm^3 (20 lb/ft^3). Some of the variability in the measured results are probably due to density variations and clogging of the orifice. The variability is on the same order as the 95% prediction interval.

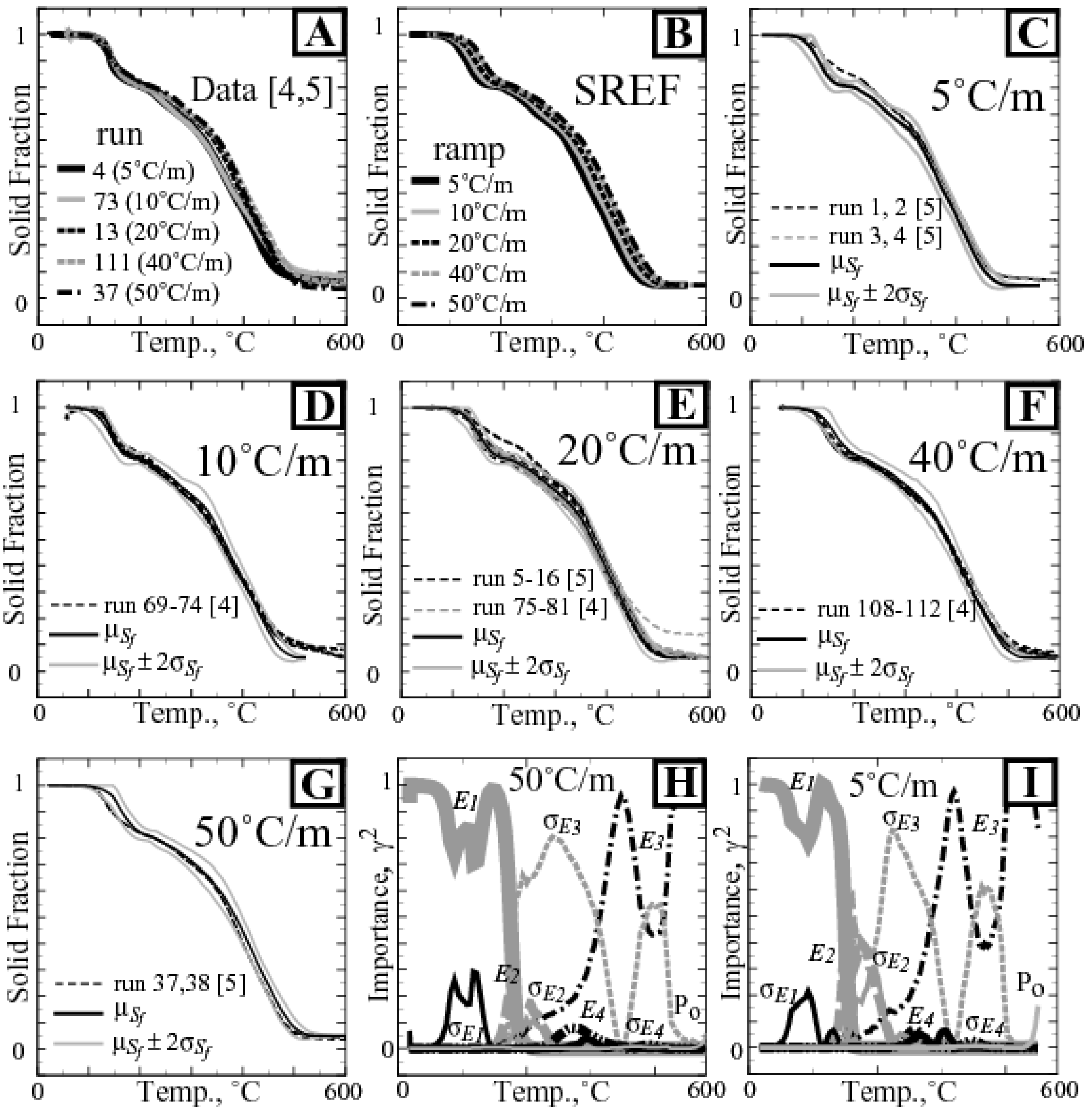

Fig. 17. Various predictions and measurements [4,5] of unconfined ramped TGA experiments at ambient pressure (see Fig. 14.A for temperature histories): A) measurements, B) SREF predictions, C) 5°C/min data and predictions, D) 10°C/min data and predictions, E) 20°C/min data and predictions, F) 40°C/min data and predictions, G) 50°C/min data and predictions, H) importance factors for 50°C/min predictions, and I) importance factors for 5°C/min predictions. Legend for H and I can be found in Fig. 15.E.

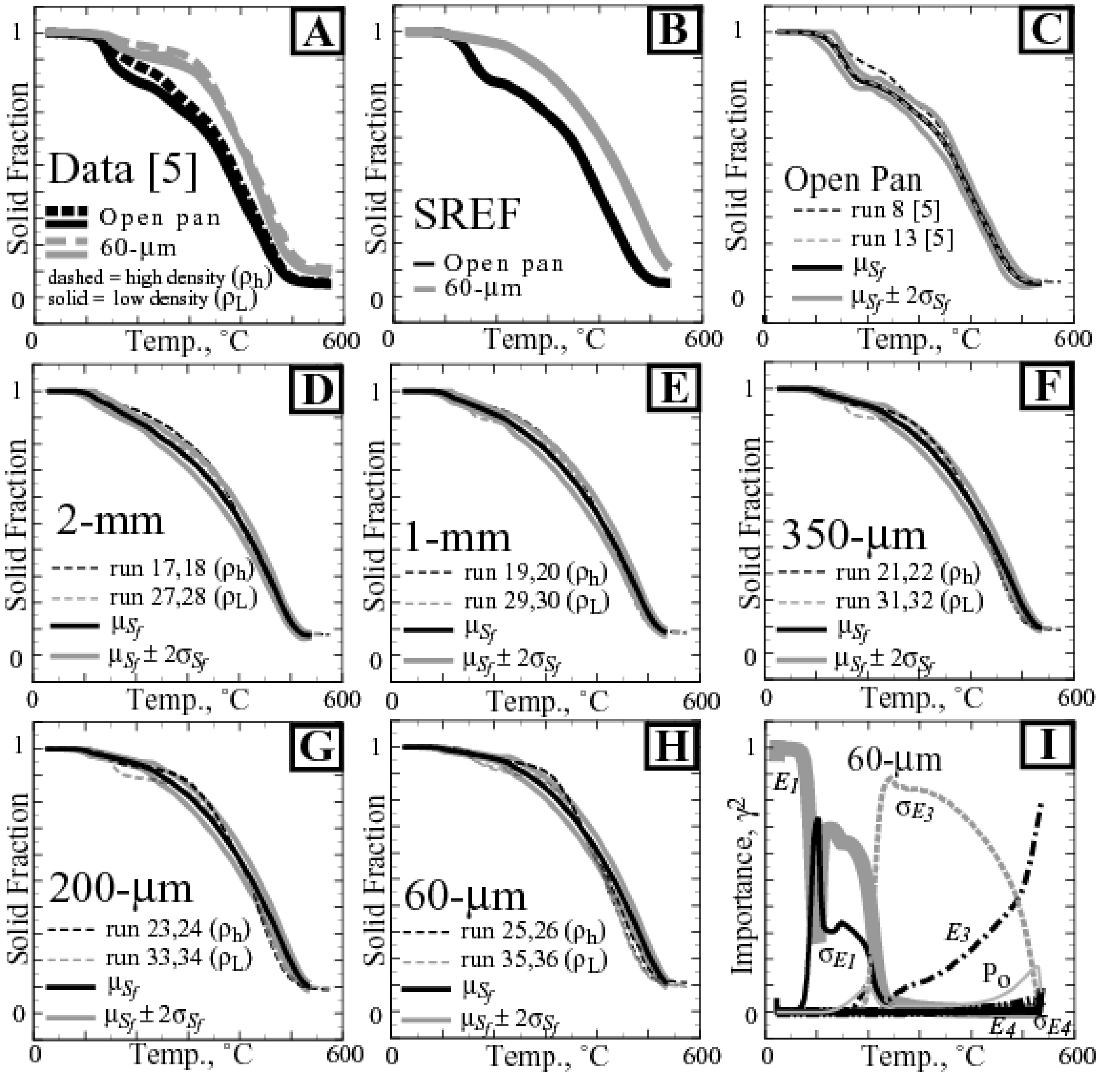

Fig. 18. Various predictions and measurements [5] of partially-confined TGA experiments ramped at 20°C/min (see Fig. 14.C for temperature histories) at ambient pressure: A) measurements, B) SREF predictions, C) open sample pan, D) 2-mm orifice diameter, E) 1-mm orifice diameter, F) 350-μm orifice diameter, G) 200-μm orifice diameter H) 60-μm orifice diameter, and I) importance factors for 60-μm orifice diameter predictions. Legend for I can be found in Fig. 15.E.

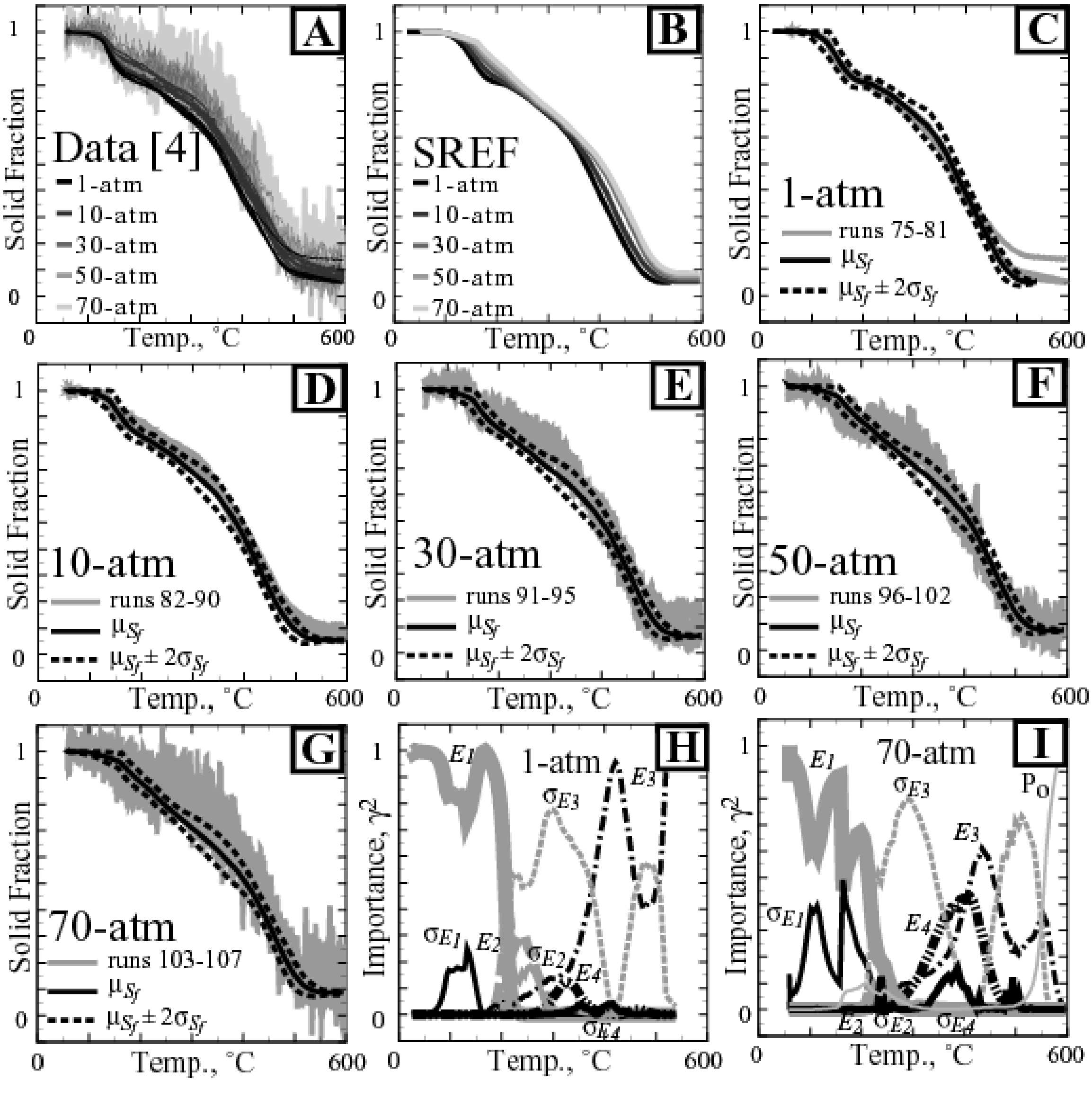

Fig. 19. Various predictions and measurements [4] of unconfined TGA experiments ramped at 20°C/min (see Fig. 14.A and 14.E for temperature histories) at various pressure: A) measurements, B) SREF predictions, C) 1-atm, D) 10-atm, E) 30-atm, F) 50-atm, G) 70-atm H) importance factors for 1-atm prediction, and I) importance factors for 70-atm prediction. Legend for H and I can be found in Fig. 15.E.

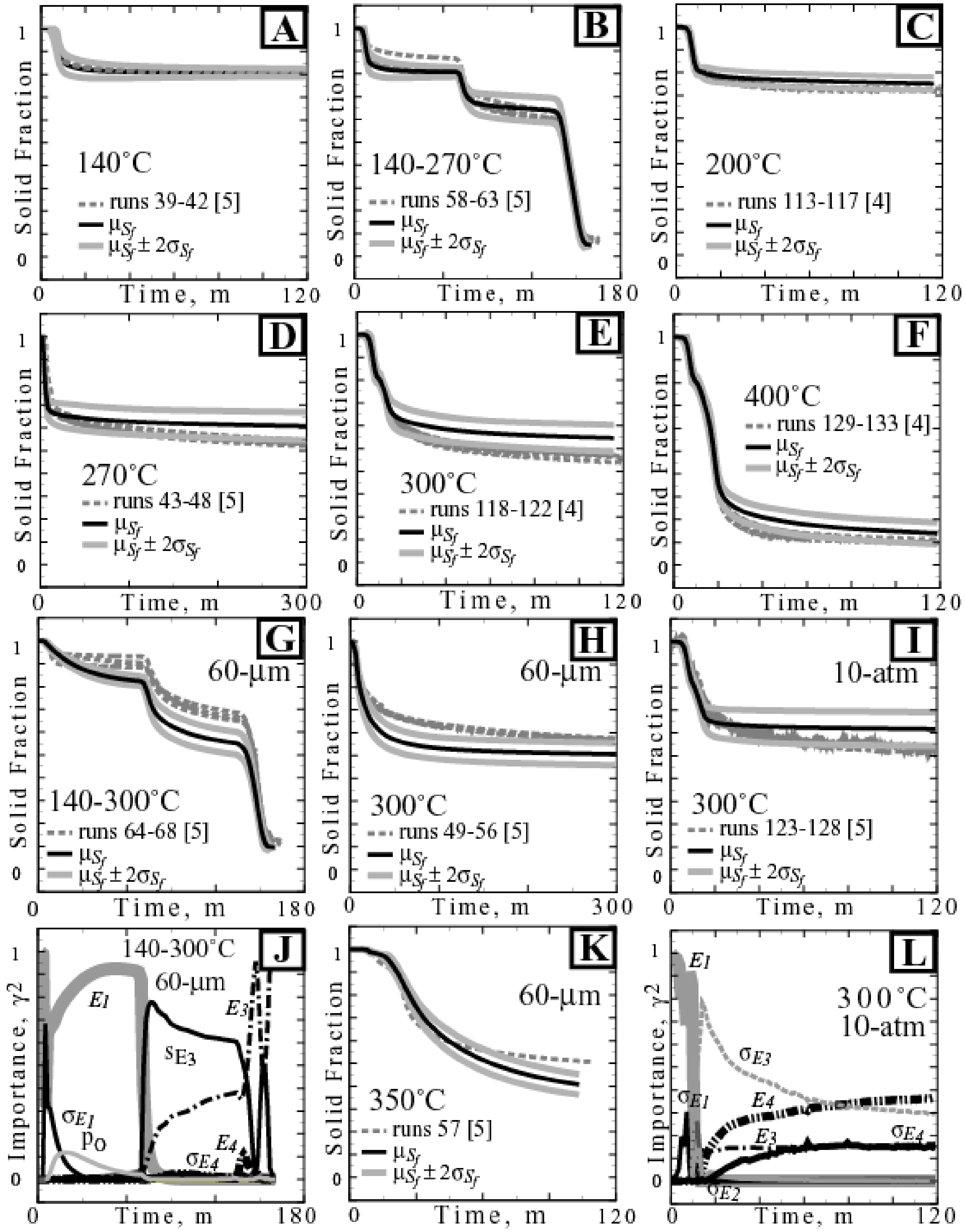

Fig. 20. Various predictions (solid lines) and measurements (dashed lines) [4,5] of isothermal TGA experiments at various pressure and levels of confinement. Figures 14.B, 14.D, and 14.E show the temperature histories for each of the following isothermal runs: A) 140°C, B) 140-270°C dual, C) 200°C, D) 270°C, E) 300°C, F) 400°C, G) 140-300°C, H) 300°C with 60-mm orifice, I) 300°C at10-atm, and K) 350°C with a 60-mm orifice. The legend for plots J and L can be found in Fig. 15.E.

Figure 18.I shows the importance factors for the ramped experiment with the 60-μm orifice. Figure 18.I can be compared to the importance factors for run 13 plotted in Fig. 15.E, which was run with the same sample temperature history but the sample pan was open. The primary difference in the two runs is that the two diffusion resistances for the blowing agent and surfactant are more pronounced for the 60-μm case than the unconfined open pan run. In Fig 18.I, the importance factor for σ_{E1} shows two distinct regions. Two distinct regions as shown in Fig. 15.I are also shown for unconfined decomposition as well. The two distinct regions occur since the desorption reactions have a significantly lower activation energy than the polymer decomposition reactions (e.g. 28.6 Kcal/mol for reaction 1 vs. 53.7 Kcal/mol for reaction 2). The initial dominance of the parameters associated with reaction 1 result from reaction 1 being the only decomposition mechanism at the lower temperatures. As the temperature increases, the polymer reactions start to dominate and the importance of reaction 1 parameters diminishes.

In Fig. 18.I, the importance factors due to the 2nd and 4th reactions are negligible for the partially-confined run since the OS species are forced to be in equilibrium with the residues for this run. The amount of the OS species that can end up in the residue depends on the orifice diameter as described by eqn (8). The importance factors for reactions 2 and 4 are small since relatively minor species are treated with these reaction steps when compared to the more dominant mixed product species treated by reaction 3.

Figure 19 shows the effect of pressure on the 20ºC/min ramped HPTGA experiments with results for 1, 10, 30, 50, and 70-atms. The experimental data required buoyancy corrections and became noisier with increasing pressure as discussed by Clayton [4]. Although the HPTGA experiments were performed at elevated pressure, the decomposition gases were forced to leave the vicinity of the thermally degrading foam by using a high-pressure purge gas. The average RMS error for the experiments shown in Fig. 19 was 5.67%, which is remarkable since even run-to-run variability between repeated high-pressure experiments was as high as 9%.

Most of the noise in the HPTGA data is related to the buoyancy problems with the HPTGA apparatus. The best way to compare predictions with this noisy data is to compare the mean of the data with the predictions. By comparing Fig. 19.A (data) with Fig. 19.B (SREF predictions), one observes that the mean of the HPTGA data falls within the 95% prediction limit for most of the temperature range. The exception occurs between 25-350ºC, which is the temperature range where all of the OS evolves into the gas-phase for the ambient pressure TGA experiment. In the HPTGA predictions, the OS reaction is inhibited at elevated pressures and OS is assumed to immediately go to its equilibrium value in the residue. This assumption prevents a kinetic evolution of the OS species. The effect of this assumption is similar mass loss profiles in the 225-350ºC-temperature range. This assumption has a minimal impact on the mean predictions since the amount of OS in the overall foam polymer is small.

Figure 20 shows predictions and measurements from all of the isothermal TGA experiments at various pressures and levels of confinement. The thermal history for each of the isothermal TGA experiments was shown previously in Fig. 14. In Fig. 20, plots A through F are for unconfined, ambient pressure isothermal decomposition, where the sample pan did not restrict the decomposition gases from leaving the system. Figures 14.G, 14.H, and 14.K show isothermal TGA runs, where the samples were partially-confined in a hermetically sealed aluminum pan with a 60-μm orifice. Figure 14.I shows a 300ºC isothermal experiment that was run at 10-atm.

The average RMS errors for the unconfined ambient pressure isothermal TGA experiments, the partially-confined ambient pressure isothermal experiments, and the unconfined high pressure isothermal experiments were 4.01, 8.48, and 4.76%, respectively. The higher RMS error for the partially-confined experiments is probably related to the constant d^*/ϕ assumption used in the REF model. Better agreement would have been obtained if d^*/ϕ would increase with the extent of reaction. Importance factors for the 140-300ºC dual isothermal experiment and the 10-atm isothermal experiment are shown in Fig. 20.J and 20.L, respectively. The initial pressure was more influential in the confined isothermal experiment than the pressurized isothermal experiment at 10-atm. However, the importance of the initial pressure becomes more significant as shown previously for the 70-atm ramped experiments in Fig. 19.I.

The SREF model was critically evaluated by comparing the measured and predicted rate of gas generation. Comparing rates of gas evolution is a stringent test of the SREF model since derivatives are extremely sensitive to changes in gas production rates. The plot of experimental gas generation was obtained by taking the negative derivative of the solid fraction. Since the data is somewhat noisy, the data was smoothed prior to taking the derivative. The rate of gas generation predicted by the model was obtained using a central derivative of the calculated solid fraction. The rate of gas generation was shown previously for the 20ºC/min ramped experiment and the 400ºC isothermal experiment in Figs. 14.B and 15.B with an RMS error between the predicted and measured gas generation that was less than a 1%. Figures 21.A, 21.B, and 21.C show the rate of gas generation for the partially-confined ramped experiments with orifices of 2-mm, 350-mm, and 60-mm. The data for both low density and high-density samples are shown in Figs. 21.A-C. The evolution of the blowing agent and surfactant, which is primarily responsible for the initial spike in the gas generation curves, is less pronounced for the high-density foam than for the low-density foam. The SREF predicts that the evolution of the blowing agent and surfactant is suppressed and gives results that are more similar to the experiments performed with high-density foam. Comparing derivative of measured data is an extremely stringent test of the model. Considering the simplicity of the SREF model, the general trends are matched, but quantitative matches of the derivatives could be better with a more sophisticated model that includes reversible reactions.

Figures 21.D, 21.E, and 21.F show gas generation rates for experiments at 1, 10, and 30-atmospheres. All of the HPTGA samples were run with high-density foam. Derivatives of the noisy HPTGA data were obtained by smoothing the data prior to taking the derivative. The initial generation of the blowing agent and surfactant for both the model and experiments were similar. The decrease in the production of the siloxane moiety as pressure increases as modeled by the SREF model is shown to be within the noise of the HPTGA experiments.

The SREF model assumes the shift in the TGA profiles to higher temperatures with increasing levels of confinement for the partially-confined TGA experiments are due to mass transport limitations. The effect of limiting the mass transport rate is to cause the BAS species to evolve into the gas-phase over a wider temperature range than the unconfined decomposition. The mass transport limitation is not as great for the unconfined experiments, even at high pressure as shown in Fig. 21.D-21.F since the decomposition products were swept away from the samples using a purge gas.

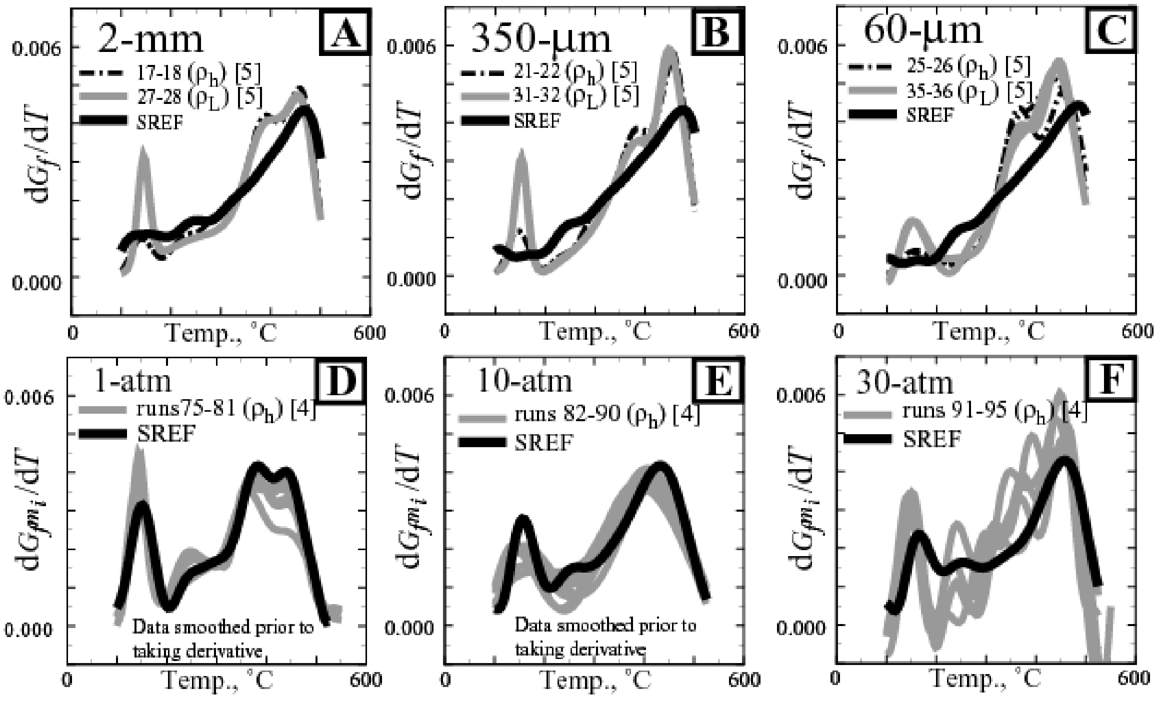

Fig. 21. Predicted and measured [4,5] effect of confinement and system pressure on gas evolution rates for various TGA experiments

9.7 Predicted Trends

Figures 22, 23, and 24 show the effects of heating rate, confinement, and system pressure on the calculated solid fraction, gas generation rate, the solid fraction of the VLE species, the average molecular weight of the condensed phase and average molecular weight of the gas phase. The imposed sample temperature for the runs in Figs 22-24 were obtained from the TGA experiments. The temperatures histories are repeated in Figs. 22.A, 23.A, and 24.A, for each condition.

In Fig. 22.B, the calculated solid fraction profile shifts to higher temperatures with increasing heating rates. The magnitude that each curve shifts to higher temperature is related to the reaction rates. Thermal decomposition is a temperature dependent kinetic process. If the reaction rates were faster, the profiles depicted in Fig 22.B would be grouped closer together. If the reaction rates were slower the profiles would be broadened. All of the remaining predictions in Figs. 22.C-22.F shift to higher temperatures similar to the solid fraction profiles.

In Fig. 22.E, the average molecular weight of the condensed phase is shown to change from 3500 g/mol to 1000 g/mol. The 3500 g/mol is average molecular weight of the XL-mer molecular weight, which was assumed to be 4000 g/mol, and the molecular weight of the C-residue, which was assumed to be 1000 g/mol. The average molecular weight of the gases changes from 120 g/mol, which is the assumed molecular weight of blowing agent and surfactant, to 150 g/mol.

Figure 23 shows the effect of confining the decomposition gases. Similar to the heating rate effect, the TGA profiles shift to higher temperatures as the orifice diameter changes from a 4-mm diameter open pan to a covered pan with a 60-μm orifice in the cover. The effect is predicted by changing the value of the diffusion parameters, d^*/ϕ, and by having part of the L_2 population change immediately to the OS-residue. In Fig. 23.C, the initial gas production depicted as the initial peak in the gas generation plot, decreases with increasing levels of confinement. The release of the blowing agent and surfactant are essentially inhibited by the smaller orifice sizes associated with increasing levels of confinement. The production of OS in the gas-phase also decreases with increasing levels of confinement.

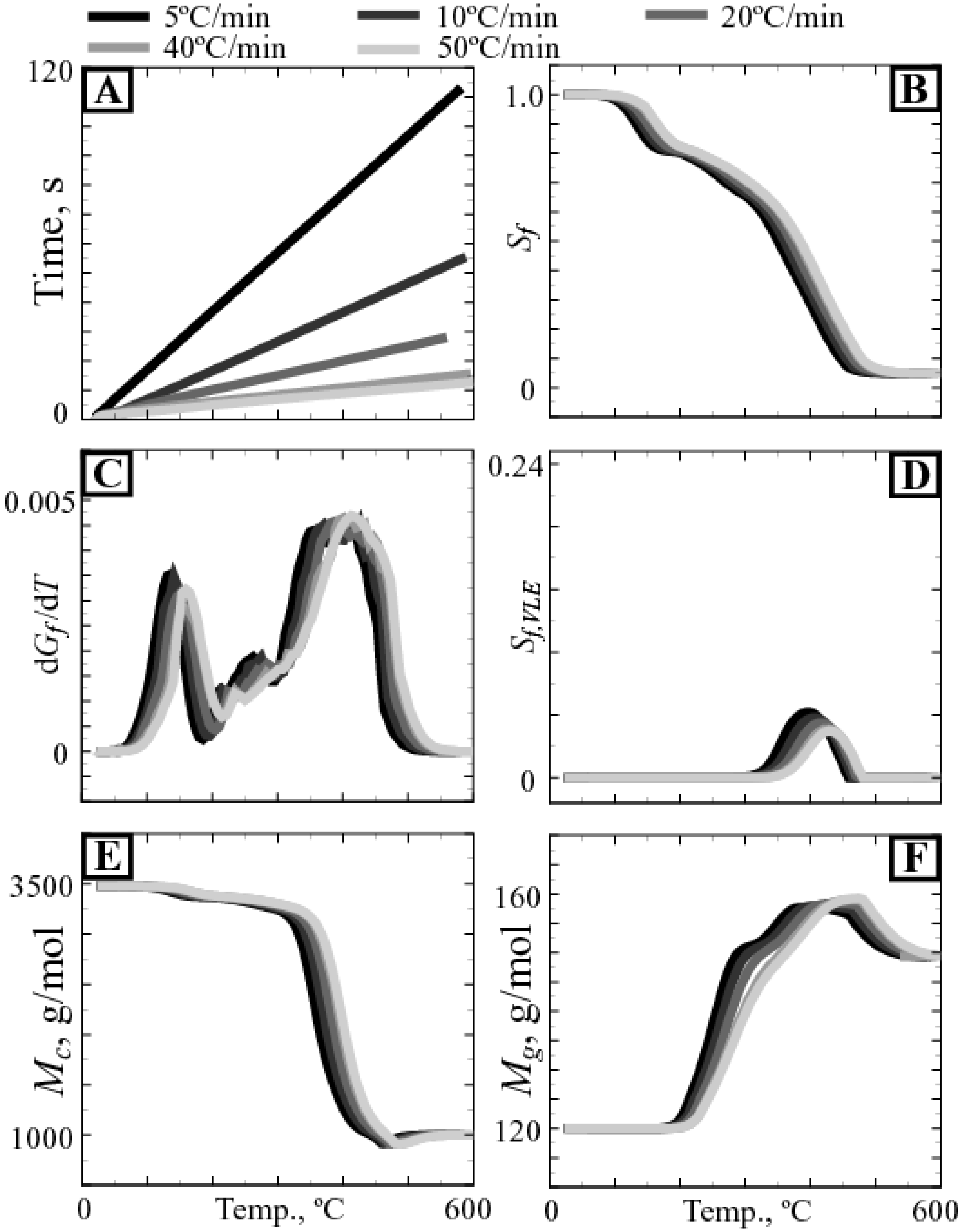

Fig. 22. Predicted effect of heating rate on B) solid fraction, C) rate of gas evolution, D) solid fraction of the VLE species as determined using eqn (75), E) average molecular weight of the condensed-phase, and F) average molecular weight of the gas-phase. The temperature history is given in A

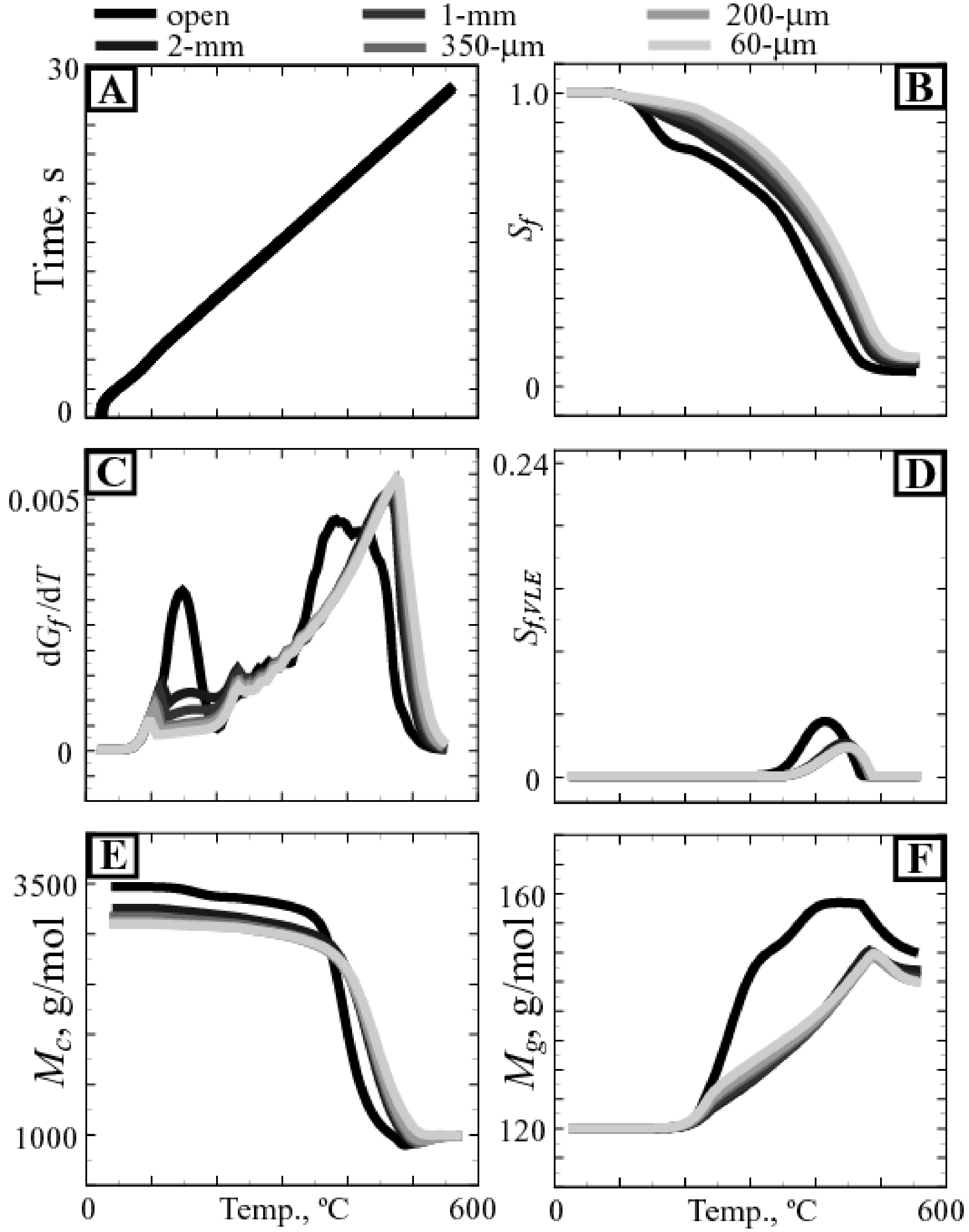

Fig. 23. Predicted effect of confinement on B) solid fraction, C) rate of gas evolution, D) solid fraction of the VLE species as determined using eqn (75), E) average molecular weight of the condensed-phase, and F) average molecular weight of the gas-phase. The temperature history is given in A

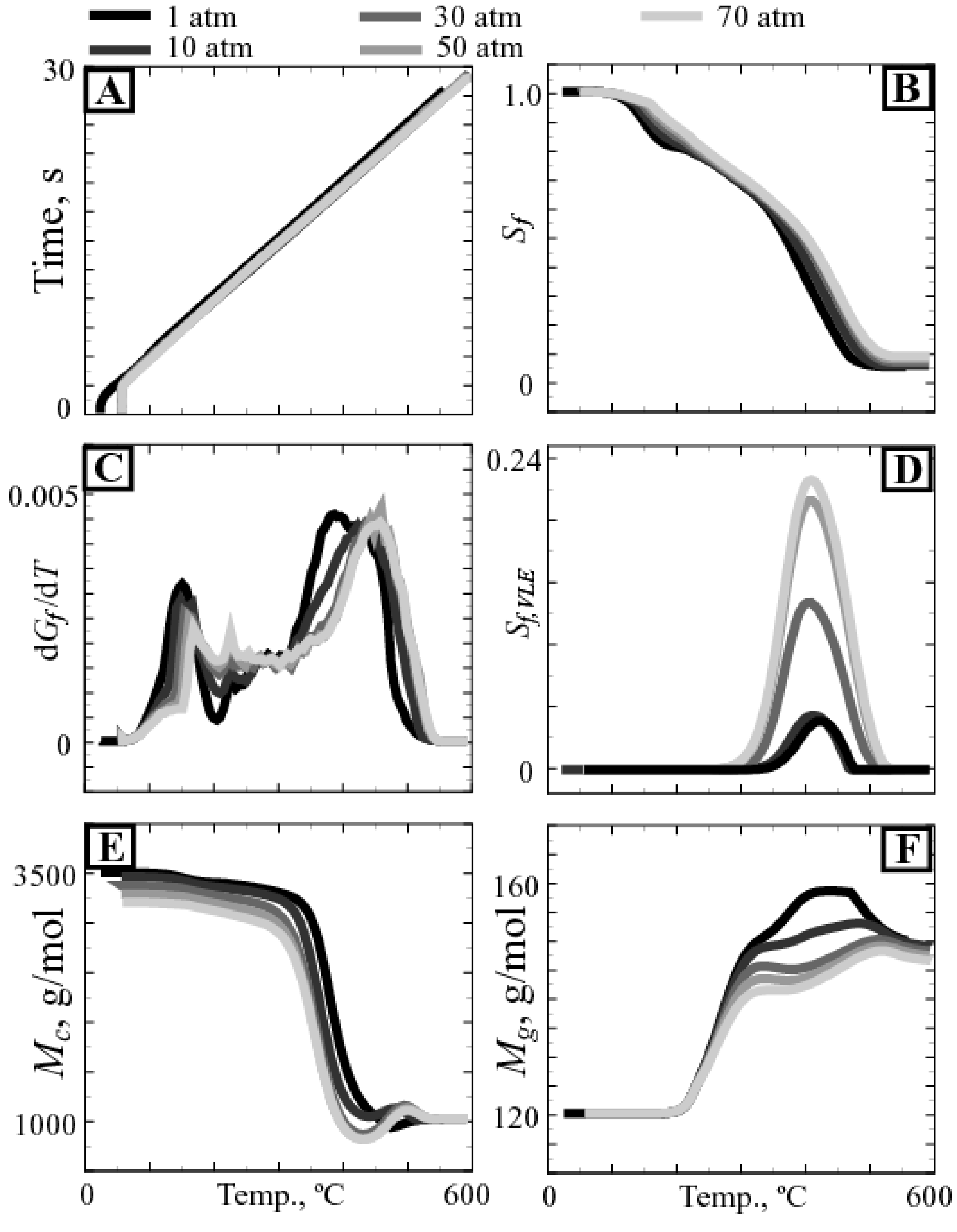

Fig. 24. Predicted effect of pressure on B) solid fraction, C) rate of gas evolution, D) solid fraction of the VLE species as determined using eqn (75), E) average molecular weight of the condensed-phase, and F) average molecular weight of the gas-phase. The temperature history is given in A.

Figures 21.A-21.C shows a decrease in the rate of OS production as the orifice diameter is decreased, especially for the low-density data. The effect is not as dramatic for the high-density data and the SREF predictions behave more like the high-density data, which is expected to have greater resistance to mass transport. Comparing derivative of measure data is an extremely stringent test of the model. Considering the simplicity of the SREF model, the general trends are matched, but quantitative matches of the derivatives, especially with different sample densities, could be better with a more sophisticated model.

In Fig. 23.E, the initial condensed-phase molecular weight is not the same for each of the confinement runs. The SREF assumption is that the OS-residue is immediately formed at the beginning of the run and is not determined kinetically. This assumption is responsible for different values of the initial molecular weight of the condensed phase, which is composed of XL-mer, C-residue, and OS-residue. Only the predicted OS-residue is a function of the confinement. The restriction on gases leaving the TGA system causes the average molecular weight to be significantly different for the open pan case when compared to the cases where the gases are restricted. The average molecular weight at the end of each reaction is slightly different since some of the initial L_2 bridge ends up in the condensed-phase rather than the gas-phase.

The effects of pressure on decomposition are shown in Fig. 24. The effect of elevated pressure is similar to the effects of confinement at ambient pressure in that the TGA profiles shift to higher temperatures. The thermoequilibrium remains unchanged for the ambient pressure confined experiments; while the mass transfer resistance is impacted. At elevated pressure, the production of blowing agent and surfactant does not decrease as much as in the confined TGA runs. This is shown in Fig. 24.C where the initial peak is still prevalent as pressure is increased. In contrast, the initial peak in Fig. 23.C decreases substantially as the decomposition gases are restricted. Such observations show that confinement effects are different than pressure effects. In the HPTGA experiments, the gases were not confined to be near the decomposing sample surface, and were swept out of the reaction chamber by a high-pressure gas.

Another difference between the effects of confinement and pressurization is in the amount of condensed VLE gases. For the low pressure, partially-confined TGA experiments, the amount of condensed-phase VLE species, described as the VLE solid fraction, was significantly less than for the higher pressure TGA runs. As pressure increases, higher vapor pressures are needed for the VLE species to be in the gas phase, and the amount of condensed VLE species increases with pressure. The effect of pressure on the condensed and gas-phase molecular weights is similar to the effects of confinement.

9.8 REF200 and REF300 experiments and predictions

The SREF model predictions and data shown in Sections 9.1-9.7 were for REF100 [3]. However, the formulation for the REF foam has changed in order to increase the glass transition temperature to be well above normal design operating temperatures. Two additional formulations, referred to as REF200 and REF300, differ primarily in the amount of blowing and curing agents used in the synthesis. The SREF model was developed with the intent to be applicable to other formulations provided the polymer is not altered significantly. Decomposition of REF200 and REF300 has been predicted using the SREF model without changing the kinetic coefficients. The only differences in the decomposition model parameters are in the initial constituents making up the polymeric foam, in particular, the initial population of the "sorbed" species and the population of the bridges composed of the mixed product gases. The initial conditions for the REF100, REF200, and REF300 were given previously in Table 3. Two 20ºC/min LPTGA experiments (runs 134 and 35 in Table 10) were performed with REF200. Two 20ºC/min LPTGA experiments (runs 136 and 137 in Table 10) were also performed with REF300.

Figure 25 shows comparisons between the predicted and measured solid fractions for REF200 and REF300 samples heated at 20ºC/min in the LPTGA apparatus. The experimental data for REF100, REF200, and REF300 at similar conditions is shown in Fig. 25.A to show the differences in these distinctly different samples. The initial densities of the samples were 0.13 g/cm^3 (8 lb/ft^3). The samples were ground into powders. Figures 25.B and 25.C show a comparison between the SREF predictions and LPTGA data, respectively. The average RMS errors for the REF200 and REF 300 were 1.1% and 2.3%, respectively. These RMS errors are consistent with the RMS errors for the REF100 series foam. The SREF model can approximate thermal decomposition of REF100, REF200, and REF300 foam encapsulants.

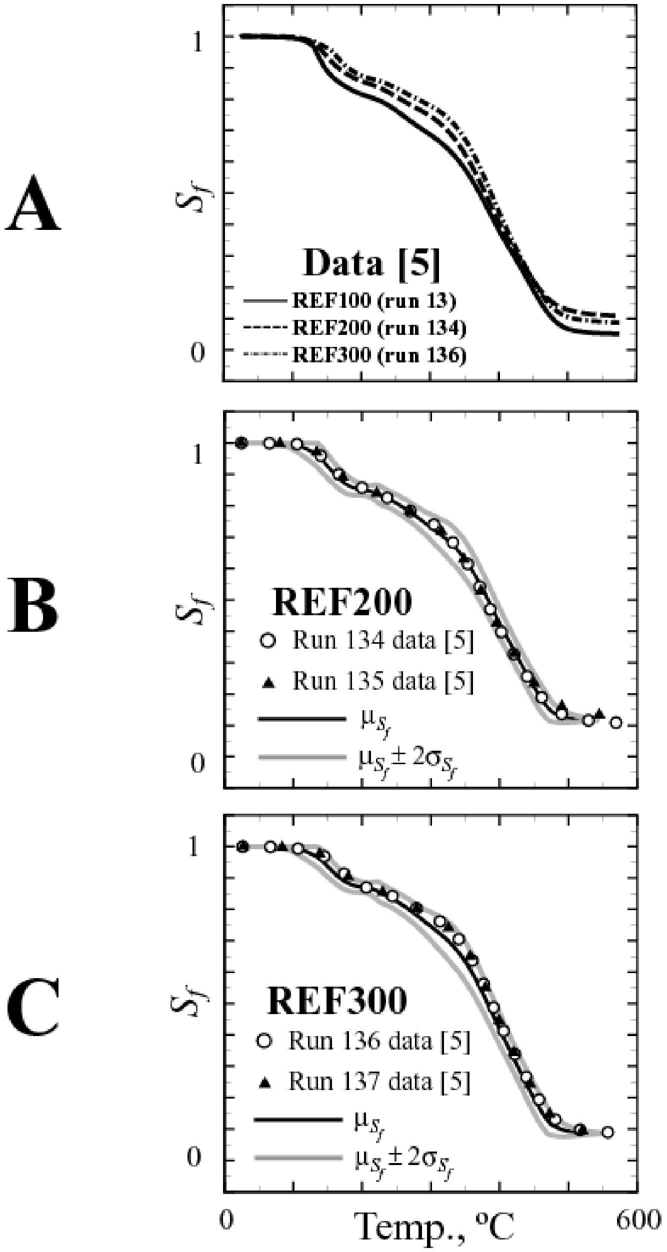

Fig. 25. A) Measured [5] solid fraction for REF100, REF200, and REF300. Predicted (lines) and measured (symbols) [5] solid fraction for B) REF200 and C) REF300.

10. Hot Cell Experiments and Predictions

The hot cell experiment was originally designed to characterize the damage state of thermally degraded energetic materials [33]. The hot cell apparatus, shown in Fig. 26.A, consists of a pneumatic cylinder that can be controlled by either the load cell or the displacement gauge. In the current report, the load cell was used to maintain a constant volume decomposition chamber by confining the ends of a cylindrical foam sample between two pistons with the lateral surface of the foam being confined by a solid cylinder of stainless steel. The initial dimensions of the cylindrical foam sample were 1.257 cm diameter by 0.663 cm high. A gas-tight seal was maintained using O-rings on the pistons. Decomposition gases caused the pressure within the constant volume chamber to increase, which required a larger load to maintain the constant volume decomposition chamber. The pressure was determined by dividing the measured load by the cross sectional area of the pistons. Renlund et al. [33] gives additional information regarding the hot cell experiment.

10.1 Observations

Three thermocouples are shown in the schematic in Fig. 26.A. The center thermocouple (shown as a gray line) was inserted through the upper piston and located close to the foam sample. The other two thermocouples were located in the solid stainless steel cylinder referred to as the hot cell. The temperature recorded with the sample thermocouple was shown previously in Fig. 14.F. All three thermocouple readings are shown in Fig. 26.B along with the pressure determined from the force measured by the load cell divided by the cross-sectional area of the pistons. The displacement measurement is also shown in Fig. 26.B. The sample was initially heated from room temperature to 39ºC and held for about 10 minutes to stabilize the hot cell instrumentation. The sample was then heated at 6-7ºC/min to 300ºC and held for an additional 60 minutes. The hot cell heaters were then turned off and the sample was allowed to cool as shown in Fig. 26.B.

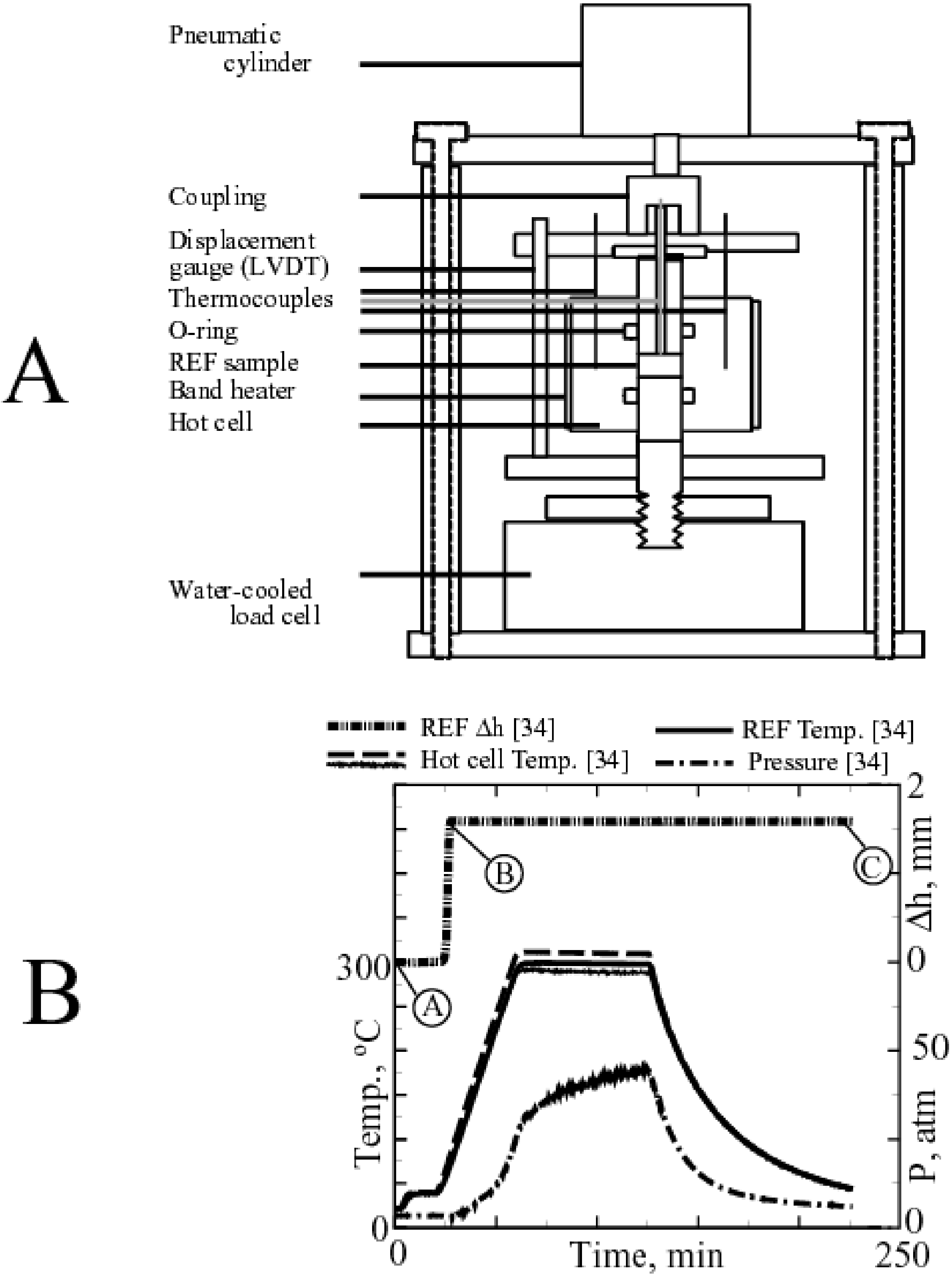

Fig. 26. A) Schematic of hot cell apparatus and B) measured [34] REF sample displacement, temperatures, and pressure. In the plot, A, B, and C represent the sample state before being squish, after being squish, and at the end of the experiment, respectively (see Table 13).

Figure 26.B show the absolute value of the displacement measured with the LVDT as Δh, which refers to the change in height of the foam sample in mm. In Fig. 26.B, the measured displacement has three states marked with an A, B, and C. In the plot, A, B, and C represent the state of the sample before being "squished", after being "squished", and at the end of the experiment, respectively. The term "squished" refers to deformation of the sample by shortening the height of the sample and increasing the width of the sample. These three states are described in Table 13. As the sample temperature reached the glass transition temperature (70ºC), the sample height decreased and width increased. In other words, the sample deformed (squished) at the glass transition temperature with an initial load of 3.39 atm. The density of the foam at point B, after being deformed, was 0.312 g/cm^3 as given in Table 14. From point B on, the decomposition chamber volume was controlled by the displacement gauge and set to be constant with a height of 0.504 cm and a diameter of 1.27 cm.

Table 13. Three foam states in hot cell experiment [34] (see Fig. 26.B)

Description	Symbol	A) Before squish	B) After squish	C) Postmortem
Foam mass	m^{foam}	0.1993 g	0.1993 g	0.131 g
Solid fraction	S_f	1	1	0.657
Height of chamber	h^c	0.663 cm	0.504 cm	0.504 cm
Diameter of chamber	d^c	1.27 cm	1.27 cm	1.27 cm
Height of foam sample	h^{foam}	0.663 cm	0.504 cm	0.095 cm
Diameter of foam sample	d^{foam}	1.257 cm	1.27 cm	1.27 cm
Volume of foam sample	V^{foam}	0.823 cm^3	0.638 cm^3	0.120 cm^3
Density of foam sample	m^{foam}/V^{foam}	0.242 g/cm^3	0.312 g/cm^3	1.09 g/cm^3

Table 14. Pressurization parameters for the hot cell [34]

Description	Symbol	Value
Initial Pressure	P^o	3.39 atm
Initial Temperature	T^o	71ºC
Initial foam density	ρ^o_f	0.312 g/cm^3
Initial polymer density	ρ^o_p	1.09 g/cm^3
Element volume	Ve	0.638 cm^3
Initial gas volume	V^o_g	0.455 cm^3
Initial gas moles	n^o	5.46×10^{-5} moles

For the 20ºC/min ramped unconfined TGA experiment shown previously in Fig. 3.B, gas-phase decomposition products were apparent when the sample temperature reached 100ºC. For the fully-confined decomposition within the hot cell apparatus, evidence of gas-phase products is also evident when the sample temperature was about 100ºC. For example, the load required to maintain a decomposition chamber height of 0.504-cm started to increase in a *concave* fashion as shown in Fig. 26.B. The shape of the load history was *convex* when the sample temperature was held constant at 300ºC between 65 and 126 minutes. At 126 minutes, the sample heaters were turned off, and the load decreased in a *concave* manner.

Postpartum measurements of the hot cell sample are given in Table 14. The postpartum sample looked like a solid plastic wafer without bubbles after removal from the hot cell. The final mass of the sample was 0.131 g giving a final solid fraction of 0.657. The height of the postpartum foam sample was 0.095 cm and the diameter was 1.27 cm giving a foam density of 1.09 g/cm^3. This is close to the density of the foam polymer (plastic without bubbles) as measured by Gembarovic and Taylor [32]. These results suggest that over the course of the hot cell experiment, the initial structure of the foam disappeared probably by liquefaction causing the gas volume to be separate from the polymer volume.

Pressurization of the hot cell decomposition chamber was determined from the initial pressure, the initial gas volume, the additional gas volume created by conversion of the REF polymer to gases, the initial gas moles, the additional gas moles generated by the decomposition reactions, the initial temperature, and the dynamic temperature. The initial pressure listed in Table 14 was determined by dividing the initial load by the cross-sectional area of the pistons. The gas volumes were determined using eqns (98) and (99); the moles of gas were determined using eqns (100) and (101); and the temperatures were measured. The increase in pressure within the decomposition chamber depends on the amount of decomposed foam and the molecular weight of the decomposition gases within the decomposition chamber.

The shape and magnitude of the measured hot cell load was reasonable, however, the hot cell seemed to unload faster than anticipated. Even though the thermocouple used to measure the sample temperature was decreasing rapidly, the load decreased at the same rate. The piston cools using active cooling. The load cell is cooled using chilled water. Thus, as the temperature decreases a large thermal gradient exists in the confining pistons and probably within the sample. This may lead to uncertainty in the measurement. Also, the SREF model does not consider reverse reactions, which are prevalent as the sample temperature drops leading to disagreement in the cool down phase of the experiment.

10.2 Predictions

Pressurization parameters used to model the hot cell experiment are given in Table 14. For the SREF model, the initial state of the sample is taken to be state B in Fig. 26.B. Figure 27 shows the measured and predicted pressure within the hot cell apparatus. The measured pressure was determined by dividing the measured load by the piston cross-sectional area. The pressure was calculated using eqn (94). The percent relative RMS error between the measured and predicted pressure was determined as follows:

$$\%\,\text{relative RMS error} = \frac{100\sqrt{\sum_{i=1}^{n}\left[\left(P^{\text{Hot Cell}} - P^{\text{SREF}}\right)\big/P^{\text{Hot Cell}}\right]^2}}{n}\,. \tag{118}$$

The relative RMS error for the hot cell simulation in Fig. 27 was 6.3%, where most of the error is in the unloading region after 125 minutes. The relative RMS error, during the loading phase of the experiment from 1 to about 125 minutes, was 0.3%. The relative error, during the unloading phase of the experiment for times greater than 125 minutes, was 12.6%. The greater RMS error associated with the unloading region may be caused by problems in measuring the sample temperature accurately and reversible reactions as discussed in the previous section.

Figure 27 also shows the 95% uncertainty interval for the predicted hot cell pressure. The factors primarily responsible for this uncertainty interval have high “importance” factors that are shown in Fig. 27.B. In Fig. 27 B, the parameters contributing to the uncertainty in the first 60 minutes of the hot cell during the initial temperature ramp are the initial pressure, the foam density, and the desorption kinetics associated with reaction 1. The most sensitive parameters during the isothermal period are the initial foam density and the chemistry parameters associated with the mixed products and bisphenol A. During the unloading phase of the experiment, the foam density and the activity coefficient parameter for reaction 1, γ_1, becomes significant.

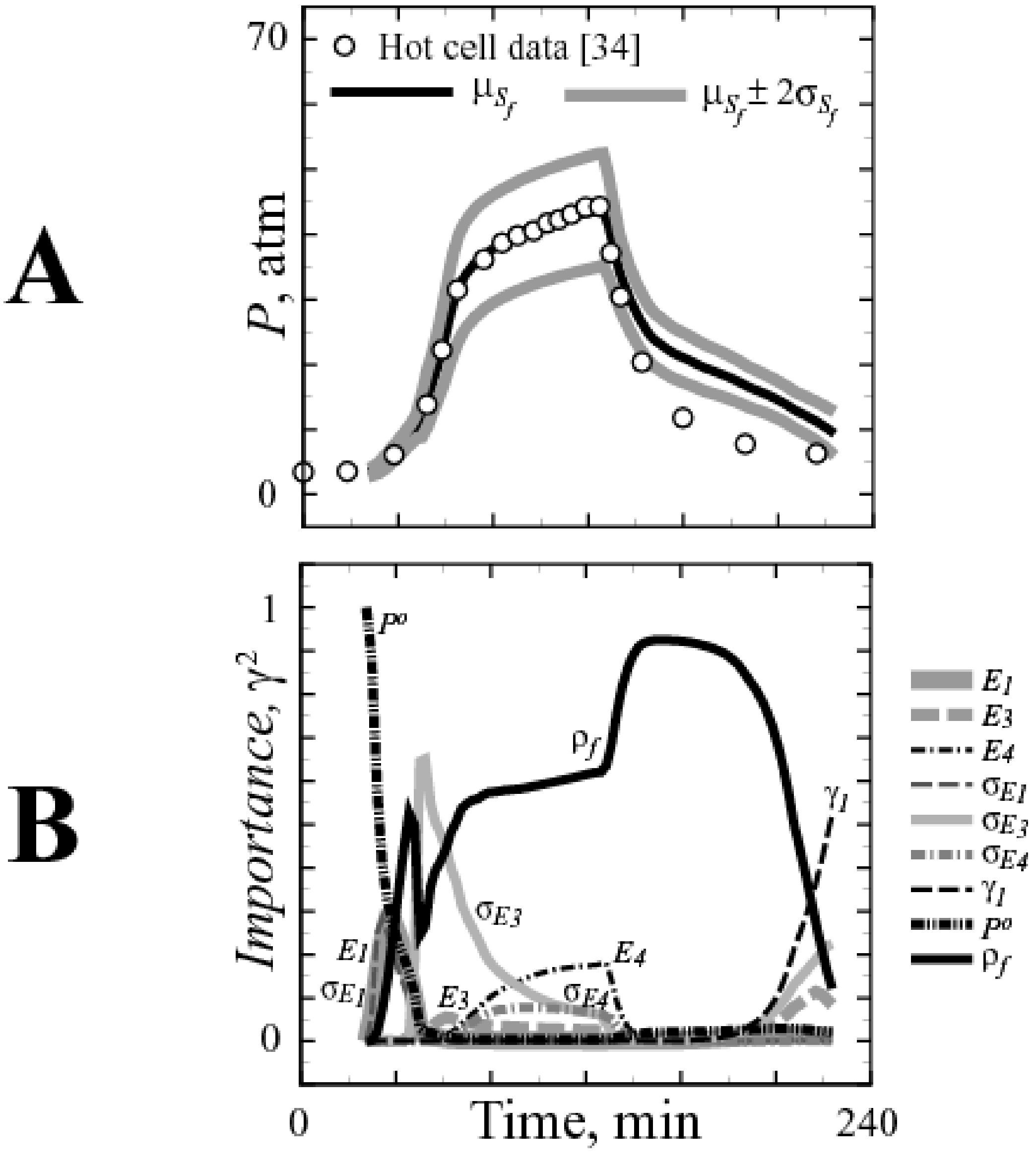

Fig. 27. A) Predicted (lines) and measured (open circles) [34] pressure in the hot cell experiment. B) Importance factors that contribute to the 95% prediction interval ($\mu_{Sf} \pm 2\sigma_{Sf}$) in plot A.

Figures 28 and 29 show sixteen predictions of the hot cell experiment. The plots in Fig. 28 show: A) pressure, B) gas-phase mass fractions and gas fraction, C) gas-phase molecular weight, D) rate of gas species evolution, E) gas volume, F) gas-phase VLE species mole fractions (see eqn 67), G) gas moles in hot cell decomposition chamber, and H) condensed-phase VLE species mole fractions (see eqn 66). The plots in Fig. 29 A) solid fraction, B) populations, C) VLE solid fraction, D) condensed mass fractions, E) average condensed-phase molecular weight, F) ratio of the moles vapor (V) to the moles of combined-phase (F), G) viscosity, and H) K-values.

Figure 28.B shows the prominent gas mass fractions (and overall gas fraction) in the decomposition chamber of the hot cell. The time derivative of the gas mass fractions and the rate of gas evolution are shown in Fig. 28.B. The mole fraction of the VLE gas-phase species is shown in Figure 28.F and correspond to the mass fractions shown in Fig. 28.B. The average gas-phase molecular weight is shown in Fig. 28.C. The average gas molecular weight is between 120 and 140 g/mol. Only three of the seven VLE species are predicted in significant quantities in the gas-phase: BAS, OS, and MP, with the remaining VLE species are in the condensed-phase. Figures 28.F and 28.H show the gas-phase [eqns (70)] and condensed-phase [eqns (69)] mole fractions of the VLE-species, respectively.

The large RMS error during the unloading phase of the experiments is troublesome. The experimental apparatus may have more uncertainty in the unloading-phase than in the initial loading phase due to active cooling as discussed previously. However, this experimental uncertainty is not expected to account for the large RMS error after 140 minutes. The error may be caused by the forward Diels Alder reaction, which is not included in the SREF mechanism. The discrepancy between the SREF model and the hot cell data occurs at approximately 140 minutes. The temperature of the sample at 140 minutes is 200ºC as shown and drops to 100ºC at 170 minutes. The Diels Alder reaction may be significant in the totally confined system.

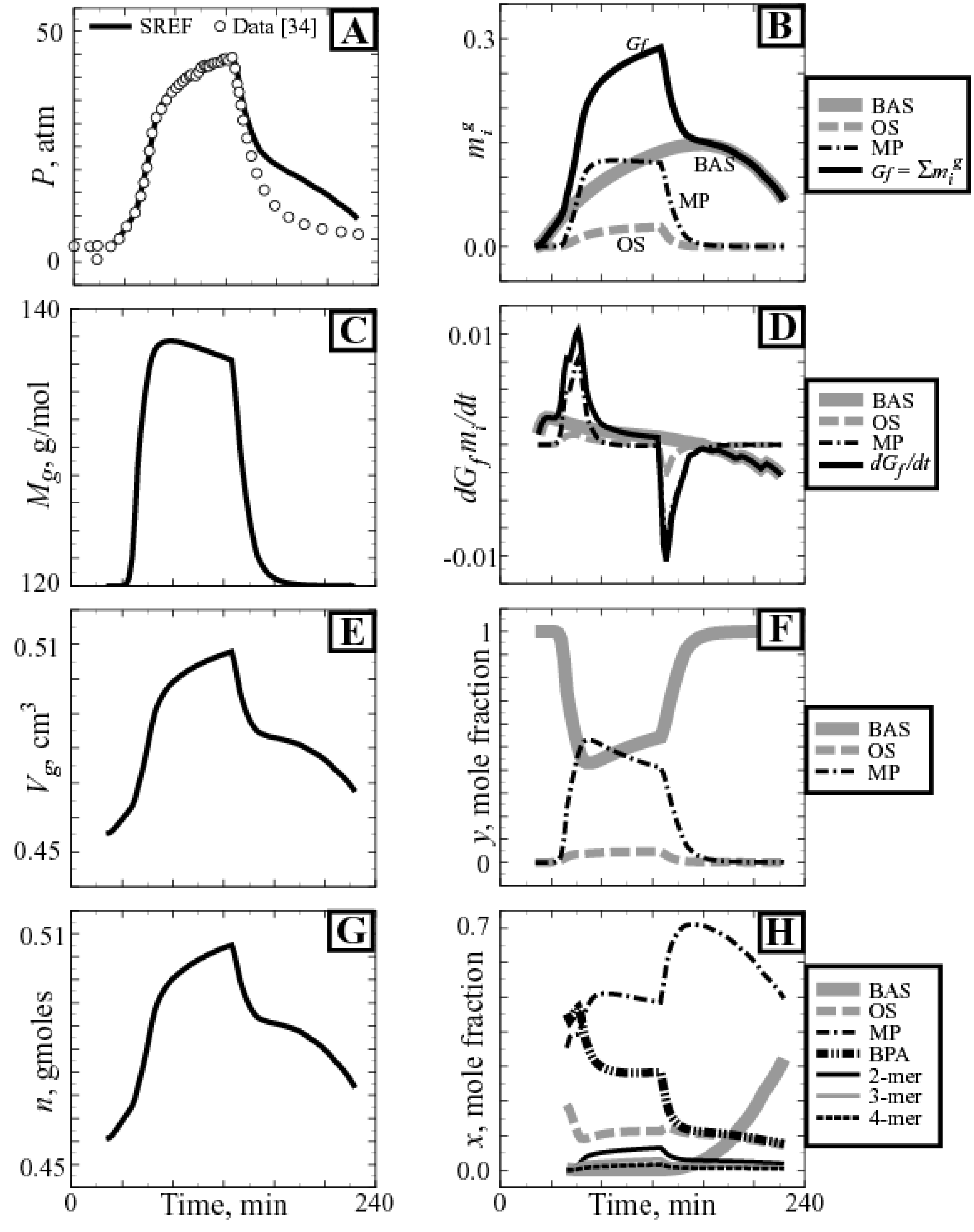

Fig. 28. Hot cell predictions: A) pressure, B) gas-phase mass fractions and gas fraction, C) gas-phase molecular weight, D) rate of gas species evolution, E) gas volume, F) gas-phase VLE species mole fractions [see eqn (70)], G) gas moles in hot cell decomposition chamber, and H) condensed-phase VLE species mole fractions [see eqn (69)]. Plot A also shows the measured pressure from [34].

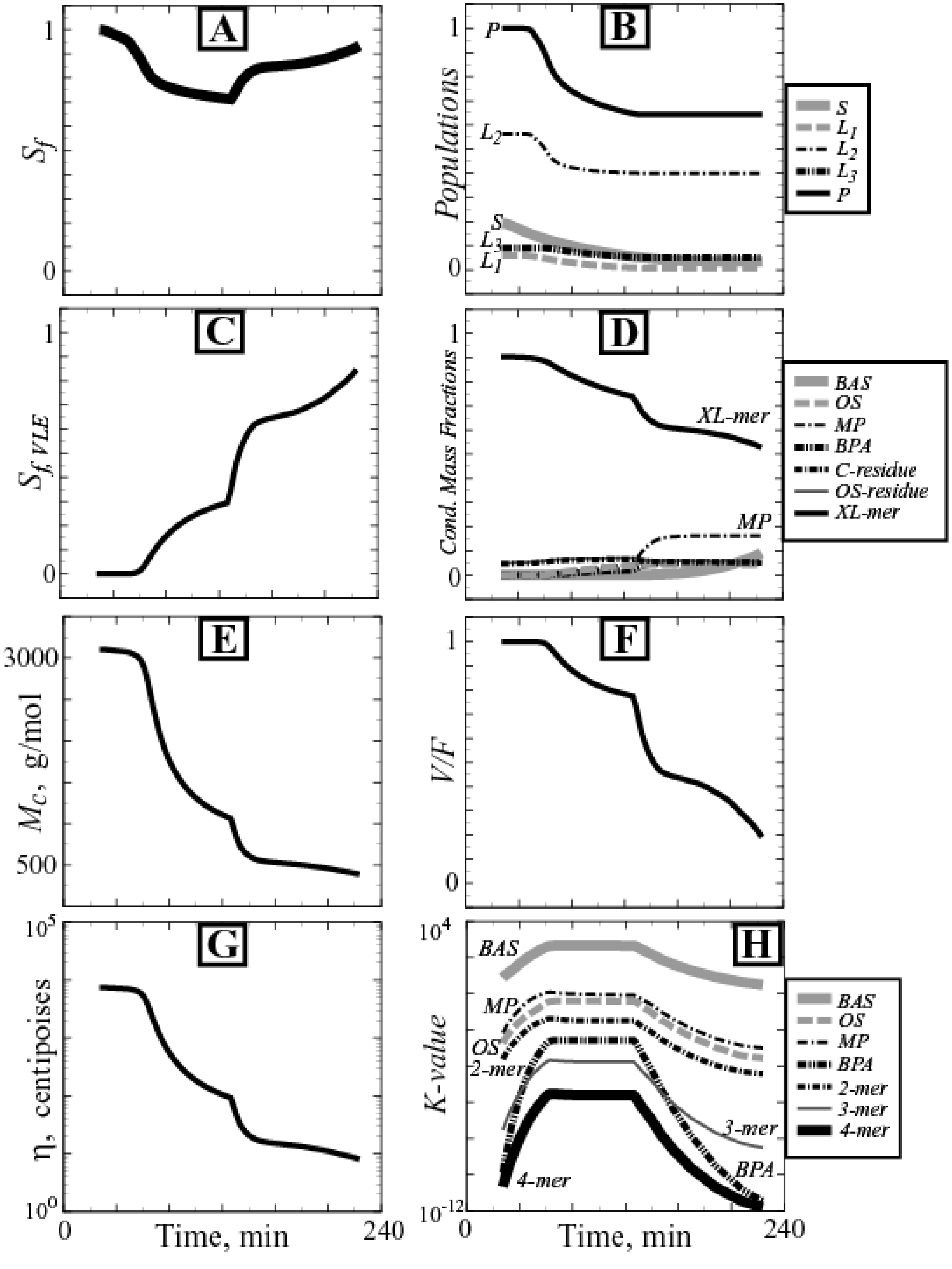

Fig. 29. Hot cell predictions: A) solid fraction, B) populations, C) VLE solid fraction, D) condensed mass fractions, E) average condensed-phase molecular weight, F) ratio of the moles vapor (*V*) to the moles of combined-phase (*F*), G) viscosity, and H) *K*-values.

In Fig. 29.A, the solid fraction is shown to decrease until the hot cell heaters are turned off. As the hot cell cools, VLE gases condense and the solid fraction increases. The postmortem solid fraction was 0.657 as shown in Table 13. The measured postmortem solid fraction is similar to the minimum predicted solid fraction in Fig. 29. The measured solid fraction is expected to be low if not all of the sample residue was retrieved during the postmortem analysis.

Figure 29.C shows the solid fraction of the VLE species. As the pressure increases, the VLE solid fraction increases due to pressure induced condensation of the VLE gases, since temperature is relatively constant. As the hot cell cools, more VLE species condense due to cooler temperatures. A similar trend can be observed in Fig. 29.F, which shows the moles of VLE vapor divided by the moles of combined-phase VLE species.

Figure 29.D shows that the condensed-phase is composed primarily of the XL-mer population and the mixed products, MP. The condensed-phase molecular weight is initially about 3200 g/mol and near the end of the isothermal period starts to plateau to a value of 1000-g/mol, which is the molecular weight of the C-residue and OS-residue. As the sample temperature drops, some of the VLE species condense as shown by a drop in the moles of gas and a decrease in the V/F ratio. The condensed-phase molecular weight decreases as the amount of condensed-phase VLE species increase.

Figure 29.H shown the K-values for the seven VLE species. The species with higher K-values are more likely to be in the gas-phase. In fact, the SREF model predicts that only the species with high K-values end up in the gas-phase. Only BAS, OS, and MP were predicted to be in the gas-phase of the hot cell decomposition chamber.

11. Summary and Conclusions

A model based upon the chemical structure of rigid, closed-cell removable epoxy foam has been presented. The chemical structure of the foam polymer was determined from synthesis details by assuming a reactivity hierarchy of various functional groups. The foam is composed of an epoxy polymer, absorbed/adsorbed blowing agents, and absorbed/adsorbed surfactants. The absorbed/adsorbed species are simply referred to as “sorbed” species. The model is called a simple removable epoxy foam (SREF) decomposition chemistry model. The term “simple” refers to the lattice model used to describe degradation of the epoxy polymer, which has been simplified considerably when compared to other lattice statistics models published in the literature. The simplification involves use of a lattice structure with massless sites (sites without mass) connected by bridges that contain the polymer mass. Three nonreversible reactions describe the degradation of the polymer. A separate reaction describes desorption of the blowing agent and surfactant.

The model lattice was composed of sites connected by octamethylcylotetrasiloxane (OS) bridges, mixed product (MP) bridges, and bisphenol-A (BPA) bridges. The mixed products were treated as a single species, but are likely composed of phenols, cresols, and furan-type products. The SREF model considers eleven (11) species that can be separated into two categories—1) seven VLE species and 2) four non-VLE species. The VLE species can reside in either the condensed-phase, the gas-phase, or in both phases as determined using a vapor-liquid equilibrium model using pressure dependent activity coefficients. The non-VLE species always remain in the condensed-phase. The VLE species include BAS, OS, MP, BPA, 2-mers, 3-mers, and 4-mers; representing the blowing agent and surfactant as a single species, octamethylcylotetrasiloxane, mixed-products, bisphenol-A, and polymer fragments that contain two, three, or four sites, respectively. The four non-VLE species have large molecular weights with low vapor pressures. These species include C-residue, OS-residue, L-mers, and XL-mers; representing a carbon residue, a residue with the same composition as OS, a residue composed of polymer fragments from 5-mers to nmax-mers, and a residue composed of nmax+1-mers to the ∞-mer, which is the infinite matrix. The value of nmax is specified by the user to be no more than 500. The user specifies the molecular weight of the C-residue, OS-residue, and XL-mer residue.

Although the SREF model considers 11 species, the reaction mechanism consists of four first order nonreversible reactions. The initial reaction describes desorption of the blowing agent and surfactant. The remaining three reactions describe the thermal degradation of the polymeric foam describing decomposition of bridges composed of octamethylcylotetrasiloxane, mixed products, and bisphenol-A. The reaction mechanism uses a mass-fraction progress variable approach where the mass fractions of various species are tracked. The reaction mechanism also considers distributed activation energies where the activation energies are distributed normally based on the extent of reaction. For the desorption reaction, the distributed activation energy is based on the extent of the desorption reaction. For the remaining polymer bridge breaking reaction, the distributed activation energy is based on the extent of the polymer bridge populations. The kinetic parameters were obtained using two TGA experiments. Parameters for the desorption reaction were obtained from a 140ºC isothermal experiment. At 140ºC, the polymer degradation reactions are negligible. The kinetics for the polymeric bridge breaking reactions were obtained from a nonisothermal TGA experiment where the sample temperature was ramped at 20ºC/min from room temperature to about 575ºC.

The SREF model also considers mass transport effects using effective mass transport properties. The ratio of the effective diffusion length normalized by the effective tortuosity was assumed to be constant throughout the reaction. The values for these diffusion parameters were obtained using partially-confined TGA data where the decomposition gases were restricted by using hermetically sealed sample pans with various sizes of orifices ranging from 2-mm to 60-μm in diameter. The amount of residue was also modeled by assuming that the residue yield was equal to the equilibrium values.

Pressure effects were included in the SREF model by solving the Rachford-Rice vapor-liquid equilibrium model with pressure dependent activity coefficients. The vapor pressures for the VLE species were obtained from the literature. The mixed product species vapor pressure was assumed to be the vapor pressure of phenol. The vapor pressures of the polymer fragments were determined from a molecular weight correlation. The VLE model was solved simultaneously with the kinetic equations, mass transport equations, and polymer lattice statistics. The SREF model can approximate quantities such as the solid fraction, gas fraction, gas-phase mass fractions, condensed-phase mass fractions, the average gas-phase molecular weight, the average condensed-phase molecular weight, the number of gas moles produced, the volume of gas produced, the pressure (considering the decomposition products are confined), the rate of gas evolution, and the viscosity of the condensed-phase. The viscosity of the condensed-phase was determined using a simple molecular weight model proposed by Flory [26]. A reaction enthalpy model based on DSC data was also presented.

Percolation theory was used to solve for the polymer lattice statistics. As the sample temperature increased, the polymer bridge population was calculated using the decomposition mechanism. The bridge population was used to determine the distribution of various polymer fragment mass fractions. The SREF model uses a Bethe lattice with a coordination number of three. The lattice statistics model was also used to determine the molecular weight distribution of the various polymer fragments.

The SREF chemistry model was tested with a large set of TGA experiments. 133 out of 137 TGA experiments were performed using SREF100, which is the initial formulation patented by Loy et al [1]. Two of the 137 TGA experiments were performed with a REF200, and two TGA experiments were performed using REF300 samples. These two REF encapsulants, referred to as REF200 and REF300, have glass transition temperatures higher than REF100. The additional formulations were developed to increase the glass transition temperature to be well above operational temperatures. The SREF model was also used to simulate experiments performed with REF200 and REF300 series foam by changing the initial constituent composition. All of the remaining parameters, including the kinetic coefficients, were not changed for the REF200 and REF300, simulations.

The REF100 TGA experiments were classified into three categories: 1) unconfined ambient pressure experiments, 2) partially-confined ambient pressure experiments, and 3) unconfined high-pressure experiments. The unconfined experiments were performed with open sample pan. The partially-confined experiments were performed in covered sample pans with orifice diameters ranging from 2-mm to 60-μm. The high-pressure experiments were performed in a high pressure reactor with a high pressure purge gas. Thus the high-pressure experiments are considered unconfined since the decomposition gases were swept from the surface of the decomposing material using a high-pressure purge gas.

The primary effects for confinement and pressure are similar. The TGA mass loss profiles shift to higher temperatures as the decomposition products are confined. Likewise, the TGA mass loss profiles shifted to higher temperatures as the reaction chamber pressure increased. The shift with confinement was predicted in the SREF model using the mass transport model using an effective diffusion length. For example, the effective diffusion length was assumed to increase with confinement, which caused the profiles to shift to higher temperatures. The vapor-liquid equilibrium model caused the shift in the predicted profiles with pressure. As pressure increased, smaller fragments with higher vapor pressures were required for significant vaporization. These smaller polymer fragments were created kinetically at higher temperatures, thus causing the mass loss profiles to shift to higher temperatures with increasing chamber pressure.

The average percent RMS errors for the three categories of REF100 TGA experiments; unconfined ambient pressure, partially-confined ambient pressure, and unconfined high pressure; were 1.9%, 5.0%, and 5.5%. The SREF model was also used with a mean value technique to estimate a 95% prediction interval, which are the mean solid fraction prediction ±2 standard deviations of the predicted solid fraction. Most of the ambient pressure TGA data were within the 95% prediction interval. For the high-pressure TGA data, noise created by buoyancy problems caused problems in comparing the predictions with measurements. However, the mean of the HPTGA data was usually within the 95% prediction interval. For the REF200 and REF300 simulations, the RMS error was 1.1% and 2.3%, respectively. The REF200 and REF300 data were also within the 95% prediction interval. The low RMS errors for REF100, REF200, and REF300 predictions suggest that the SREF model with one set of parameters can be used to describe decomposition of a variety of epoxy foam encapsulants by specifying the initial constituent composition. The only difference between the 3 types of epoxy foam (REF100, REF200, and REF300) was the initial amount of blowing agent, surfactant, and curing agents.

As a final test of the SREF model, a hot cell experiment was simulated to predict dynamic pressurization of a sample that was fully-confined. The decomposition gases were not allowed to leave the decomposition chamber. The volume of the decomposition chamber was kept constant by confining a foam sample between two pistons. The lateral surface of the foam was also confined with a stainless steel cylinder. A pneumatic piston, controlled by a displacement gauge, was used to keep the decomposition chamber volume constant. Decomposition gases were retained in the decomposition using O-rings on the pistons. The force required to maintain a constant volume divided by the cross-sectional area of the pistons gave the pressure within the decomposition chamber.

The RMS error between the SREF pressure predictions and the measured pressure for the loading phase of the hot cell experiment was 0.3%. The RMS error during the unloading phase of the hot cell experiment was 12.6% giving an overall RMS error of about 6.3%. The loading phase included the time that the sample temperature was increased from room temperature to the set temperature of 300ºC and the isothermal period while the foam was at 300ºC. During the loading phase, the load increased due to decomposition chemistry. The unloading phase of the hot cell experiments included the time that the hot cell heaters were turned off and the cell cooled. The agreement between the predictions and measurements were noticeable different as the hot cell cooled. Part of the difference between the measured response and the predicted response is related to uncertainty in the sample temperature. The hot cell was actively cooled with chilled water. Active cooling created large temperature gradients within the confining pistons, which may have led to uncertainty in the sample temperature measurements. Other sources of uncertainty include complex phase equilibrium during condensation that is not included in the SREF model. Also all of the SREF model parameters were based on ramp-up experiments and not cool-down experiments that favor crosslinking retrograde reactions such as the reversible Diels-Alder reaction. More accurate results could have been obtained at substantial complexity by including reversibility in the reaction mechanism. The SREF decomposition chemistry model was developed with the intent of describing significant reactions prevalent during decomposition events expected during abnormal thermal environments such as fire where reversible reactions are inconsequential. For these abnormal thermal environments, the SREF model has been shown to give quantitative agreement with experimental observations.

References

1. Loy, D.A., Wheeler, D.R., Russick, E. M., McElhanon, J.R., Saunders, R. S., “Method of Making Thermally Removable Epoxies,” Sandia National Laboratories, Patent #6,337,384 (January 2002).

2. Aubert, J.H., McElhanon, J.R., Saunders, R.S., Sawyer, P.S., Wheeler, D.R., Russick, E.M., Rand, P.B., and Loy D.A., “Progress in Developing Removable Foams, Adhesives, and Conformal Coatings for the Encapsulation of Weapon Components,” Sandia National Laboratories Report SAND2001-0295 (2001).

3. McElhanon, J.R., Russick, E.M., Wheeler, D.R., Loy, D.A., and Aubert, J.H., “Removable Foams Based on an Epoxy Resin Incorporating Reversible Diels-Alder Adducts,” *J. Appl. Polym. Sci.*, **85**, 1496 (2002).

4. Clayton, D., J. “Modeling Flow Effects During Polymer Decomposition using Percolation Lattice Statistics,” Dissertation, Brigham Young University, Provo, UT (2002).

5. Erickson, K.L., Trujillo, S.M., Thompson, K.R., Sun, A.C., Hobbs, M.L., Dowding, K.J., “Liquefaction and flow behavior of a thermally decomposing removable epoxy foam,” Materials Characterisation 2003, WIT Press, Southampton Press (2003).

6. Hobbs, M. L., Erickson, K. L., and Chu, T. Y., “Modeling Decomposition of Unconfined Rigid Polyurethane Foam,” *Polymer Degradation and Stability*, **69**(1), 47 (2000).

7. Hobbs, M.L., Erickson, K.L., Chu, T.Y., Borek, T.T., Thompson, K.R., Dowding, K.J., Clayton, D., and Fletcher, T. H., “CPUF – Chemical-structure-based PolyUrethane Foam decomposition model,” Sandia National Laboratories Report SAND2003-2282, Albuquerque, NM (2003).

8. Hobbs, M.L. and Lemmon, G.H., “SPUF—A Simple PolyUrethane Foam mass loss and response model,” Sandia National Laboratories Report SAND2003-2099, Albuquerque, NM (2003). See also Hobbs, M.L. and Lemmon, G.H., “Polyurethane foam response to fire in practical geometries,” accepted for publication in *Polymer Degradation and Stability* (October 2003).

9. Laurendeau, N.M., “Heterogeneous Kinetics of Coal Char Gasification and Combustion,” *Prog. Energy Combust. Sci.*, **4**, 221 (1978).

10. Walker, P.L., Rusinko, F., and Austin, L.G., *Advances in Catalysis* , D.D. Eley, P.W. Selwook, and P.B. Weisz, Editors, **XI**, Academic Press Inc., New York, 134 (1959).

11. Park, K.Y. and Edgar, T.F., “Modeling of Early Cavity Growth for Underground Coal Gasification,” *Ind. Eng. Chem. Res.*, **26**, 237 (1987).

12. Thorsness, C.B. and Kang, S.W., “A General-Purpose, Packed-Bed Model for Analysis of Underground Coal Gasification Processes,” Lawrence Livermore National Laboratory Report UCID-20731, University of California, Livermore California (1986).

13. Wang, S.C. and Wen, C.Y., “Experimental Evaluation of Nonisothermal Solid-Gas Reaction Model,” *AIChE J.*, **18**, 1231 (1972).

14. Hobbs, M. L., Radulovic, P. T., and Smoot, L. D., “Modeling Fixed-Bed Coal Gasifiers,” *AIChE J.*, **38**(5), 681 (1992).

15. Froment, G.F. and Bischoff, K.B., *Chemical Reactor Analysis and Design*, second edition, John Wiley & Sons, Inc., New York (1990).

16. Bird, R.B., Stewart, W.E., Lightfoot, E.N., *Transport Phenomena*, second edition, John Wiley & Sons, Inc., New York (2002).

17. Grant, D.M., Pugmire, R.J., Fletcher, T.H., and Kerstein, A.R., "Chemical Model of Coal Devolatilization using Percolation Lattice Statistics," *Energy & Fuels*, **3**, 175 (1989).

18. Henley, E.J. and Seader, J.D., *Equilibrium-Stage Separation Operations in Chemical Engineering*, John Wiley & Sons, New York (1981).

19. Shampine, L.G. and Watts, H.A., "ZEROIN – a root-solving code," Sandia National Laboratories Report SC-TM-70-631, Albuquerque, NM (1970).

20. Rajtar, P.E., Advanced Technical Service Engineer for 3M Performance Fluids, 3M Center, Building 223-6S-04, St. Paul, MN 55144-1000 (October 15, 2002).

21. Air Products DC-193, technical product information (October 21, 2002).

22. Daubert, T.E., Danner, R.P., Subul, H.M., and Stebbins, C.C., *Physical and Thermodynamic Properties of Pure Compounds: Data Compilations*, extant 1994 (core with 4 supplements), Taylor & Fracis, Bristol, PA (1994).

23. Fletcher, T.H., Kerstein, A.R., Pugmire, R.J., Solum, M.S., Grant, D.M., "Chemical Percolation Model for Devolatilization 3. Direct use of ^{13}C NMR data to Predict Effects of Coal Type," *Energy & Fuels*, **4**, 54 (1990).

24. Hobbs, M.L. and Romero, V. J., "Uncertainty analysis of decomposing polyurethane foam," *Thermochimica Acta*, **384**, 393 (2002).

25. Eldred, M. S., "Optimization Strategies for Complex Engineering Applications," Sandia National Laboratories report SAND98-0340. Albuquerque, NM (1998).

26. Flory, P.J., *Principles of Polymer Chemistry*, Cornell University Press, Ithaca, New York (1953).

27. Erickson, K.L., "DSC data," EMAIL to Hobbs, M.L., (January 15, 2003).

28. Dobranich, D., and Gill, W., "A Thermal Model Validation Test Unit for the W76-1 AF&F – Design, Experiments, and Simulations," Sandia National Laboratories Report SAND2002-1769, Albuquerque, NM (2002).

29. Aselage, T.L, "C_p Measurements for Removable Epoxy Foam," EMAIL to Hobbs, M.L., (September 18, 2001).

30. Hobbs, M.L., Erickson, K.L., Chu, T.Y., Borek, T.T., Renlund, A.M., and Thompson, K.R., "Thermal Decomposition of Polymeric Foams: Model Development based on Decomposition Chemistry," *Fourth Biennial Tri-Lab Conference*, Albuquerque, NM (October 23-24, 2001).

31. Incropera, F.P. and DeWitt, D.P., *Fundamentals of Heat and Mass Transfer*, Fifth Edition, John Wiley & Sons, New York (2002).

32. Gembarovic, J. and Taylor, R.E., “Thermophysical Properties of Plastic Sample—A Report to Sandia National Laboratories,” Thermophysical Properties Research Laboratory, Inc. report TPRL2868, West Lafayette, IN (Oct. 2003).

33. Renlund, A.M., Miller, J.C., Trott, W.M., Erickson, K.L., Hobbs, M.L., Schmitt, R.G., Wellman, G.W., and Baer, M.R., “Characterization of Thermally Degraded Energetic Materials,” *Eleventh International Detonation Symposium*, Snowmass, CO (1998).

34. Renlund, A.M., “Hot Cell Data for REF encapsulant,” EMAIL to Hobbs, M.L., (November 11, 2002).

Appendix

This appendix includes a flow sheet describing the SREF model algorithm and the input deck for run 13.

SREF Model Algorithm

Figure 30 shows the SREF algorithm. After the SREF parameters are initialized and echoed to the output files, the model uses a stiff ODE solver to solve for the population parameters. The foam composition is determined using percolation theory with the population parameters. The VLE species are determined from the foam composition and the mole fractions of the combined-phase VLE species are determined. After calculating the equilibrium ratios, or *K*-values, the Rachford-Rice equation is solved for the ratio of the moles of vapor to the moles of combined-phase VLE species from which the VLE solid fraction, VLE mole fractions in both the vapor and condensed-phase, and the average gas-phase molecular weight is determined. A material balance is then solved to determine the composition of the condensed-phase and molecular weight of the condensed-phase. The mass transport model, pressurization model, and extent of reaction needed for the distributed activation energy model is updated between calls to the stiff ODE solver. And output variables of interest are written to various files.

Run 13 input deck

```
t $ lecho: t echo input deck to oecho, f  no input deck echo
6 $ nsay   number of the following lines in the header description
C----------------------------------------------------------------------C
C       Simple Removable Epoxy Foam (SREF) decomposition model         C
C       run 013: r20.l.u.p.0522                                        C
C----------------------------------------------------------------------C
C Kinetic Parameters
C----------------------------------------------------------------------C
1e+13 2e+15 2e+16 6e+12     $ a(1:4) prefactors, 1/s
28700 46400 58100 43500     $ e(1:4) act. Energies, cal/mol
760 2800 6600 790  $ esig(1:4) std dev., cal/mol
C----------------------------------------------------------------------C
C Lattice Parameters and Initial Conditions for SREF Mechanism
C    Only sig+1 and osres can be changed in this section.
C    Note: so + l1o + l2o + l3o = 0.95; 0.05 is the carbon residue
C----------------------------------------------------------------------C
3.0     $ sig+1  Lattice coordination number
0.192   $ so     Initial sorbed populations (blowing agent & surfactant)
```

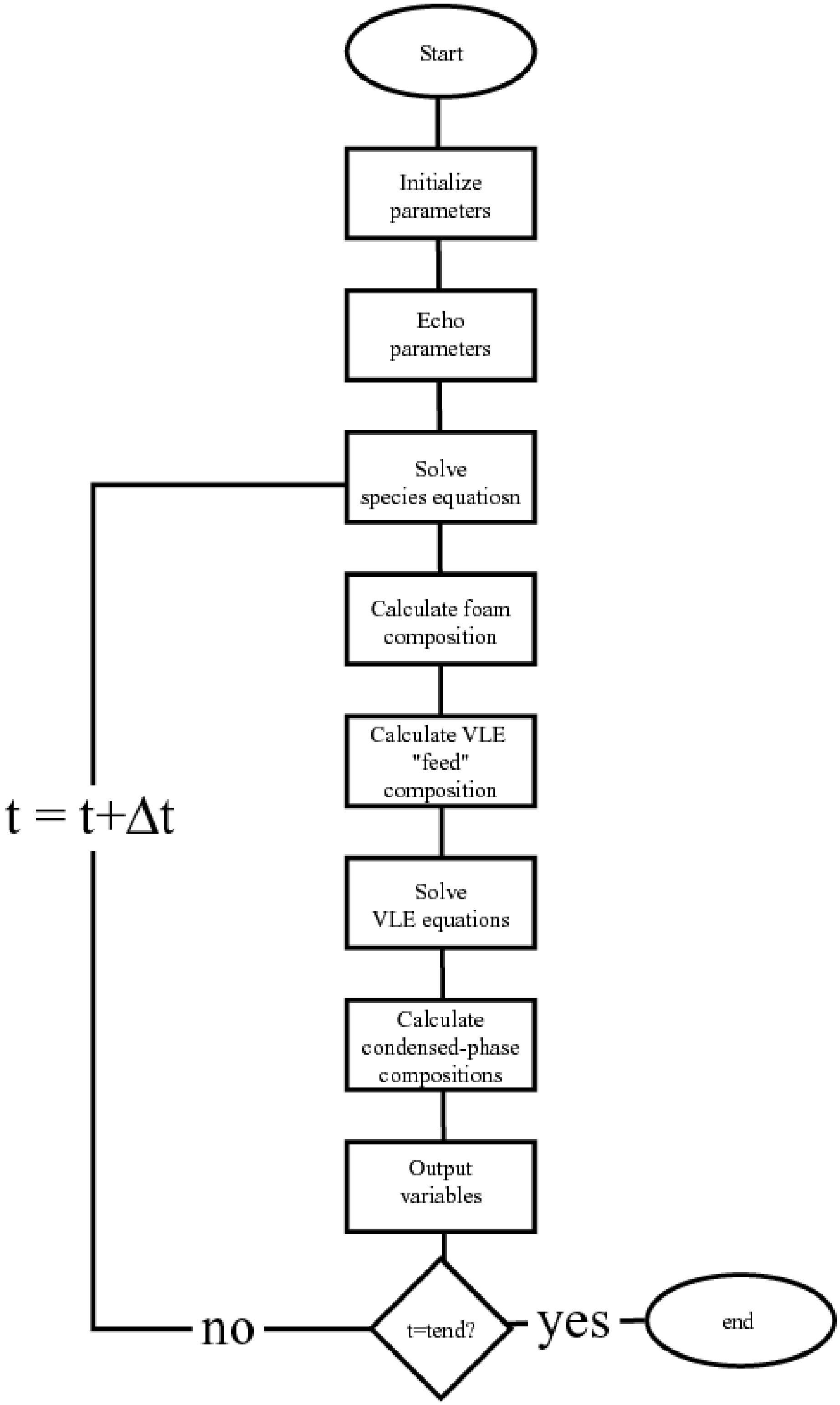

Fig. 30. SREF algorithm.

```
0.104   $ l1o    Initial OS bridge pop. (OctamethylcyclotetraSiloxane)
0.563   $ l2o    Initial MP bridge pop. (Mixed Products)
0.091   $ l3o    Initial BPA bridge pop. (BisPhenol A)
0.444 $ osres  OS residue (0: no OS in residue, 1: all OS in residue)
C----------------------------------------------------------------------C
C Molecular Weights [note mw(5)-mw(7),mw(10) calculated by SREF model]
C----------------------------------------------------------------------C
120.    $ mw(1)  BAS mw:Blowing Agent (73.5wt%,338) Surf. (26.5wt%,60.)
296.    $ mw(2)  OS molecular weight (OctamethylcyclotetraSiloxane)
140     $ mw(3)  MP molecular weight (Mixed Products)
228.    $ mw(4)  BPA molecular weight (BisPhenol A)
1E3     $ mw(8)  Nonvolatile carbon residue molecular weight
1E3     $ mw(9)  Nonvolatile OS residue molecular weight
4E3     $ mw(11) Nonvolatile XLarge-Mer residue molecular weight
10      $ maxmer Maximum mer size for Large-Mer residue (maxmer>4)
C----------------------------------------------------------------------C
C VLE Parameters, Mass Transport Parameters, and Pressure
C    Pc, critical pressures used to limit VLE K-values
C    Vc, critical volume used in molecular diffusivity calculation
C    Mass transport resistance can be shut off by setting dstar to 0
C----------------------------------------------------------------------C
5.0     $ pc(1)  BAS critical pressure, atm
13.1    $ pc(2)  OS critical pressure, atm
52.0    $ pc(3)  MP crit. pres., atm (ave of o,m,p-cresol, phenol, fu-
ran)
28.9    $ pc(4)  BPA critical pressure, atm
38.7    $ pc(5)  2-mer critical pressure, atm
38.7    $ pc(6)  3-mer critical pressure, atm
38.7    $ pc(7)  4-mer critical pressure, atm
2045.0  $ vc(1)  BAS critical volume, cc/mol
970.0   $ vc(2)  OS critical volume, cc/mol
229.0   $ vc(3)  MP critical volume, cc/mol
677.0   $ vc(4)  BPA critical volume, cc/mol
30 $ act(1) BAS constant activity coefficient
0.5 $ act(2) OS constant activity coefficient
3 $ act(3) MP constant activity coefficient
0.5 $ act(4) BPA constant activity coefficient
0.5 $ act(5) 2-mer constant activity coefficient
0.5 $ act(6) 3-mer constant activity coefficient
0.5 $ act(7) 4-mer constant activity coefficient
2 $ dopsur d*/phi for surfactant
0.542  $ dopba  d*/phi for blowing agent
2    $ dop    d*/phi for polymer fragments
0.039   $ sft    Solid fraction transition for BAS species
0.001   $ width  Width of solid fraction transition for BAS species
C----------------------------------------------------------------------C
C Pressure flag
C pflag--> f: pressure contant at pinit value
C          t: pressurization calculated using rhof, rhop, and vole
C----------------------------------------------------------------------C
f            $ pflag  f pressure constant, t dynamic pressurization
1  $ pinit  Initial hydrostatic pressure in atm
0.312  $ rhof   Initial foam density, g/cc
1.09  $ rhop   Initial polymer density, g/cc
```

```
0.638  $ vole   Volume of the element, cc
C-----------------------------------------------------------------------C
C Confinement parameters
C cflag--> 0: osres/dop from above used
C          1: unconfined (osres = 0. and dop = 0.1-cm)
C          2: partially confined (dorif needs to be set for this case)
C             (osres and dop calculated based on orifice diameter)
C          3: totally confined (osres = 0.444 and dop = 32.3)
C-----------------------------------------------------------------------C
1       $ cflag  1: unconf, 2 part conf, 3 tot conf; 0 use osres/dop/sft
60.     $ dorif  orifice diameter, um (used only if partially confined)
C-----------------------------------------------------------------------C
C Output control and temperature history
C-----------------------------------------------------------------------C
t f t t $ otmpsf, otimsf, omg,   omc  : TvSf, tvSf, MwG, MwC
t t t t $ osfvle, ovof,   oxvle, oyvle: Sf-vle, V/F, Y-vle, X-vle
t t t f $ owc,    opop,   okval, opres: w-c, pop, k-values, pres
f t t t $ ltime,  ovg,    ogmol, otmp : time, volgas, molgas, temp
0.5     $ dt0    time step, s
15.     $ iprint print increment, s
5.      $ dtmax  Maximum time step, s
1650.   $ timax            final time in calculation, s
856    $ ntime   number of time points
     0.00  298.66
```

The complete input deck continues with an additional 855 time points for this 20ºC/minute run.

Distribution

Brigham Young University (1)
Department of Chemical Engineering
Attn: Dr. Thomas H. Fletcher
350 K Clyde Building
Provo, Utah 84602-4100

Easterling Statistical Consulting (1)
51 Avenida del Sol
Cedar Crest, NM 87008

Federal Aviation Administration (1)
Attn: Richard E. Lyon
Fire Safety Section, AAR-422
William J. Hughes Technical Center
Atlantic City International Airport, NJ 08405

New Mexico State University (1)
Department of Mechanical Engineering
Attn: Richard G. Hills
Las Cruces, New Mexico 88003

United States Department of Commerce
Attn: Kathryn M. Butler
Building and Fire Research Laboratory
National Institute of Standards and Technology
Gaithersburg, MD 20899

University of California, Berkeley (1)
Attn: Carlos Fernandez-Pello
Mechanical Engineering Department
6105a Etcheverry Hall
University of California
Berkeley, CA 94720

University of Utah (1)
Attn: Ronald Pugmire
Associate Vice President for Research
Professor of Chemical & Fuels Engineering
210 Park Building
Salt Lake City, UT 84112

University of Utah (1)
Attn: David M. Grant
Distinguished Professor of Chemistry
Henry Eyring Bldg
315 S 1400 East Rm 2020
Salt Lake City, UT 84112

University of Washington (1)
Dept of Mechanical Engineering
Attn: Ashley Emery
Box 352600
Seattle, WA 98195-2600

Sandia

1	MS0888	1811	R. L. Clough
1	MS0888	1811	J. H. Aubert
1	MS0888	1811	E. M. Russick
1	MS0886	1822	R. P. Goehner
1	MS0886	1822	T. T. Borek
1	MS0888	1832	N. R. Sorenson
1	MS1411	1834	A. L. Frischknecht
1	MS0481	2132	R. J. Harrison
1	MS0481	2132	D. R. Helmich
1	MS0481	2132	T. F. Hendrickson
1	MS0427	2134	R. A. Paulsen, Jr.
1	MS1452	2552	L. G. Minier
1	MS1454	2554	A. M. Renlund
1	MS0311	2616	M. J. Craig
1	MS0627	2991	J. W. Shelton, III
1	MS1202	5932	T. A. Ulibarri
1	MS0748	6413	D. G. Robinson
1	MS9014	8242	D. M. Kwon
1	MS9014	8242	A. R. Ortega
1	MS9051	8351	A. R. Kerstein
1	MS9052	8361	R. Behrens, Jr.
1	MS9052	8361	S. B. Margolis
1	MS9042	8752	C. D. Moen
1	MS9042	8752	R. H. Nilson
1	MS9401	8752	B. M. Rush
1	MS0841	9100	T. C. Bickel
1	MS0836	9100	M. R. Baer
1	MS1393	9100	T. Y. Chu (in Washington DC, Forrestal Building)
1	MS0826	9100	D. K. Gartling
1	MS0824	9110	W. L. Hermina
1	MS0834	9112	M. R. Prairie
1	MS0834	9112	K. L. Erickson
1	MS0834	9112	S. M. Trujillo
1	MS0826	9113	S. N. Kempka
1	MS0834	9114	J. E. Johannes
1	MS0834	9114	T. A. Baer
1	MS0834	9114	P. L. Hopkins
1	MS0834	9114	A. M. Kraynik
1	MS0834	9114	P. R. Schunk
1	MS0834	9114	A. C. Sun
1	MS0836	9116	E. S. Hertel
1	MS0836	9116	B. L. Bainbridge
1	MS0836	9116	B. D. Boughton
1	MS0836	9116	J. F. Dempsey
1	MS0836	9116	D. D. Dobranich
1	MS0836	9116	R. C. Dykhuizen
1	MS0836	9116	N. D. Francis, Jr.
10	MS0836	9116	M. L. Hobbs

1	MS0836	9116	R. E. Hogan
1	MS0836	9116	C. Romero
1	MS0836	9116	R. G. Schmidt
1	MS0836	9117	R. O. Griffith
1	MS0836	9117	M. E. Larsen
1	MS0555	9122	M. S. Garrett
1	MS0555	9122	K. R. Thompson
1	MS0893	9123	M. K. Neilsen
1	MS0824	9130	J. L. Moya
1	MS0821	9132	L. A. Gritzo
1	MS0836	9132	W. Gill
1	MS1135	9132	J. T. Nakos
1	MS1135	9132	J. M. Suo-Anttila
1	MS1135	9132	S. R. Tieszen
1	MS0828	9133	M. Pilch
1	MS0828	9133	B. F. Blackwell
1	MS0828	9133	K. J. Dowding
1	MS0828	9133	V. J. Romero
1	MS0828	9133	W.L. Oberkampf
1	MS0835	9140	J. M. McGlaun
1	MS0835	9141	E. A. Boucheron
1	MS0835	9141	S. W. Bova
1	MS0835	9141	M. W. Glass
1	MS0835	9141	R. R. Lober
1	MS0847	9211	M. S. Eldred
1	MS0819	9211	R. G. Trucano
1	MS0423	9732	J. A. Fernandez
1	MS0151	9750	A. C. Ratzel
1	MS0139	9900	M. O. Vahle
1	MS0139	9905	S. E. Lott
1	MS0829	12323	B. M. Rutherford
1	MS0405	12333	T. R. Jones
1	MS0405	12333	L. A. Schoof
1	MS0405	12333	S. E. Camp
1	MS0958	14172	J. A. Emerson
1	MS9018	8945-1	Central Technical Files
2	MS0899	9619	Technical Library